

# **Selected-area, self-assembly nucleation used in the fabrication of nanofocusing refractive lenses from diamond**

**Rachel Irlam**

*A dissertation submitted to the University of Bristol in  
accordance with the requirements for the award of the  
Honours degree of Master of Science in Chemistry.*

**Supervisor: Professor Paul May**

**Second Assessor: Professor Mike Ashfold**

**Section: Physical Chemistry**



University of  
**BRISTOL**



## **Acknowledgements**

I would first like to acknowledge Professor Paul May, my project supervisor, for his guidance and support throughout the project. I would also like to thank Dr. Oliver Fox for training me to use the microwave reactor and for his massive amount of day-to-day help and advice; this work would not have been possible without him. Further thanks go to Professors Mike Ashfold and Andrew Orr-Ewing, my second and third assessors. I would also like to acknowledge Dr. Simon Hall for his advice with the silane work, Ian Nichols for training me to use the dynamic light scattering equipment and Dr. Lucia Alianelli and Dr. Kawal Sawhney from the Diamond Light Source Ltd. Final thanks go to the Bristol University Diamond Group for making the project so enjoyable.

## **Declaration**

I declare that the work in this dissertation was carried out in accordance with the requirements of the University's Regulations and Code of Practice for Taught Postgraduate Programmes and that it has not been submitted for any other academic award.

Except where indicated by specific reference in the text, this work is my own work. Work done in collaboration with, or with the assistance of others, is indicated as such. I have identified all material in this dissertation which is not my own work through appropriate referencing and acknowledgement. Where I have quoted from the work of others, I have included the source in the references/bibliography. Any views expressed in the dissertation are those of the author.

SIGNED:

.....

DATE: .....

# Table of Contents

<b>Acknowledgements .....</b>	<b>2</b>
<b>Declaration .....</b>	<b>3</b>
<b>Abstract .....</b>	<b>8</b>
<b>1 Diamond .....</b>	<b>10</b>
1.1 Properties and applications .....	10
1.2 Structure and morphology .....	11
1.3 Synthetic diamond .....	13
1.3.1 Substrates for diamond CVD.....	15
1.3.2 Mechanism of diamond CVD .....	15
1.4 High-aspect-ratio structures with smooth, vertical sidewalls made from diamond and their application as x-ray optics .....	19
1.4.1 Synchrotron radiation .....	19
1.4.2 Refractive x-ray lenses .....	21
<b>2 Deep reactive ion etching of silicon for the fabrication of high-aspect-ratio structures.....</b>	<b>23</b>
2.1 The Bosch process .....	24
2.2 The cryogenic process .....	25
<b>3 Problems arising from standard DRIE processes.....</b>	<b>26</b>
3.1 Sidewall scalloping .....	26
3.2 Notching and undercutting .....	27
3.3 Aspect-ratio dependent etching (ARDE) effects .....	27
<b>4 Current technologies for etching high-aspect-ratio silicon structures with smooth and vertical sidewalls .....</b>	<b>28</b>
4.1 Surface Technology Systems .....	28
4.1.1 Adjustment of the standard Bosch process.....	28
4.1.2 STS products for DRIE of silicon .....	30
4.2 Plasma-Therm .....	31
4.3 Oxford Instruments .....	32
4.4 Unaxis Wafer Processing .....	34
<b>5 Comparison of the technologies offered by Plasma-Therm and Oxford Instruments.....</b>	<b>34</b>

<b>6</b>	<b>Reactive ion etching of high-aspect-ratio structures in diamond.....</b>	<b>35</b>
<b>7</b>	<b>Selected-area, self-assembly nucleation of nanodiamond particles.....</b>	<b>37</b>
7.1	Electrostatic self-assembly.....	37
7.2	Selected-area diamond nucleation .....	38
<b>8</b>	<b>Aims of the nanodiamond selected-area, self-assembly nucleation project</b>	<b>41</b>
<b>9</b>	<b>Experimental Method .....</b>	<b>42</b>
9.1	Electrostatic self-assembly of nanodiamond particles .....	42
9.1.1	The solutions.....	42
9.2	MWCVD reactor .....	43
9.3	Optical and scanning electron microscopy and Raman spectroscopy.....	45
9.4	Mass flow controller (MFC) calibration.....	46
<b>10</b>	<b>Results and Discussion.....</b>	<b>48</b>
10.1	Development of a resist-compatible and repeatable, electrostatic self-assembly nanodiamond nucleation .....	48
10.1.1	Alterations to the cleaning and drying steps.....	48
10.1.2	Investigation into the ionic polymer coating method .....	50
10.2	Investigating the use of a silane molecule to replace PDDA and PSS.....	51
10.3	The use of different substrates in chemical vapour deposition .....	60
10.3.1	Diamond on titanium.....	60
10.3.2	Diamond on zirconium.....	62
10.3.3	Diamond on strontium titanate.....	63
10.3.4	Diamond on aluminium nitride.....	63
10.4	Investigation into the properties of the nanodiamond solution used in self-assembly nucleation.....	68
10.4.1	Nanodiamond from the Carbon Research Institute, Japan .....	69
10.4.2	Nanodiamond from MicroDiamant: XP 0.018 and XPC 0.018.....	73
10.4.3	Nanodiamond in DMSO from University of Gdansk, Poland.....	75
10.5	Selected-area nucleation .....	79
10.5.1	Resist layer removal.....	79
10.5.2	Buffered oxide etch (BOE) .....	83
10.5.3	Diamond deposition on substrates fabricated by Kelvin Nanotechnology.....	85
10.6	Application of selected-area, self-assembly nucleation using resist lift-off to lens-mould substrates.....	90

10.7	The effect of varying the concentration of N <sub>2</sub> and Ar added to the H <sub>2</sub> /CH <sub>4</sub> gas mixture used in diamond MWCVD .....	94
<b>11</b>	<b>Future Work.....</b>	<b>97</b>
<b>12</b>	<b>Conclusions .....</b>	<b>98</b>
<b>13</b>	<b>References .....</b>	<b>100</b>
<b>14</b>	<b>Appendices .....</b>	<b>104</b>
14.1	Deposition tables .....	104
14.2	MFC Calibration Graphs .....	108
14.3	Photographs from the spin-coating experiments .....	110
14.4	Optical microscope images of the diamond films grown in the investigation with CEST in self-assembly .....	112
14.5	SEM images taken of diamond films grown on CEST-seeded silicon substrates....	118
14.6	SEM images freestanding diamond films grown on AlN.....	121
14.7	Resist testing photographs.....	125
14.8	SEM images of SiO samples before and after BOE .....	141
14.9	SEM images of the DL samples from Kelvin Nanotechnology after a 3 h NCD on each and the Inkscape drawings used to calculate various parameters .....	149
14.10	SEM images comparing the filling of the trenches of RAL132 and RAL133 .....	154
14.11	SEM images of selected area deposition in RAL135 and RAL136 .....	155
14.12	Optical microscope images comparing the diamond films grown for 1 h under varying gas mixtures.....	156
14.13	SEM images comparing the diamond films grown after 1 h in various gas mixtures.....	161



## Abstract

This project involved optimising the various steps used in selected-area, self-assembly nanodiamond particle nucleation, with the view to applying the new procedure to diamond deposition on silicon substrates. Successful selected-area, self-assembly nucleation would enable fabrication of diamond refractive lenses using chemical vapour deposition, capable of focusing hard x-rays down to nanosized focal spots at synchrotron sources.

Firstly, experiments, conducted with the solvents used in the cleaning and washing steps described in earlier work for electrostatic self-assembly nucleation, led to the development of a new resist-compatible, repeatable self-assembly nucleation process to be used with 1 cm<sup>2</sup> silicon substrates. Investigations then looked at the efficacy of spin-coating rather than immersion as a means of coating the substrate with the polymer layer, and also the use of a silane molecule rather than the two polymers in the nanodiamond self-assembly process. From these, a standard method for the use of carboxyethylsilanetriol in self-assembling nanodiamond particles onto silicon was devised and the conclusion that spin-coating is not as efficient as immersion was met. Dynamic light scattering equipment was used to analyse the effect of sonication time, sonication power and concentration on the average particle size found in various nanodiamond solutions, leading to a recommended treatment of each nanodiamond solution before its use in the self-assembly process.

Once self-assembly nucleation of nanodiamond particles had been optimised, ways in which to improve the selected-area procedure were investigated. Tests were carried out to evaluate how agitation, substrate pre-treatment, temperature of the lift-off solution and the time the resist substrate spends in the lift-off solution affect removal of the resist layer. These allowed the suggestion of best practice, resist-removal methods for the three resist layers ma-N2410, ma-N415 and UV-III. Carrying out a buffered oxide-etch step on various silicon oxide-coated substrates after diamond deposition enabled the analysis of the selectivity achieved using this method and whether it was good enough to be practical for lens-mould fabrication.

The recommended self-assembly nucleation methods were then combined with the optimised resist-removal methods and applied to real lens-mould substrates to evaluate their success. This resulted in better selected-area diamond deposition than has been achieved in previous work.

Throughout the project the self-assembly nucleation procedures developed were also applied to zirconium, strontium titanate, titanium and aluminium nitride substrates to determine the efficacy of the seeding processes on non-silicon surfaces, with aluminium nitride and strontium titanate proving successful. Work was carried out with aluminium nitride as a growth substrate, generating freestanding thin diamond films of varying thicknesses after various deposition times. The thinnest film produced was after a 7 min nanocrystalline diamond deposition and had a thickness of 83 nm over a 1 cm<sup>2</sup> surface area. Finally, thirty 1 cm<sup>2</sup> silicon substrates were seeded using the same self-assembly nucleation process and then each grown on using a different gas mixture. This allowed evaluation of the effect of nitrogen and argon added to the chemical vapour deposition plasma on the size, morphology and surface smoothness of the diamond crystals. The presence of nitrogen in the gas mixture was found to cause the deposition of nanocrystalline diamond and increasing the concentration of argon was seen to decrease the diamond crystal size and increase their surface roughness. Analysis of these findings led to the recommendation of an ideal gas mixture for producing smooth, nanocrystalline diamond layers.

# 1 Diamond

In today's society diamonds represent wealth and prestige<sup>1</sup> in the same way they have done for over two millennia. Despite the fact that there are references to crystal diamond discovered in India as far back as 70AD, it was not until relatively large deposits were discovered in South Africa in 1870 that the use of diamond became a lot more widespread.<sup>2</sup> Today, the latest technology enables the deposition of thin films of diamond on silicon substrates and even three-dimensional diamond structures can be produced by, for example, using processes to etch either the silicon substrate, which can then act as a mould for the deposition of a diamond layer, or the diamond itself. In this way diamond micro- and nanostructures can be produced.

## 1.1 Properties and applications

Not only sought-after for its value as a gemstone, diamond is also of great interest to scientists and engineers thanks to its impressive array of unique properties<sup>3</sup>, which stem from the very stable, covalently-bound, tetrahedral carbon network.<sup>4</sup> To name a few, diamond is the hardest, stiffest and least compressible known material. It possesses a low thermal expansion coefficient, a high thermal conductivity at room temperature and a broad-band optical transparency, remaining transparent from the ultraviolet to the far-infrared region. Diamond is also chemically inert and has a wide band gap that means it is electrically insulating.<sup>5</sup> However, it can be easily doped, enabling its use as a semiconductor.<sup>6</sup>

If these properties could be exploited then diamond would be the ideal material in an extensive number of applications, ranging from electronics to cutting and polishing. However, the vast expense and scarcity of natural diamond, coupled with the fact that it often contains impurities or defects<sup>7</sup>, means that these industrial applications are often only theoretical. Instead, researchers have developed methods to grow synthetic diamond, which is free from defects whilst displaying all the properties of natural diamond.<sup>8</sup>

## 1.2 Structure and morphology

Diamond is one of the two allotropes of crystalline carbon<sup>9</sup> and can adopt either the hexagonal or cubic structure. Each carbon atom is covalently bound to four others and is thus  $sp^3$ -hybridised, which generates a regular tetrahedral lattice. Although the physical properties of hexagonal and cubic diamond are similar due to the same bonding in both structures, hexagonal diamond possesses a total energy that is higher than that of cubic diamond. As a result hexagonal diamond is the less stable form of the two and the less abundant.<sup>10</sup>

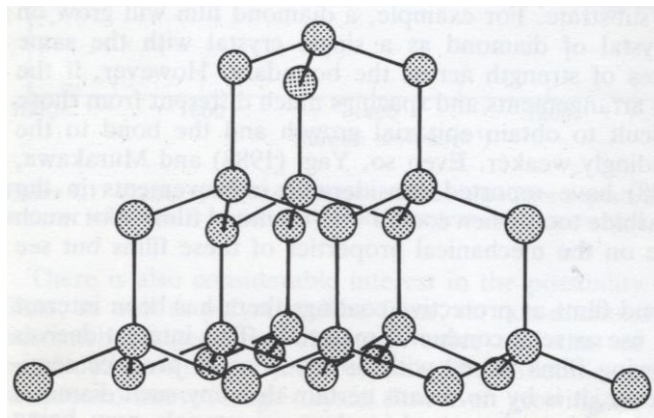


**Figure 1:** Model of the diamond lattice. Image reproduced from reference 9.

Graphite is the other allotrope of crystalline carbon where the bonds between the carbon atoms are  $sp^2$ -hybridised, generating planar structures that are arranged in layers and it is the thermodynamically stable carbon allotrope under standard conditions. However, once formed, diamond will not spontaneously convert to graphite since there is a large activation barrier between the two states and so is said to be metastable.<sup>11</sup> The conditions used to synthesise artificial diamond must therefore be extreme to overcome the barrier to conversion of one allotrope to another<sup>12</sup> and favour diamond over graphite thermodynamically.

Both natural and synthetic diamonds display a variety of crystal forms and shapes. Crystal growth tends to take place on planes with low Miller indices, such as {001}, {011} and {111}.<sup>13</sup> There are three types of primary diamond facets; <100>, <110> and <111>.<sup>14</sup>

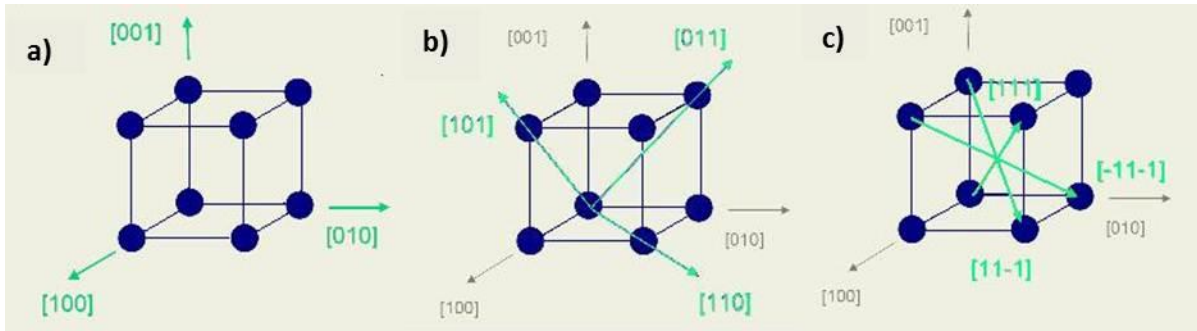


**Figure 2:** Orientations of the structure of a diamond crystal described by Miller indices (a)  $\langle 100 \rangle$  (b)  $\langle 110 \rangle$  (c)  $\langle 111 \rangle$ . Image reproduced from reference 14.

Outward growth on all eight  $\{111\}$  planes results in the commonly observed octahedral form of diamond with triangular facets. The indices  $\{001\}$  refer to the six sets of mutually perpendicular planes and uniform growth on each of these six planes generates a crystal with the cubic form and square facets. A regular crystal with a dodecahedral form arises from growth on the twelve planes that the  $\{011\}$  indices refer to. If the growth rate is not uniform on each plane, some faces may be larger than others and growth on more than one family of planes leads to other crystal forms, such as the cubo-octahedron. Natural diamonds are predominantly octahedrons, whereas the cubic form is only occasionally observed and the dodecahedral form is never seen in nature. Synthetic diamonds are often octahedrons or cubo-octahedrons but can sometimes display dodecahedral facets.<sup>13</sup>

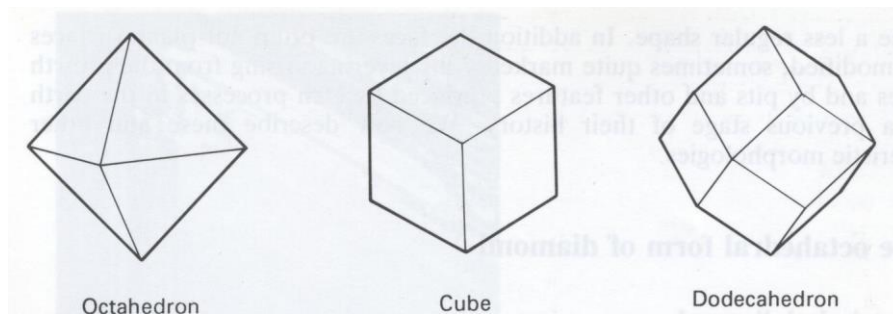


**Figure 3:** Octahedron, cube and dodecahedron forms of diamond. Image reproduced from reference 13.

The morphology of synthetic diamond crystals is highly sensitive to changes in methane concentration so can be tuned through control of the growth conditions used in the synthesis method<sup>15</sup> (these methods are discussed in **Section 1.3**). At a methane concentration of  $\leq 0.3\%$ , polycrystalline diamond films on silicon resulting from deposition

by microwave CVD have diamond grains with triangular (111) crystallographic facets. At methane concentrations between 0.4% and 1%, the majority of crystallographic faces on the surface are (100) so the film is dominated by square facets with the square feature of the (100) faces becoming more prominent at higher concentrations. At methane concentrations  $\geq 1\%$ , microcrystallites with no clear faceting dominate.<sup>16, 17</sup>

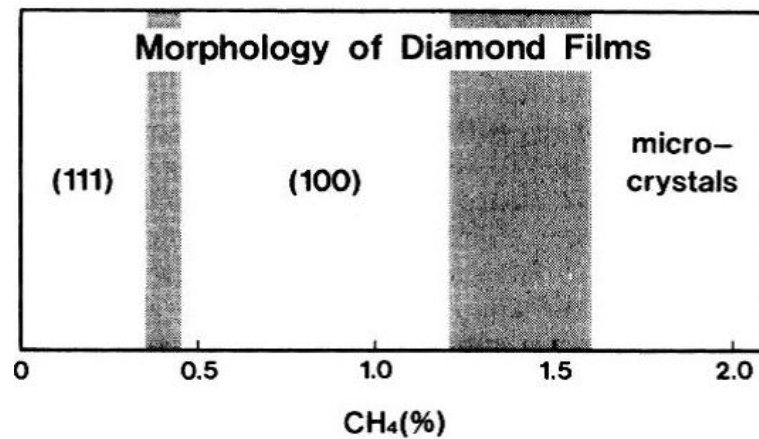


**Figure 4:** Diamond film morphology with respect to methane concentration. Image reproduced from reference 12.

The grain size of synthetic diamond is important as it affects its properties and can also be altered by using different growth conditions. Microcrystalline diamond (MCD) thin films have a grain size between 100 nm and 1000 nm and have a rough surface, whereas those with a grain size smaller than 100 nm are termed nanocrystalline diamond (NCD) and exhibit smoother surfaces than microcrystalline films.<sup>18</sup> Smoother still are ultrananocrystalline diamond (UNCD) films that consist of crystallites that have an average size of between 3 nm and 10 nm. These are the smoothest films and are useful in optics since radiation scattering is minimised with smoother surfaces.<sup>19</sup>

### 1.3 Synthetic diamond

In the early 1950s, high pressure, high temperature (HPHT) techniques were used to generate the first synthetic diamond for commercial applications. This method involves the use of pressures between 50 kbar and 100 kbar in conjunction with temperatures between 1500 °C and 2000 °C in order to recrystallise metal-solvated carbon and form diamond. It was not until the early 1980s when the rate of vapour-phase diamond growth reached the

micrometers per hour ( $\mu\text{m h}^{-1}$ ) scale that attention was focused on chemical vapour deposition (CVD) as a feasible method of synthesising diamond for industrial applications.<sup>12</sup> CVD is one of the most common techniques used today to grow synthetic diamond. From the table below, comparing the properties of CVD diamond with those of natural diamond, it is clear from the similarity in the values that the method is effective.

**Table 1:** Comparison of the properties of synthetic and natural single-crystal diamonds. Reproduced from reference 8.

	<b>CVD Diamond</b>	<b>Single-Crystal Diamond</b>
<b>Density [<math>\text{g cm}^{-3}</math>]</b>	3.51	3.515
<b>Specific Heat, <math>C_p</math> [<math>\text{J mol}^{-1}</math>] (at 300 K)</b>	6.195	6.195
<b>Thermal Conductivity [<math>\text{W m}^{-1} \text{K}^{-1}</math>] (at 25 °C)</b>	2100	2200
<b>Thermal Expansion [<math>10^{-6}/^{\circ}\text{C}</math>] (at 25-200 °C)</b>	2.0	1.5-4.8
<b>Index of Refraction at 10 <math>\mu\text{m}</math></b>	2.34-2.42	2.40
<b>Bandgap [eV]</b>	5.45	5.45
<b>Electrical Resistivity [<math>\Omega \text{cm}^{-1}</math>]</b>	$10^{12}$ - $10^{16}$	$10^{16}$
<b>Dielectric Constant (45 MHz – 20 GHz)</b>	5.6	5.7
<b>Dielectric Strength [<math>\text{V cm}^{-1}</math>]</b>	$10^6$	$10^6$
<b>Loss Tangent (45 MHz – 20 GHz)</b>	<0.0001	
<b>Saturated Electron Velocity</b>	2.7	2.7
<b>Carrier Mobilities [<math>\text{cm}^2 \text{V}^{-1} \text{s}^{-1}</math>]</b>		
<b>Electron (n)</b>	1350-1500	2200
<b>Positive Hole (p)</b>	480	1600
<b>Young's Modulus [GPa]</b>	910-1250	1250
<b>Compression Strength [GPa]</b>	8.68-16.53	16
<b>Vickers Hardness Range [GPa]</b>	50-100	57-100
<b>Coefficient of Friction</b>	0.05-0.15	0.05-0.15

Thanks to the development of plasma- and thermally-enhanced CVD methods, which enable diamond growth at pressures below one atmosphere<sup>12</sup>, pure films of diamond can be grown on substrates at appreciable rates.<sup>20</sup>

### **1.3.1 Substrates for diamond CVD**

Non-diamond substrates, such as silicon, are often used rather than diamond itself in CVD methods. Processes that enhance nucleation and initiate diamond growth are first carried out on the non-diamond substrates before deposition in the CVD reactor. The nucleation density of diamond on substrates capable of forming carbide layers, such as silicon, molybdenum and tungsten, is one or two orders of magnitude higher than the density on substrates that do not form carbide layers, such as copper and gold.<sup>15</sup> Silicon has a higher melting point than the temperature required for diamond growth and a thermal expansion coefficient similar to that of diamond. Combined with the fact that it is both inexpensive and readily available makes it a commonly used substrate for diamond CVD.<sup>2</sup>

The two methods commonly used to nucleate the silicon substrate are abrasion and seeding. In the abrasion approach, the substrate surface is damaged using a hard material, such as diamond itself, boron nitride (BN) or silicon carbide (SiC). The defects on the surface lower the free energy of the diamond deposition compared with graphite and result in the stabilisation of diamond nucleation. However, since this technique damages the substrate surface and is also less effective than seeding, nucleation using diamond seed particles is often favoured. Seeding involves the introduction of a layer of nanodiamond particles onto the substrate surface that form the foundation on which the diamond film will grow during the deposition.<sup>12</sup>

### **1.3.2 Mechanism of diamond CVD**

In a chemical vapour deposition process, deposition onto a solid substrate is the result of a gas-phase chemical reaction taking place above the surface. Typically the substrate has a temperature above 700 °C and is exposed to a gas mixture containing around 1% by volume CH<sub>4</sub> diluted in hydrogen. The presence of excess atomic hydrogen is essential to ensure the growth of diamond's *sp*<sup>3</sup>-carbon structure rather than graphitic *sp*<sup>2</sup>-carbon. In a hot-filament reactor the atomic hydrogen is generated by thermal decomposition of H<sub>2</sub> and in a

microwave reactor by electron impact dissociation of  $H_2$ . The atomic hydrogen promotes the growth of diamond over graphite in four ways in both CVD methods. Firstly, atomic H terminates the dangling bonds at the growth surface, maintaining the stability of the  $sp^3$  diamond lattice. H atoms also etch graphitic carbon more quickly than diamond-like carbon. Therefore,  $sp^2$  graphitic clusters are rapidly etched back into the gas phase. Atomic H also breaks up long-chained hydrocarbons, preventing their build-up in the gas phase and subsequent deposition onto the growth surface. Reactive radicals that can attach to vacant surface sites are also generated through the reaction of atomic H with neutral species, such as methane.<sup>1</sup>

The mechanism of diamond CVD is a complex system since there are many gas-phase and surface processes involved (Fig.5).<sup>12</sup>

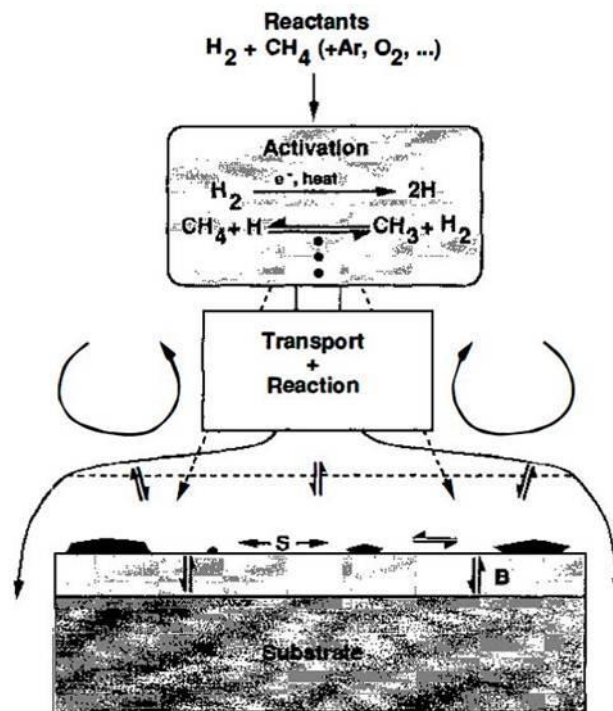


**Figure 5:** A schematic diagram of the main elements in the diamond CVD process. Reactants flow into the reactor, are activated by a thermal or plasma process, react and then are transported to the substrate surface where a number of surface processes occur and diamond is deposited. The dashed lines depict diffusion through a boundary layer and B depicts diffusion into the bulk. Image reproduced from reference 21.

Activation methods, such as the use of a hot filament or microwaves, are required in all CVD processes for synthetic diamond growth. This activates the carbon-containing reactant

gases, causing them to fragment into reactive radicals and atoms. The mechanism proceeds in a series of steps and is shown in **Fig.6**. A hydrogen radical that has been generated in the activation step removes a hydrogen atom from a  $sp^3$ -hybridised surface carbon atom to form  $H_2$ . This leaves a reactive carbon radical that can be attacked by a reactive gaseous methyl radical, adding a carbon atom to the lattice. This process can also take place at the adjacent carbon atom. Hydrogen from one of the newly bound methyl groups is then removed by another hydrogen radical. This generates another carbon radical, which attacks the adjacent carbon atom and forms a ring structure. This process continues until a diamond film with the desired thickness has been grown.<sup>1, 21</sup>

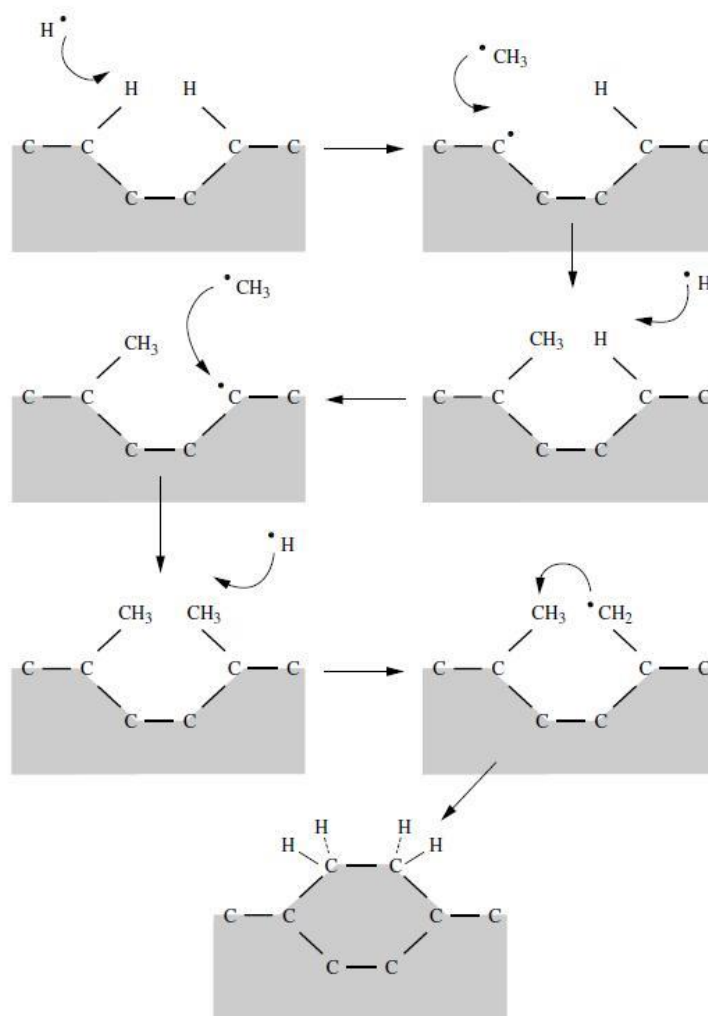


**Figure 6:** A schematic diagram showing the mechanism of CVD growth. Image reproduced from reference 1.

In the hot-filament method a tungsten filament is located just above the substrate and is electrically heated to around 2000 °C. The temperature of the substrate increases above 600 °C thanks to the thermal radiation from the filament. This activates chemical reactions, generating atomic hydrogen and methyl radicals, and these species then diffuse towards the surface of the substrate and cause spontaneous growth of a diamond layer.

Plasma-enhanced CVD uses radiation in the form of RF waves or microwaves to generate a hydrogen-hydrocarbon mixed-gas plasma in which the substrate is immersed. In microwave CVD the substrate often lies in a quartz tube that penetrates perpendicularly to a wave guide. A magnetron generates microwaves that are guided to the quartz tube and produces a plasma by exciting the gas molecules within the chamber.

The gas pressure in the chamber is typically 20-200 Torr in both CVD methods. Other hydrocarbon gases, such as ethane, ethylene and acetylene can be used as the source of carbon, in addition to the commonly employed methane.<sup>15</sup>

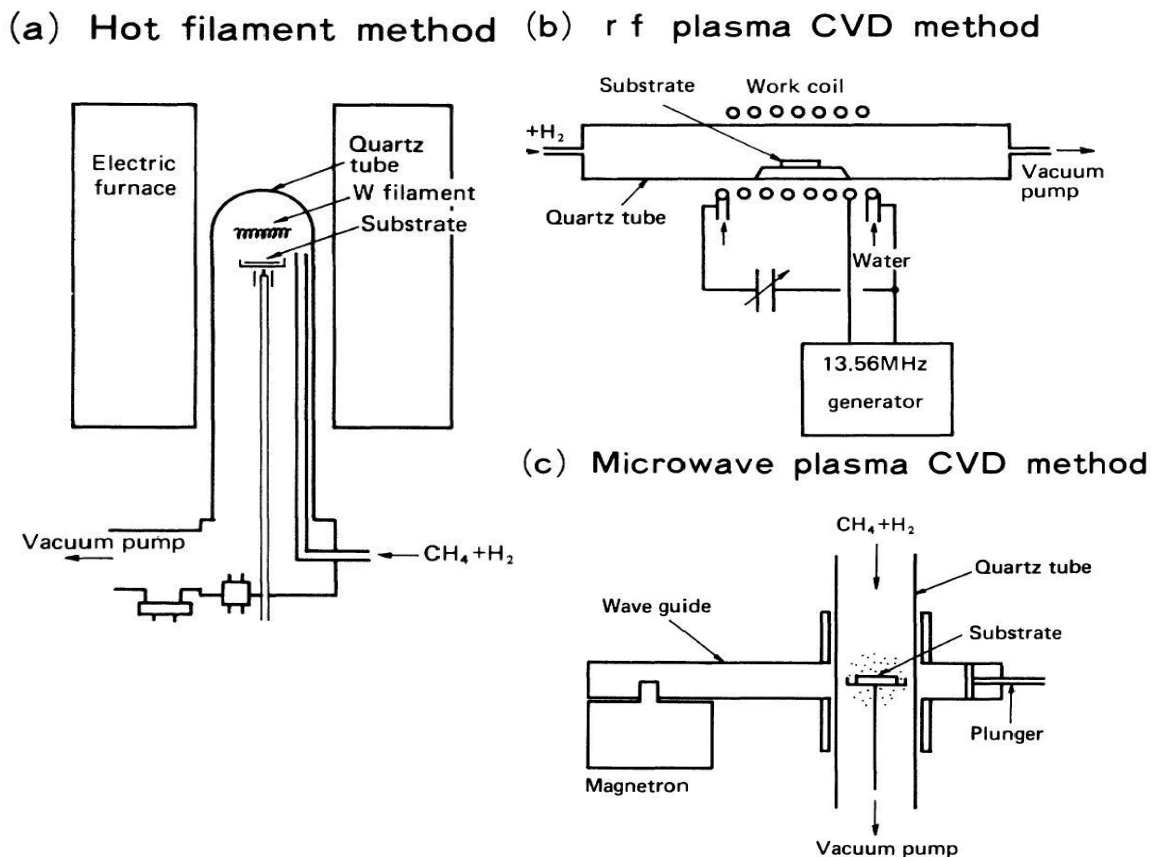


**Figure 7:** CVD methods for diamond synthesis using (a) hot-filament, (b) rf plasma, and (c) microwave plasma CVD activation. Image reproduced from reference 15.

In contrast, the etching of the diamond film once it has been grown presents substantial technical challenges due to both its hardness and chemical inertness.<sup>22</sup> When forming three-dimensional diamond structures using CVD, a solution lies in the use of silicon microfabrication methods, such as optical or electron-beam lithography and deep-reactive ion etching to make moulds. Polycrystalline diamond can then be grown into the silicon moulds, which are later removed using wet or dry etching techniques. This process has been used to generate free-standing diamond structures, such as lenses for the purpose of focusing high-energy x-rays.<sup>23</sup>

## **1.4 High-aspect-ratio structures with smooth, vertical sidewalls made from diamond and their application as x-ray optics**

The analysis of both soft and solid matter at the nanoscale is of great importance within many areas of science; from chemistry and physics to biology and material science. This can be achieved at synchrotron radiation sources where x-ray optics are required to focus the high-energy radiation onto the studied samples. Structures suitable for use as x-ray-focusing refractive optics must have high-aspect-ratio features with smooth and vertical sidewalls to prevent scattering of the x-ray radiation and lens aberrations. Current refractive lenses used at synchrotron sources are fabricated by deep etching silicon. However, with the increasing energy and brightness of synchrotron sources, x-ray optics must be manufactured that can withstand both the high temperatures and the intense radiation. For this reason, research has turned the attention to the use of diamond in generating such robust x-ray lenses. Diamond is a material often superior to silicon in many optical applications and is capable of forming transparent and strong structures that also possess a very low thermal expansion coefficient. The low thermal expansion coefficient of diamond ensures the x-ray optics can withstand the powerful x-ray beams generated by third and fourth-generation light sources whilst still focusing hard x-rays down to less than 500 nm.<sup>24, 25, 26</sup>

### **1.4.1 Synchrotron radiation**

Electrons or positrons moving along a curved trajectory with a large radius of curvature at relativistic velocities emit electromagnetic radiation.<sup>27</sup> Very intense beams of x-rays and

both infrared and ultraviolet light, collectively termed synchrotron radiation, can be generated at synchrotron sources.<sup>28</sup>

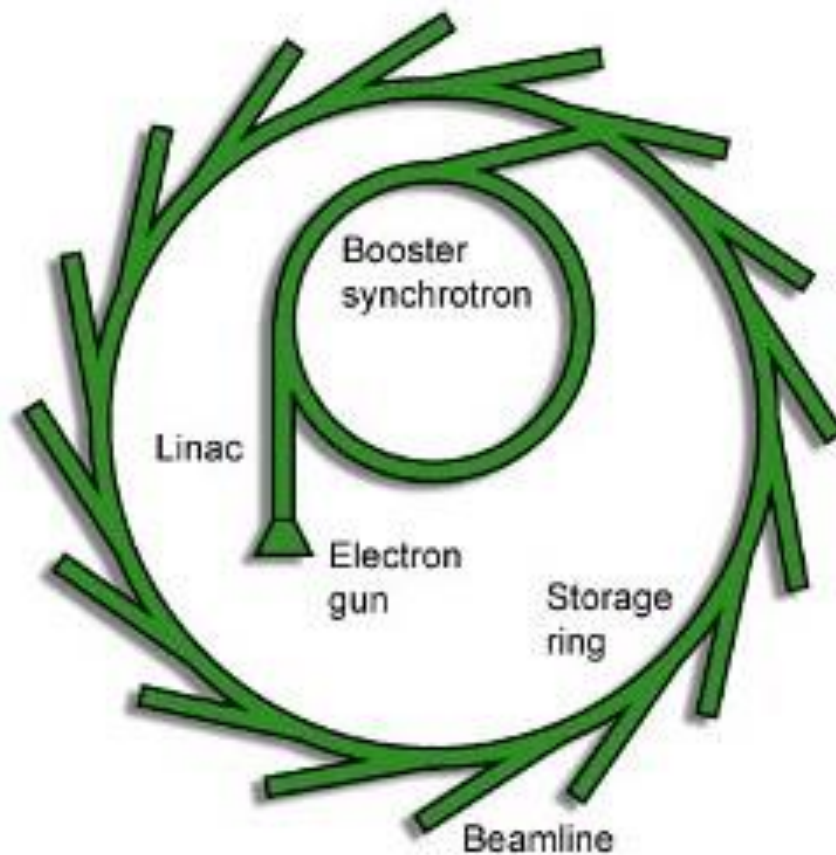


**Figure 8:** Schematic diagram of a synchrotron instrument. Image reproduced from reference 28.

The storage ring and the beamlines are the two main components of instruments used to generate synchrotron radiation. Charged particles are injected into the storage ring and accelerated to velocities nearing the speed of light. The storage ring is made up of bending magnets, which steer the electrons around the ring and keep them moving at relativistic velocities, under vacuum, in a closed orbit. At each bending magnet, synchrotron radiation is emitted and channelled into the experimental beamlines. The particular photon energy that is needed for an experiment can be selected and collected by a specific beamline.<sup>27, 28</sup>

## 1.4.2 Refractive x-ray lenses

Refracting x-rays is problematic because the refractive index,  $n$ , is almost one in most materials.<sup>29</sup> The refractive index for x-rays in matter is dependent on the refractive index decrement,  $\delta$ , and is described by equation 1, where  $i\beta$  is the imaginary part of the refractive index.

$$n = 1 - \delta - i\beta \quad \text{Equation 1}$$

$\delta$  is typically  $10^{-6}$  for hard x-rays and  $\beta$  is much smaller than one, which means that  $n \approx 1$ .

The focal length,  $f$ , of a lens depends on the radius of curvature,  $R$ , and both the number of refractive surfaces,  $N$ , and the refractive index decrement,  $\delta$ , according to equation 2.

$$f = \frac{R}{2N\delta} \quad \text{Equation 2}$$

Therefore, the focal length required to refract x-rays using a single lens ( $N = 1$ ) is large and since the real part of  $n$  is smaller than one, an x-ray refractive lens must also be concave.<sup>30</sup>

The problems associated with focusing x-rays with refractive lenses are solved by using either a compound refractive lens (CRL) design ( $N > 1$ ) or a kinoform lens design, both of which can achieve focusing with high resolution and high transmission. Therefore, the fabrication of high-aspect-ratio lens structures with smooth sidewalls that can function as CRL or kinoform optics is of great interest to synchrotron science. Today, these hard x-ray optics are fabricated from silicon and beryllium since high-quality focusing optics require the lens material to be precisely sculpted and this can be challenging in diamond. However, transmission of the lens material increases as the atomic number decreases. Therefore, it is clear that diamond, with a  $Z$  value of 6, is a superior material compared to silicon, with a  $Z$  value of 14, for the purpose of x-ray lens fabrication. Beryllium has a low  $Z$  value but it is not very abundant, is difficult to machine and produces toxic oxides when exposed to high-powered x-ray beams. As a result it is not ideal to be used in industrial processes.<sup>31</sup>

Compound refractive lenses consist of a series of parabolic, concave surfaces with a small radius of curvature, stacked together to enable the focusing of x-rays at a reasonable focal length.<sup>30</sup>

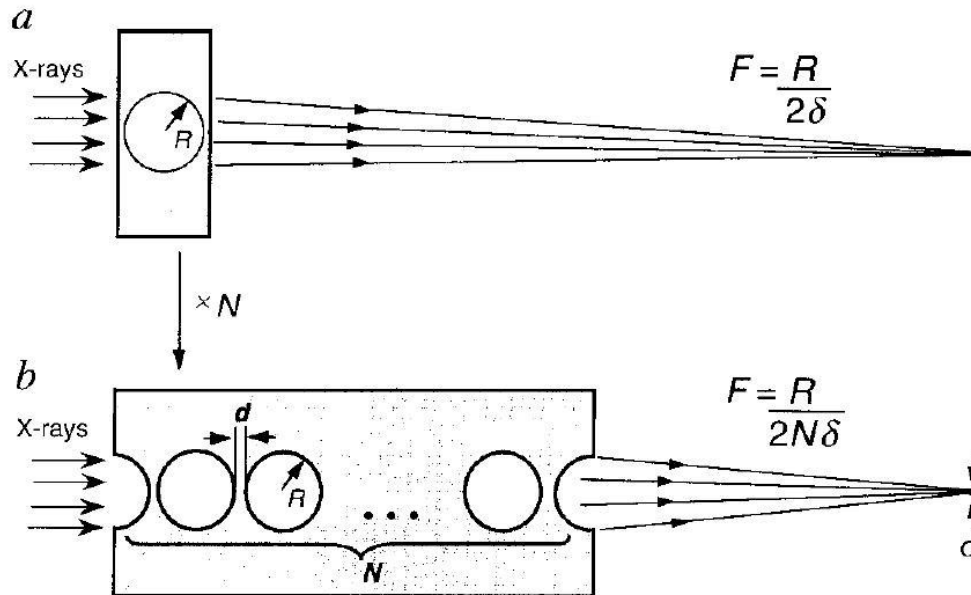


**Figure 9:** Schematic diagram showing (a) a single lens refractive optic and (b) a CRL. The focal length decreases with an increasing number of lenses,  $N$ . Image reproduced from reference 32.

Higher numbers of refractive surfaces making up the CRL increase the distance the x-rays have to travel within the lens and, hence, the more absorption that takes place. For this reason, kinoform designs are often preferable to CRLs since they are designed to minimise absorption.

The kinoform lens has a single elliptical focusing surface that can function with a short focal length, due to the small radius of curvature, and exhibits high transmission. The issue of excessive x-ray absorption experienced by other lenses is avoided by removing material whilst maintaining the lens shape and focusing properties.<sup>24, 25, 26</sup>

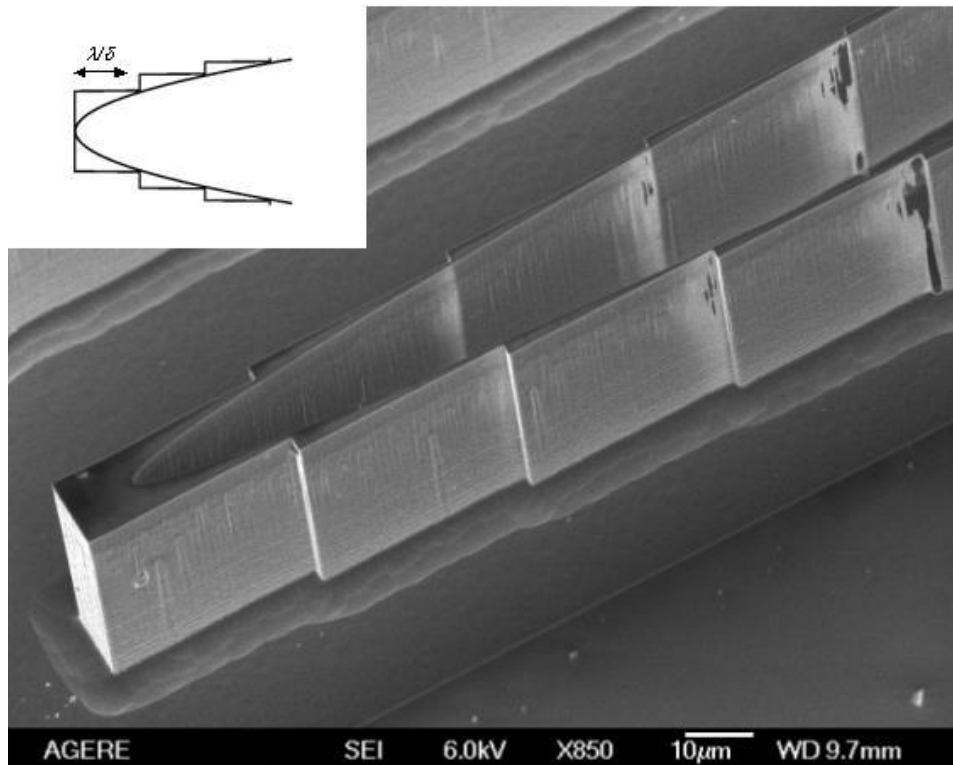


**Figure 10:** Silicon kinoform lens with an inner elliptical focusing surface and an outer stepped surface where lens material has been removed to minimise absorption. Inset: schematic diagram of a kinoform lens. Image reproduced from reference 26.

The removal of sections of the lens material yields an improved transmission compared to the solid refractive optic. Material with dimensions corresponding to integer multiples of  $\frac{\lambda}{\delta}$  is removed, where  $\lambda$  is the operating wavelength. The removed segments correspond to multiples of the  $2\pi$  phase shift at the operating wavelength, leading to an improvement in transmission without compromising the behaviour of the corresponding solid optic.<sup>31</sup>

## 2 Deep reactive ion etching of silicon for the fabrication of high-aspect-ratio structures

The introduction of inductively coupled plasma (ICP) reactors for the purpose of silicon reactive ion etching (RIE) less than twenty years ago led to the development of deep reactive ion etching (DRIE). Changes to hardware and processing since then have led to more selective DRIE methods which are capable of etching features with high aspect ratios at a higher etching rate, whilst also reducing the commonly observed undesirable features

of DRIE, such as notching, scalloping and aspect ratio dependent etching (ARDE). The main benefit of these technologies lies in the microfabrication of high-aspect-ratio microstructures (HARMS) that have many applications as micro-electro-mechanical systems (MEMS). Deep reactive ion etching of silicon is also an important process for producing moulds for refractive x-ray lenses from diamond as diamond itself is too hard and chemically inert to be easily etched.

There are two main ways in which HARMS are fabricated using DRIE methods: the Bosch process and the cryogenic process<sup>33</sup>, both of which have their own advantages.

## **2.1 The Bosch process**

The original patent for the silicon etch process, known today as the Bosch Process, was filed in 1994 by employees at Robert Bosch GmbH and this new etching method very quickly developed a fundamental role in the silicon microfabrication field.<sup>34</sup>

The Bosch process is a two-step technique for anisotropic etching and is the foundation of many modern methods to form deep etches in silicon. To begin with, a patterned mask layer, that is selective and so will not be etched under the particular etching conditions, is deposited on the substrate. A cyclic deposition/etching process then takes place in an ICP system. During the deposition step a Teflon-like polymer layer is deposited using a gaseous fluorocarbon, such as  $C_4F_8$ <sup>35</sup>, and this protects the surface and sidewalls of the substrate from being etched.<sup>36</sup> This is followed by the etching step during which attack of the substrate by a fluorine-containing gas (commonly  $SF_6$ ) etches the silicon. The generation of an electric field in the etch step through application of radio frequency (RF) power on the substrate causes ion bombardment at the bottom of an etch feature.<sup>35</sup> As a result, the polymer layer is removed from the bottom of the etched feature whilst the passivation layer on the sidewalls remains intact.

Repetitive alternation of these deposition and etching phases leads to the substrate being etched at the bottom of the trench until an anisotropic etched feature with a desired depth is reached.<sup>36</sup>

## Standard Bosch Process

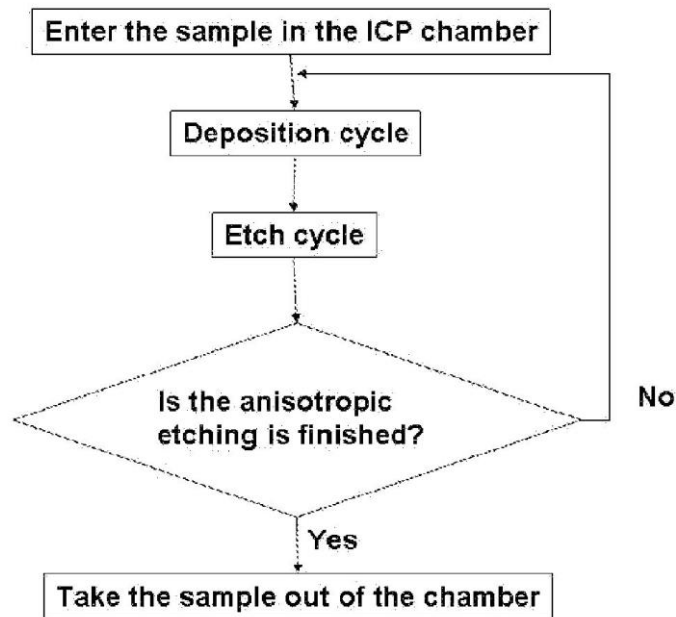


**Figure 11:** Flow diagram of the standard Bosch process. Image reproduced from reference 35.

## 2.2 The cryogenic process

As with the Bosch process, the cryogenic process consists of two steps; firstly the deposition of a passivation layer, which is followed by an etching step. The most frequent etching gas used in both processes is  $\text{SF}_6$  and it is only in the sidewall passivation and mask layer protection mechanisms where the differences arise.<sup>37</sup> During the cryogenic process the temperature of the silicon substrate is reduced to about  $-100\text{ }^\circ\text{C}$ , which promotes the formation of a  $\text{SiO}_x\text{F}_y$  passivation layer on the sidewalls and prevents attack of this layer by the fluorine radicals generated in the etch gas. This leads to a more anisotropic etch thanks to a reduced etch rate at the passivation layer.<sup>38</sup> The main advantage of this process is the formation of very smooth sidewalls. Therefore, the cryogenic process is often the leading technology in nanoscale etching where sidewall smoothness is paramount.<sup>37</sup>

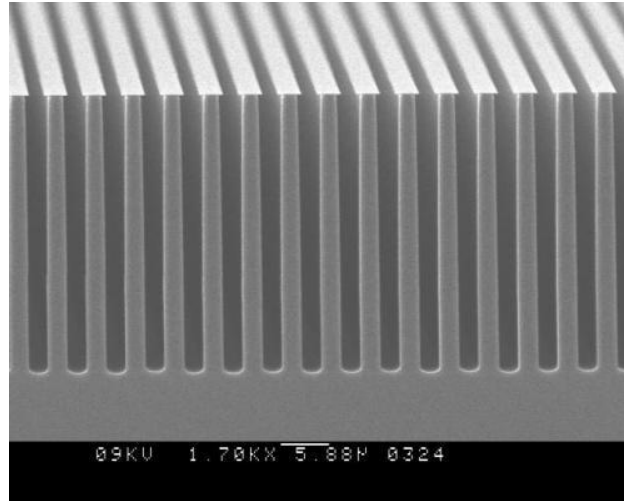


**Figure 12:** Etched features in silicon with very smooth sidewalls produced using the cryogenic process. Image reproduced from reference 37.

### 3 Problems arising from standard DRIE processes

In many cutting-edge nanotechnology applications, smooth sidewalls, high aspect ratios, high etch rates and high selectivity to standard mask materials, such as photoresist and silicon oxide, are the requirements of high-performance deep silicon etch (DSE) technologies.<sup>39</sup> For example, sidewall verticality and smoothness are vital if the etched silicon is to be used as a mould for CVD of diamond optics, since surface roughness can cause scattering of radiation.<sup>2</sup> There are a number of disadvantageous features that are commonly experienced when using a standard DSE process, including sidewall scalloping, notching and aspect ratio dependent effects. These impact the quality of the etch and so must be addressed when designing equipment to carry out deep etching of silicon.

#### 3.1 Sidewall scalloping

Scalloping of the sidewalls of deep trenches results directly from the repetitive nature of the alternating passivation layer deposition and etch steps (see **Fig.13(d)**). After the passivation step, fluorine ions travel vertically down the etch structure, colliding at the bottom of the trench. These collisions remove the passivation layer and leave it exposed to the etchant gas. Longer cycles increase etch rate but also enhance scalloping<sup>36</sup> and, therefore, the ratio of the etch time to the passivation time is important. The etch rate increases as the length of the passivation cycle decreases as there is less time to deposit the passivation layer at the

base of the etch feature and therefore less material to remove in the etch step. As a result, more of the etch cycle is spent etching silicon and the etch rate increases. While increasing etch rate, decreasing the passivation cycle time also enhances sidewall scalloping so is not always feasible.<sup>40</sup> A ratio must be found that maintains an appreciable etch rate while keeping sidewall scalloping to a minimum.

### **3.2 Notching and undercutting**

Notching and undercutting at the etch entry, caused by flaring at the oxide (etch stop) layer, are often seen when etching silicon-on-insulator (SOI) structures used for 3D-MEMS production.<sup>36</sup> Undercutting is observed when the top of the trench begins to be etched laterally by the chemical reaction (see **Fig.13(c)**). Notching occurs when the etch reaches the silicon/insulator interface and the conductive current path is broken leading to charge separation (see **Fig.13(a)**). Arriving ions flow towards the sidewall and etch laterally instead of vertically.<sup>41</sup>

### **3.3 Aspect-ratio dependent etching (ARDE) effects**

ARDE features arise because the etch rate is often inversely proportional to aspect ratio. Since the ions do not always travel vertically and get deflected through collisions with nearby gas molecules, their concentration decreases towards the bottom of deep trenches. Therefore, the passivation layer removal process is slowed and this leads to a reduction in the length of time that the silicon is exposed to the etch gas in the etching step. Similarly, the concentration of the etch gases decreases as the depth increases leading to a reduction in the silicon etching step. This reduction in ion bombardment and gas transport at the bottom of deep and narrow features results in a slower etch rate with increasing trench depth. Consequently, there is a narrowing of trenches, sometimes the etch is stopped completely and the maximum aspect ratio is limited.<sup>42</sup>

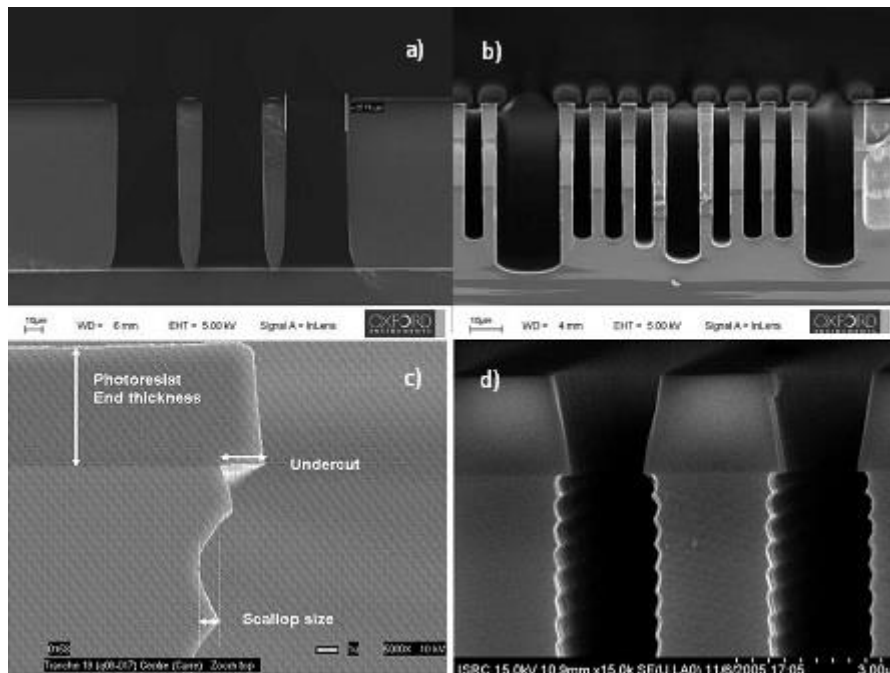


**Figure 13:** Scanning electron microscope (SEM) images showing the four main problems that can occur in DRIE processes (a) notching (b) effects of ARDE (c) undercutting at the top of the etch feature (d) sidewall scalloping. Image reproduced from references 35, 36, 37.

## 4 Current technologies for etching high-aspect-ratio silicon structures with smooth and vertical sidewalls

Today the leading companies producing DSE systems, such as Plasma-Therm and Oxford Instruments, have developed equipment to minimise or eliminate the problems of sidewall scalloping, notching and ARDE and meet the needs of an increasingly demanding market.

### 4.1 Surface Technology Systems

#### 4.1.1 Adjustment of the standard Bosch process

Etch rate is an important factor to be considered if an industrial process is to be economically viable. The etch rate of the standard Bosch process can be altered in four ways:

- Increase the etch cycle pressure to between 40 mTorr and 1000 mTorr.
- Increase the ratio between the etch time and the deposition time in each cycle.
- Increase the flow rate of the etchant gas.

- Use high RF power on the ICP antenna to promote dissociation of the etchant gas.

Unfortunately all of the above measures generally result in a higher degree of scalloping of the sidewalls, which can be more detrimental than a faster etch rate is beneficial. Through continual improvement of the Bosch process over time, Surface Technology Systems (STS), the original licensee of the process in 1994<sup>34</sup>, has developed a method in which high pressure can be used to maintain a high etch rate.

As the mean free path of an ion is inversely proportional to pressure, increasing the pressure reduces the density of ions that are accelerated without collision in the plasma. Collisions in the plasma slow the ions, causing them to reach the bottom of the etch feature later. This means that at the beginning of each etch cycle it takes longer to remove the deposited passivation layer from the preceding deposition cycle. As a result there is a greater degree of wall etching and roughness of the bottom surface. Altering the standard Bosch process by adding a third step to the cycle gives the STS '3-Step Method' used today:

1. Deposition cycle
2. Etch removal step
3. Main etch step

Step 2 is carried out at a low pressure of between 5 mTorr and 40 mTorr and a high RF power. In contrast, step 3 is carried out at a lower power that gives higher selectivity to the mask layer. High pressure can now also be used in this step since deposition on the bottom of the etch feature is removed during the second step. This increases the etch rate without causing the aforementioned problems attributed to use of a high pressure.<sup>35</sup>

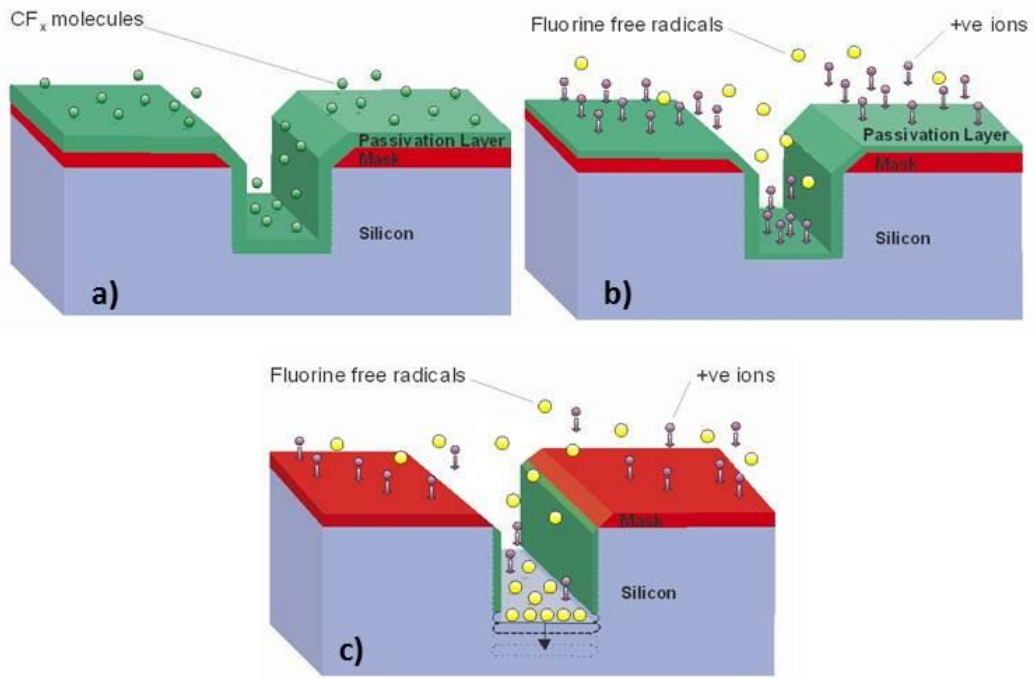


**Figure 14:** Schematic diagram of the DRIE process used by STS a) passivating polymer layer deposited on all surfaces by  $C_4F_8$  plasma b) horizontal surfaces bombarded by cations in  $SF_6$  plasma, etching the passivation layer and exposing the mask layer/substrate c) silicon at the base of the feature is isotropically etched by the fluorine free radicals in the  $SF_6$  plasma whilst sidewalls remain protected by passivation layer. Steps (a)-(c) are repeated continually until the desired trench depth is achieved. Image reproduced from reference 34.

#### 4.1.2 STS products for DRIE of silicon

Current products available from STS are capable of etch rates exceeding  $30 \mu\text{m min}^{-1}$  and can produce aspect ratios greater than 90:1 (ratio of the height of the etch feature to its width). The Pegasus Rapier Module from STS etches silicon using Bosch switching processes. It boasts a patented dual plasma source design in which the primary and secondary plasma zones are decoupled, enabling independent control and gas supply. As a result, radical distribution is uniform and highly concentrated giving a fast etch rate, controlled tilting of deep features across the substrate and very good uniformity. Furthermore, oxide etching using the same hardware is also possible with multi-mode flexibility.<sup>43</sup> STS also offers a unique and patented ‘parameter ramping’ technology using its Morflex™ software, with which plasma conditions can be continuously altered throughout the etch process in order

to overcome ARDE effects. This software and the Pegasus Rapier model are combined specifically for the fabrication of deep, vertical, high-aspect ratio features at a high rate.<sup>44</sup>

## **4.2 Plasma-Therm**

Since its founding in 1975, the company Plasma-Therm has become a leader in the supply of plasma processing equipment and, like STS, also makes use of a three-step version of the original Bosch process. In the two step method the passivation-layer removal and isotropic etch are incorporated into the second step that means it is difficult to achieve independent optimisation of each process. As a consequence, etching machines which do not deviate from this method typically suffer from poorer etch selectivity.

The Versaline® DSE is an etching system developed by Plasma-Therm that incorporates a number of patented processes and modern technologies, which give it several advantages over competing companies.

Firstly, gas switching, using a set of hardware and software that works to achieve optimum switching times, is employed to minimise the scalloping of trench sidewalls. Control of the etch rate, mask undercut, SOI notching, ARDE and etch selectivity is then achieved through control of the process parameters, such as power, pressure and temperature. The process morphing™ programme alters these process parameters automatically throughout the etch process in order to improve profile control and fabricate near vertical structures with minimal undercut. By providing higher gas flow, pressure and RF power, Plasma-Therm etching products are also able to meet the demands for increased performance and faster etch rates. Furthermore, substrate temperature is an additional parameter that needs to be strictly controlled to ensure high uniformity and repeatability. Excess heating of the substrate caused by faster etch rates is potentially problematic. Typically the centre of the substrate gets hotter, leading to higher deposition rates in this area and a consequent loss of etch uniformity. To solve this problem, Plasma-Therm products incorporate a closed-loop controlled cooling chuck that dissipates heat from the wafer during the process.

SOI substrates, which have an oxide layer on the silicon acting as an etch stop, are often etched using DSE to create 3D-MEMS structures. Since the combination of SOI and DSE can be very powerful, the Versaline® DSE system makes use of a patented technology which prevents notching and undercutting. An integrated endpoint detection feature using optical

emission spectrometry (OES) is also used and detects when the etch stop layer has been reached, stopping the etch and reducing over-etching.

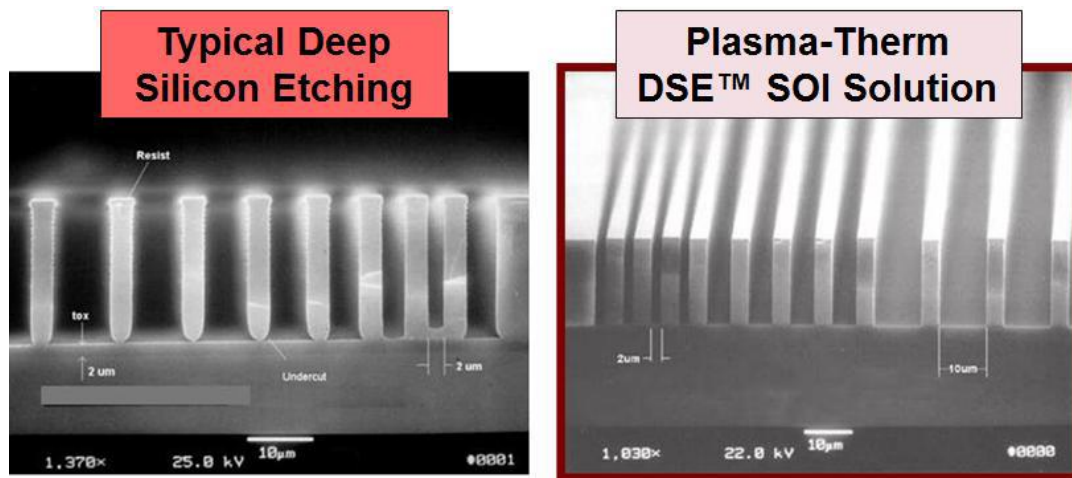


**Figure 15:** Comparison of the processing of SOI structures using the typical DSE process and the Plasma-Therm Versaline® DSE system. Image reproduced from reference 36.

Through use of process controls that yield higher efficiency results and etch features of uniform depths, and conversion of pressure bursts on the transition from the passivation step to the etching step into a smooth pressure transition, Plasma-Therm has been able to eliminate ARDE effects and increase the reproducibility of results.<sup>36, 45, 46</sup>

### 4.3 Oxford Instruments

The requirements of a modern etching system are also met by the Oxford Instruments PlasmaPro Estrelas 100 machine shown in **Fig.16**.



**Figure 16:** PlasmaPro Estrelas 100 tool from Oxford Instruments. Image reproduced from reference 39.

Configured for both the Bosch and cryogenic deep silicon etch processes, the PlasmaPro Estrelas 100 instrument can provide both micro- and nanoscale etching in the same reaction chamber.<sup>47</sup> This instrument achieves high selectivity because the core processes are once again carried out in a three-step cycle based upon the Bosch process. The higher RF powers and rates of gas flow provide more fluorine radicals to increase the etch rate and the excess substrate heating is addressed by the improved substrate cooling. A reduction in scallop size, and therefore smoother sidewalls, is obtained through shorter cycle steps whilst improved pumping and chamber design maintain etch rates. Further improvement to the removal of the etched products allows structures with higher aspect ratios (up to 70:1) to be generated. Overall, the PlasmaPro Estrelas 100 machine achieves an improvement in switching speed, selectivity and etch rate in comparison with other systems.<sup>39</sup>

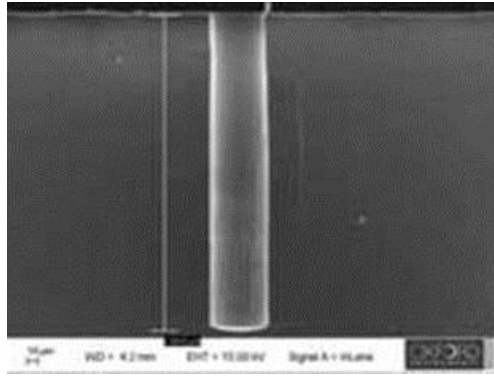


**Figure 17:** SEM showing a 50  $\mu\text{m}$  deep silicon trench etched at a rate of 16  $\mu\text{m min}^{-1}$  by the PlasmaPro Estrelas 100 instrument. Image reproduced from reference 39.

#### **4.4 Unaxis Wafer Processing**

Unaxis Wafer Processing offers innovative technology in the field of deposition and etching.<sup>48</sup> The increasing use of SOI substrates for the production of MEMS led to the Unaxis DSE™ III SOI hybrid process. Using a modified Bosch process and a novel three-step technique, consisting of a bulk etch, OES end-point detection and a finishing etch, this equipment has focused on the elimination of notching in the DSE process. Since any exposure of the oxide layer to the plasma during the bulk etch period will cause notching, the OES end point detector detects the initial oxide exposure and prevents the etch from continuing. Using this proprietary DSE technique, notching is completely absent in features with aspect ratios up to 8:1 and significantly reduced to less than 200 nm in those with aspect ratios up to 25:1.<sup>41</sup>

### **5 Comparison of the technologies offered by Plasma-Therm and Oxford Instruments**

There are similarities and differences between the Versaline® DSE from Plasma-Therm and the PlasmaPro Estrelas 100 from Oxford Instruments machines used for deep silicon etching. Both systems reduce scalloping through use of shorter deposition and etch cycles and tune the RF power and pressure to increase etch rate and minimise ARDE effects. Similarly, the increased temperature, a direct consequence of a faster etch, is addressed by both systems through improved substrate cooling. However, there are subtle differences between the two instruments that make them engineered for slightly different purposes. Whilst both

machines work on an optimised three-step version of the Bosch process, the PlasmaPro Estrelas 100 is also able to carry out the cryogenic process, making it suitable for deep etching on both the micro- and nano-scale. On the other hand, the Versaline<sup>®</sup> DSE tool is more effective for the production of 3D MEMS since it has an incorporated patented technology in order to reduce notching and undercutting associated with etching SOI substrates. The repeatability of results with the Versaline<sup>®</sup> system is also enhanced thanks to the elimination of pressure bursts.

To be beneficial to researchers the equipment needs to be readily accessible for use by those who require deep silicon etching processes. The two systems discussed above can be accessed in two different centres in the UK: Southampton Nanofabrication Centre and the James Watt Nanofabrication Centre. These are two state-of-the-art facilities that provide etching capabilities for use in the field of nanotechnology. Southampton Nanofabrication Centre is home to a Plasma-Therm Versaline<sup>®</sup> DSE system and serves both commercial and academic clients. Not only does the centre use this tool to fabricate devices for application in electronics, nanotechnology and bio-nanotechnology, but it is also available to be used by researchers.<sup>49</sup> Kelvin Nanotechnology supplies a range of commercial nanotechnology services delivered through the James Watt Nanofabrication Centre at the University of Glasgow. They use the latest Oxford Instruments dry etching and deposition systems to supply etched silicon wafers for use in a variety of industries including electronics, optics, sensors and biomimetics.<sup>50</sup>

## **6 Reactive ion etching of high-aspect-ratio structures in diamond**

Diamond proves difficult to etch due to its intrinsic hardness and chemical inertness and this is why it can be preferential to obtain diamond structures using etched silicon moulds. However, there is a method which enables the successful etching of diamond with high aspect-ratio, smooth features.

Like the silicon etch, the technique used for dry etching diamond is the reactive ion etching (RIE) process. The diamond surface is covered with a patterned mask, such as aluminium, and etched in an RIE inductively coupled plasma reactor in the same way as silicon substrates. The differences between silicon and diamond etching lie in the mask material and the gas mixture used. Metals such as aluminium and chromium and their alloys must

form the hard masks in diamond etching since a photoresist is not suitable, while  $\text{CF}_4$  or  $\text{CHF}_3$  gas replaces the conventional  $\text{SF}_6$  used in silicon etching as this yields higher selectivity. Any fluorine gas in the plasma reduces the selectivity of the diamond etch versus aluminium but some is always present as it increases the etch rate and sidewall smoothness. Typically the gas mixture also contains oxygen to provide radicals which, combined with ion bombardment, are able to break the strong carbon-carbon bonds present in diamond and allow etching to take place.<sup>51, 52, 53, 54</sup>

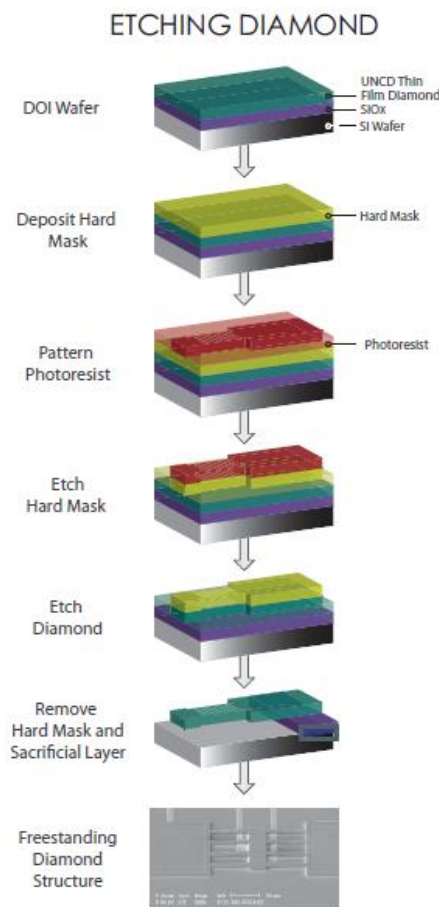


**Figure 18:** Schematic diagram showing the process of a diamond etch using RIE. Image reproduced from reference 55.

The technology that provides the solution to the problems faced when etching diamond is provided by Oxford Instruments in their RIE/-ICP systems, such as the PlasmaPro 100 Etch & Deposition Tool.<sup>56</sup> Kinoform lenses from diamond with vertical sidewalls and minimal diamond grass have been successfully synthesised by Isakovic, *et al.* using this instrument, achieving a focal spot size of approximately  $1 \mu\text{m}$  with a single kinoform lens working at  $E = 11.3 \text{ keV}$ ,  $f = 0.2 \text{ m}$ .<sup>31</sup>

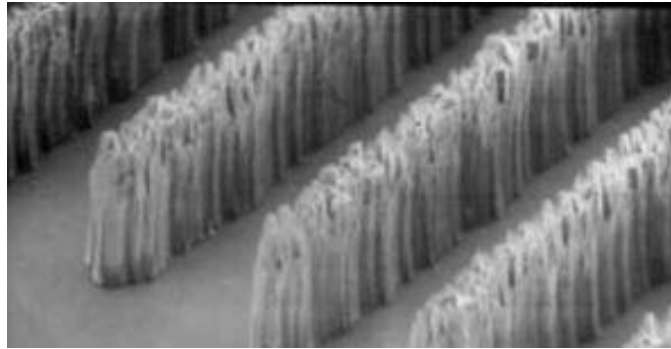


**Figure 19:** SEM image showing etched diamond features with a depth of 10  $\mu\text{m}$  generated by an Oxford Instruments etch system at a rate of  $500 \text{ nm min}^{-1}$ . Image reproduced from reference 56.

From the SEM image in **Fig.19** it is evident that a mould process would often be preferable to etching the diamond itself as the sidewall roughness and selectivity is very poor, since the resulting structure does not perfectly match the mask.

## **7 Selected-area, self-assembly nucleation of nanodiamond particles**

### **7.1 Electrostatic self-assembly**

Before a substrate can be subject to a diamond chemical vapour deposition process it must be thoroughly cleaned, to remove any trace of organic or inorganic contaminants, and then nucleated with nanodiamond particles. The electrostatic self-assembly nanodiamond nucleation method yields a high nucleation density and is hence a commonly used method for seeding non-diamond substrates prior to CVD. A process has been formulated involving two polymer layers, one of poly-diallyldimethyl ammonium chloride (PDPA) and the other of poly-sodium 4-styrene sulfonate (PSS), which has proved to be very effective at applying nanodiamond seed particles to a substrate and is often adopted as the standard procedure. Both strong polyelectrolytes across a wide pH range<sup>57</sup>, PDPA and PSS are ideal polymers in the layer-by-layer self-assembly process since the driving force is electrostatic interaction.<sup>58</sup>

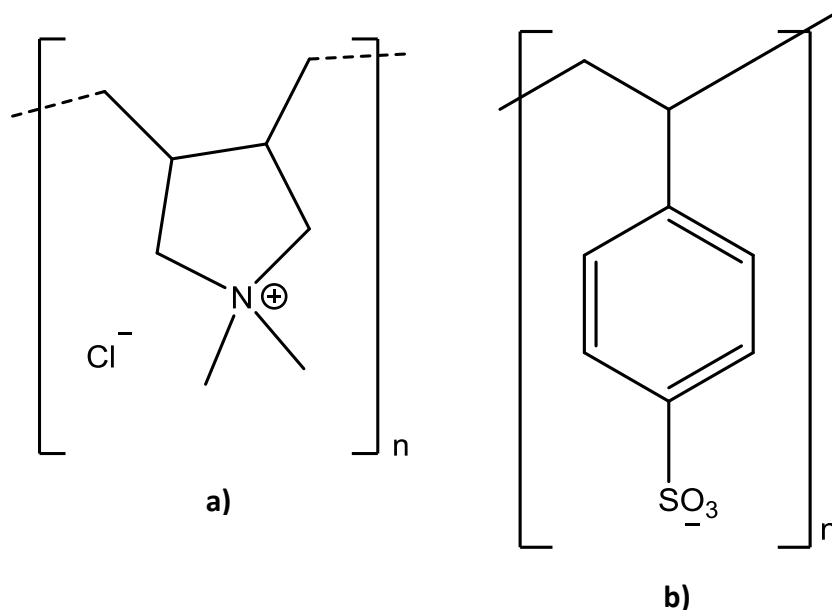


**Figure 20:** Schematic drawings of a) a monomer unit of the cationic polymer PDDA and b) a monomer unit of the anionic polymer PSS.

An anionic Si (100) substrate is coated with the cationic PDDA solution and cationic nanodiamond (ND) particles are coated with the anionic PSS. A Si (100) / PDDA / PSS / ND seed layer structure is then formed by immersion of the now cationic, polymer-treated substrate into the anionic PSS-ND solution at room temperature and pressure.<sup>59</sup> The procedure begins with the substrate rinsed sequentially with deionised water, acetone, ethanol and methanol and dried with compressed air between solvents. The substrate is then fully submerged in a PDDA solution (10 w/v %) for 10 min and then rinsed with deionised water and dried. It is then submerged in a PSS-ND (10 w/v %) for 60 min and rinsed and dried again.<sup>60</sup>

## 7.2 Selected-area diamond nucleation

Patterned diamond films have many applications in micromechanics, microelectronics and biosensors.<sup>61</sup> Fabrication of these films requires the substrate to be selectively nucleated so that diamond deposition takes place on certain areas only.

One way to achieve selective nucleation is through the use of photolithography. A photoresist layer is applied to the substrate using spin-coating apparatus and then lithographically patterned. The normal self-assembly seeding procedure is then carried out, followed by the removal of the photoresist layer in a lift-off solution, such as acetone. This

leaves nanodiamond seed particles on the patterned silicon area only and therefore selective diamond deposition results when the substrate is placed in a chemical vapour deposition reactor. This method has been successfully carried out by Albin *et al.* to generate a diode for use in diamond electronics.<sup>61, 62</sup> Ha *et al.* have used a mask layer of SiO<sub>2</sub> and the above procedure to also achieve selective nucleation and deposition.<sup>63</sup>

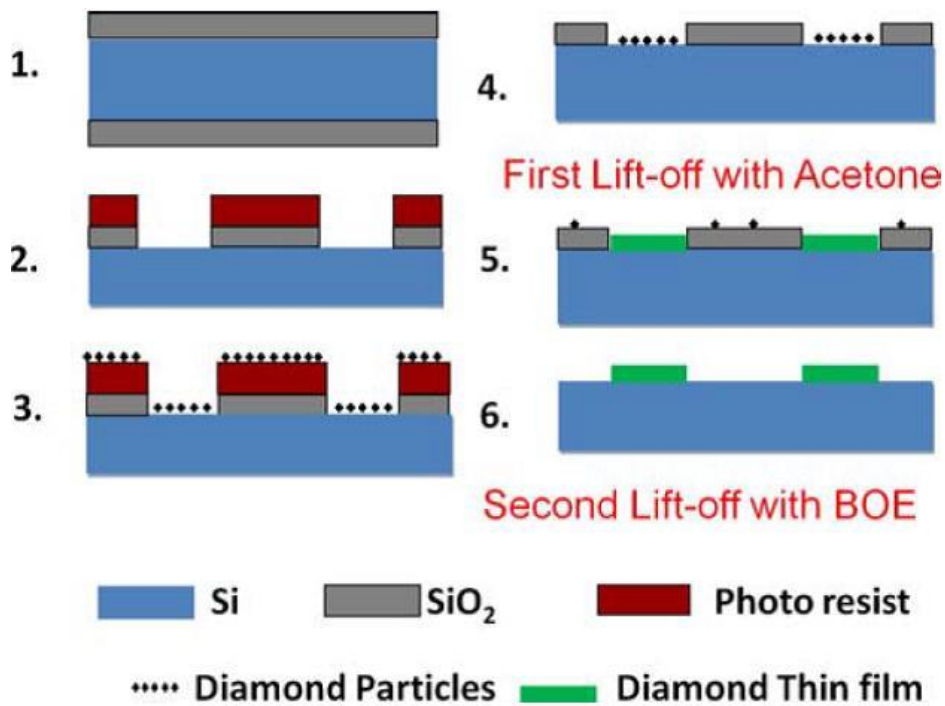


**Figure 21:** Schematic diagram showing the selected-area nucleation process used by Albin *et al.* to generate a diamond diode. Image reproduced from reference 62.

An alternative approach to photolithography is patterning by ultrasonic treatment, which is carried out in one of two ways. Ultrasonic bombardment of nanodiamond particles is used to nucleate the sample in both methods. The patterned mask layer is either applied before nucleation and then removed before deposition, taking the seed layer with it, or after the whole substrate has been seeded. In the latter case, the mask remains in place during deposition, selectively burying some of the nucleation sites, and is then removed once diamond has grown in the unmasked regions.<sup>61</sup>

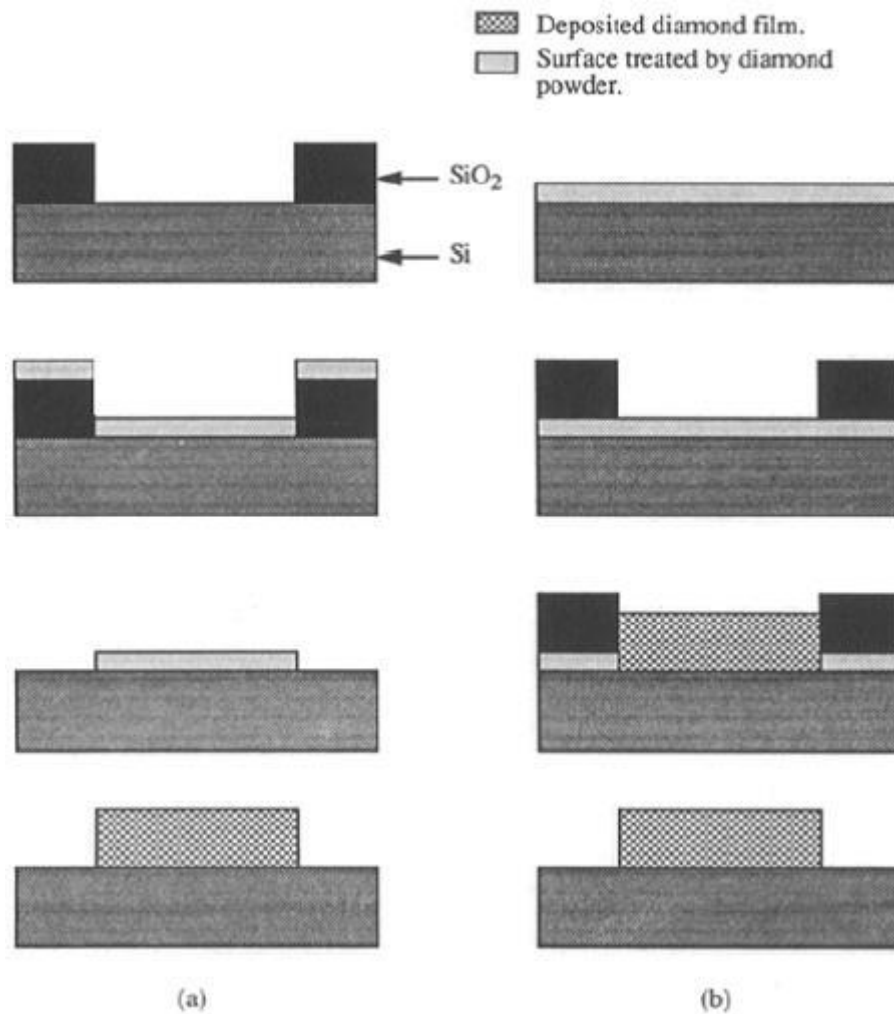


**Figure 22:** Schematic diagram showing the process of ultrasonic treatment where the mask layer is applied either (a) before diamond growth or (b) after nucleation has taken place. Image reproduced from reference 61.

The final method for patterning diamond structures is the etching of diamond films in oxygen. This method differs from the other two in that the substrate is non-selectively seeded and grown on. The patterned mask layer is then applied on top of the grown film and exposed to an oxygen plasma. Since diamond readily undergoes oxidation at high temperatures, the exposed areas of the diamond layer are etched away whilst the mask layer remains intact. The resist layer can then be later removed using a wet etching technique, such as etching in hydrofluoric acid, leaving a patterned diamond film.<sup>61</sup>

## **8 Aims of the nanodiamond selected-area, self-assembly nucleation project**

The aim of this investigation is to optimise the selected-area, electrostatic self-assembly nucleation method, used to seed substrates with a layer of nanodiamond particles, in order to obtain a uniform seed layer and the highest density of nanodiamond nucleation sites. The seeded substrate can then be grown on in a microwave CVD reactor to produce a polycrystalline diamond layer. The optimised process will then be applied to a lens-mould substrate to generate a freestanding, high-aspect-ratio refractive optic from diamond, for focusing hard x-ray beams generated at synchrotron sources.

## 9 Experimental Method

### 9.1 Electrostatic self-assembly of nanodiamond particles

In order to achieve the best uniformity and nucleation density from the electrostatic self-assembly method, the standard operating procedure detailed in the thesis by E. Tofts<sup>60</sup> and described above in **Section 7.1** was largely followed. In summary, the substrate was first thoroughly cleaned with a series of solvents to ensure all contaminants were removed before it was immersed in the cationic PDDA solution for 10 minutes. After removal and subsequent rinsing with DI water and drying, the substrate was immersed in the anionic PSS-ND solution for 1 hour. The substrate was then once again removed, rinsed with DI water and dried. The only change made to the original process was the removal of the ethanol-washing step after immersion in the polymer solutions, since ethanol is not compatible with the resists used in selected-area nucleation. Investigations into the substrate used for CVD, the replacement of the two polymers with a single silane and the properties of the nanodiamond in water solution used were undertaken, in order to try to optimise the uniformity and nucleation density achieved through use of this self-assembly approach.

#### 9.1.1 The solutions

The PDDA ( $M_w < 100,000$ ) and PSS ( $M_w \approx 70,000$ ) used throughout this investigation were purchased from Sigma-Aldrich. An aqueous solution of PDDA dispersed in deionised water was made up with a concentration of 10 w/v %. The solution was then mixed to ensure even polymer dispersion using a Bandelin sonoPLUS HD2070 MS72 ultrasonic mixer for 10 min at 30 % power. A 10 w/v % aqueous solution of PSS in deionised water was made up and heated until it was completely dissolved prior to addition of 5 g of the nanodiamond solution. This solution was then sonicated for 10 min at 30 % power. The nanodiamond particle solution used was a 50 w/v % aqueous colloid dispersion in water and was obtained from the Carbon Research Institute, Tokida.

Two other nanocluster diamond particle solutions, with average particle sizes of 30 nm, were investigated and were obtained from Microdiamant in Switzerland. Experiments were also carried out with a 0.5 % w/w de-agglomerated nanodiamond suspension in

dimethylsulfoxide (DMSO) with a particle size of 3-7 nm, obtained from the University of Gdansk, Poland.

The size distribution of the nanodiamond particles in the different dispersions investigated was characterised using a dynamic light scattering (DLS) method with a Nano-S90 instrument from Malvern Instruments. The measurements were carried out at 25 °C with an equilibration time of 120 s and a scattering angle of 90°.

For the silane tests, carboxyethylsilanetriol sodium salt in water (CEST) and tetraethoxysilane (TEOS) were obtained from Gelest. The CEST solution was used either in the sourced concentration or diluted by half with deionised water and mixed by ultrasonic agitation for 5 min at 30 % power. The TEOS solution was added to a 1 mol dm<sup>-3</sup> aqueous solution of sodium hydroxide and stirred for 5 min with a magnetic stirrer in order to hydrolyse it. Three aqueous nanodiamond (ND) dispersions in deionised (DI) water, for use in the silane investigations, were made up at concentrations of 10 w/v %, 5 w/v % and 2.5 w/v % and sonicated for 10 min at 30 % power.

## **9.2 MWCVD reactor**

The seeded samples were grown on in an Astex-type 2.45 GHz MWCVD reactor to deposit a diamond film for subsequent analysis of its uniformity and density. A complete description of the components of the reactor and the standard operating procedure is given in the PhD thesis by O. Fox<sup>4</sup> and is summarised below.

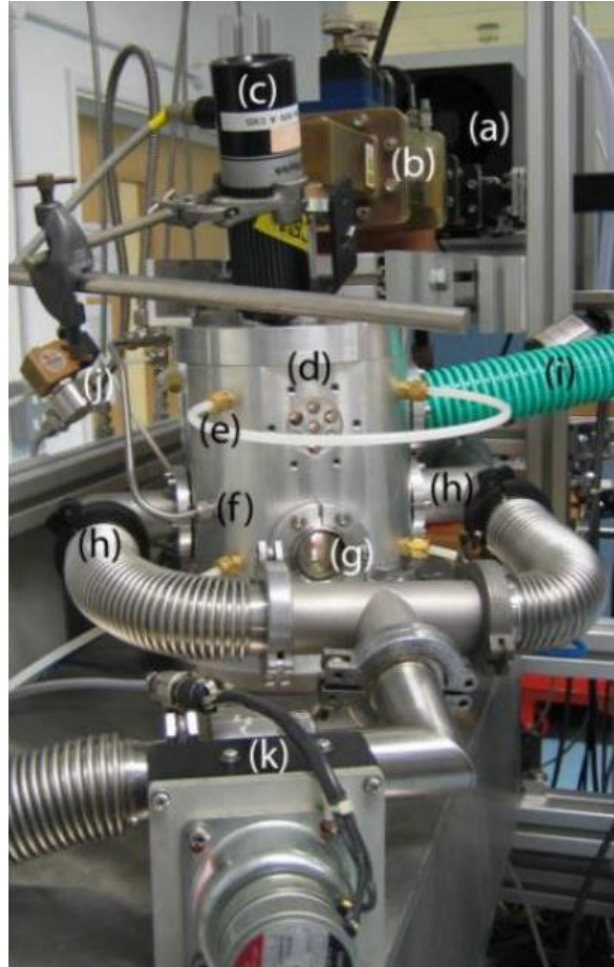


**Figure 23:** The MWCVD reactor used for synthetic diamond growth (a) MW magnetron (b) MW waveguide (c) optical pyrometer (d) reaction chamber (e) water-cooler (f) process gas inlet (g) silica viewing window (h) gas exhaust (i) air-cooler pipe (j) solenoid valve (k) pressure regulating butterfly valve. Image reproduced from reference 4.

The seeded substrate was placed on a circular molybdenum holder that sits on a tungsten wire ring in the centre of the reaction chamber. The holder and substrate are heated to a temperature of around 1000 K by the plasma and the tungsten wire is required to act as a thermal break between them and the water-cooled aluminium base of the reaction chamber. The chamber was then closed, secured with bolts and fastened to the gas exhaust (h) with clamps before being vacuated by the opening of the butterfly valve (k). The water, air-cooler and temperature measurement pyrometer were then turned on and the required gases fed into the reaction chamber just below the quartz window, the flow rates and

mixing ratios of which were controlled by a MKS247C electronic control box connected to six mass-flow controllers (MFC).

2.45 GHz microwave radiation generated by a 1.5 kW HS-1000 magnetron activated the process gases and a plasma was formed. The plasma contains activated carbon radicals that diffuse to the substrate surface and add to the seeded nanodiamond layer, producing a polycrystalline diamond film. The required power and pressure for the particular deposition were then set (the temperature cannot be controlled independently). Throughout this project, the conditions typically involved a chamber pressure of  $p = 125$  Torr and an input power of  $P = 1000$  W for a microcrystalline diamond (MCD) deposition,  $p = 110$  Torr and  $P = 1000$  W for a nanocrystalline diamond (NCD) deposition and  $p = 170$  Torr and  $P = 800$  W for an ultrananocrystalline diamond (UNCD) deposition. The standard gas mixture used varied between different deposition types. A typical MCD deposition involved a gas mixture of 500 sccm H<sub>2</sub>, 25 sccm CH<sub>4</sub> and 40 sccm Ar, where 'sccm' refers to gas flow in units of standard centimetres cubed per minute. The gas mixture used in NCD deposition was 500 sccm H<sub>2</sub>, 35 sccm CH<sub>4</sub> and 4 sccm N<sub>2</sub> and a mixture of 50 sccm H<sub>2</sub>, 3 sccm CH<sub>4</sub> and 450 sccm Ar in UNCD deposition. See **Appendix 14.1** for a complete list of all depositions carried out in this project and the conditions used.

### 9.3 Optical and scanning electron microscopy and Raman spectroscopy

After deposition in the microwave reactor, the samples were viewed with a Zeiss Axiolab optical microscope to assess the uniformity of the grown film and hence the effectiveness of the seeding method used. Images were taken at magnifications of  $\times 5$ ,  $\times 10$ ,  $\times 20$ ,  $\times 50$  or  $\times 100$ . A JEOL JSM 6330F scanning electron microscope (SEM), which produces an electron beam via field emission, was also used to look at the films in greater detail. A beam of electrons passes over the surface of the sample and images with very high resolution (on the nanometer scale) can be obtained by detecting the secondary electrons emitted by the surface. As a result, the morphology of the diamond crystals and the thickness of freestanding films could be analysed. Cross-sections of lens substrates that had been grown on were prepared by cleaving them using an Oxford Lasers Alpha 532 laser machining instrument and imaged to determine the thickness of the diamond layer.

Characterisation of some of the diamond films was achieved using a UV-laser Raman spectrometer from Renishaw. The UV laser (325 nm wavelength) at 100 % intensity was used for each film with 30 accumulations per sample and an accumulation time of 25 s.

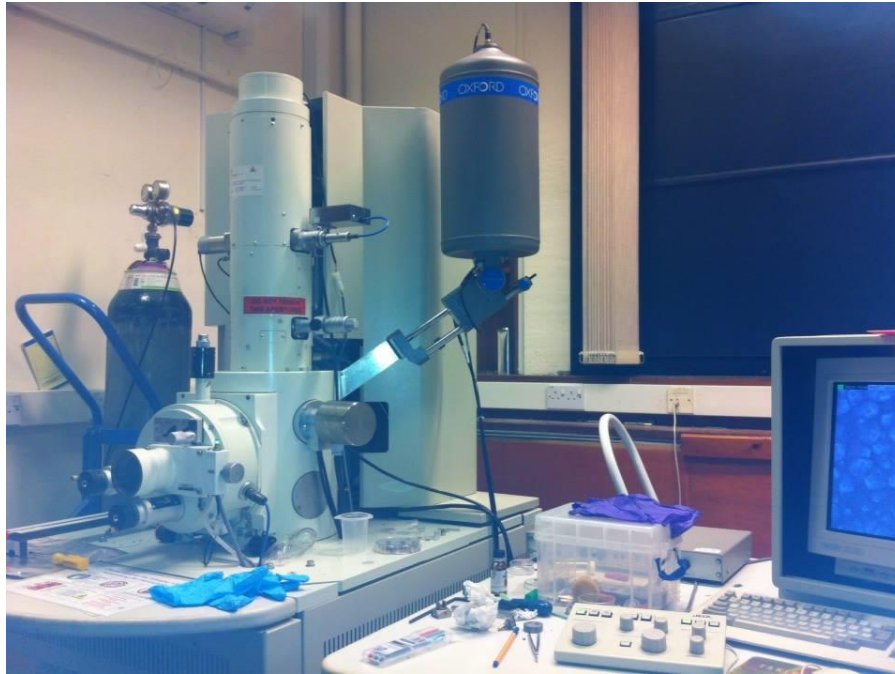


**Figure 24:** Photograph of the scanning electron microscope used throughout the project (JEOL JSM 6330F).

#### **9.4 Mass flow controller (MFC) calibration**

Before the experimental work was commenced, the MFCs for each gas used in MWCVD were calibrated. This was to ensure that the amount of gas that was flowing into the reactor was the amount that had been set on the controller. There are five MFCs that were calibrated; hydrogen, methane, nitrogen, argon and nitrogen(argon). The nitrogen(argon) MFC is used to flow small amounts of argon into the reaction chamber (up to 200 sccm) whereas the argon MFC is used when larger flow rates than 200 sccm are required. The nitrogen(argon) MFC is calibrated for nitrogen so a conversion factor must be applied whereby, in a standard MCD deposition where 40 sccm of argon were used, the MFC had to be set to 27 sccm.

The calibration involved flowing each gas into the reaction chamber once it had completely pumped down to vacuum and the exhaust valve had been closed, then the time it took to

reach a certain pressure was measured. This was done for four flow rates for each gas, at 0.25, 0.5, 0.75 and 1.0 times the maximum flow rate of the MFC.

From the linear behaviour seen in the graphs plotted for each MFC (**Appendix 14.2**), it is evident that each MFC is working in the way that it should. To check that the flow rate of each gas varies with the rate of the pressure rise in the same way, a graph with these values was plotted for all five MFCs. It was found that the gradient of the line for each MFC is exactly the same and so all points lie on the same line (**Fig.25**). In conclusion, all MFCs proved to be correctly calibrated.

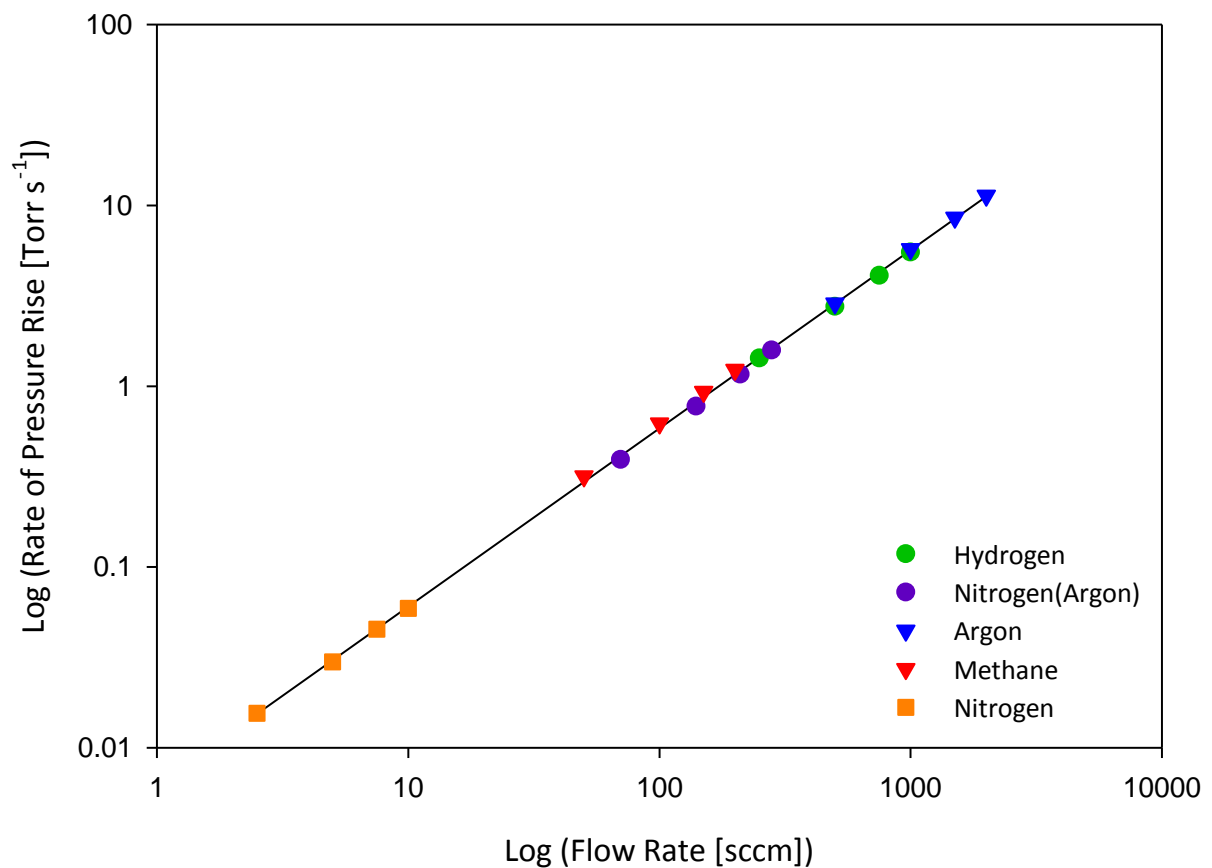


**Figure 25:** Graph showing flow rate against the rate of pressure rise for each MFC.

## **10 Results and Discussion**

The aim of this project was to optimise the selected-area, self-assembly nucleation process, so that it was both repeatable and compatible with resist-coated substrates, without compromising a high nucleation density and uniformity. In order to do this, the starting point was to use the best practice method for electrostatic self-assembly, recommended in a thesis by E. Tofts.<sup>60</sup> Investigations into the solvents used in the cleaning and washing steps, the way that the polymers are applied to the substrate and the nanodiamond solution used were then undertaken and experiments using a silane molecule instead of the two polymers were carried out. In addition, both the removal of different resist layers and the use of a buffered oxide etch were investigated in an attempt to achieve selected-area diamond deposition. After seeding, the samples were all deposited on in the microwave reactor before being analysed by microscopy. Throughout the project various different substrates, other than silicon, were also seeded and grown on, in order to see the effectiveness of diamond growth on materials that had not previously been employed. The gas mixture used in the microwave reactor when growing diamond films on a series of 1 cm<sup>2</sup> silicon substrates was also varied, in order to analyse the effect of the concentration of both nitrogen and argon on diamond morphology and grain size. Experiments were not necessarily carried out in the order in which they will be discussed here.

### **10.1 Development of a resist-compatible and repeatable, electrostatic self-assembly nanodiamond nucleation**

#### **10.1.1 Alterations to the cleaning and drying steps**

Since the aim of this project was to apply the self-assembly process to lens-mould substrates and achieve selected-area deposition, the method used had to be compatible with resist-coated substrates. The method suggested in the thesis by E. Tofts<sup>60</sup> recommends that the substrate to be nucleated is cleaned sequentially in four solvents to remove contaminants and maximise the electrostatic interaction between the substrate and the cationic polymer to be applied in the next step. Rinsing in DI water, acetone, ethanol and methanol, accompanied by drying with pressurised air in between each rinse, was a time consuming process so the methanol rinse was removed to see if there was a noticeable

difference in the quality of the diamond film that resulted after MWCVD. To achieve compatibility of this nucleation method with resist-coated substrates, ethanol, which will attack the ma-N2410 resist layer coating the top surface of a substrate, was taken out of the washing steps that follow immersion in each polymer solution. This was essential since, in a selected-area, self-assembly nucleation process, the resist layer cannot be removed from the substrate until after it has been nucleated, as described in **Section 7.2**.

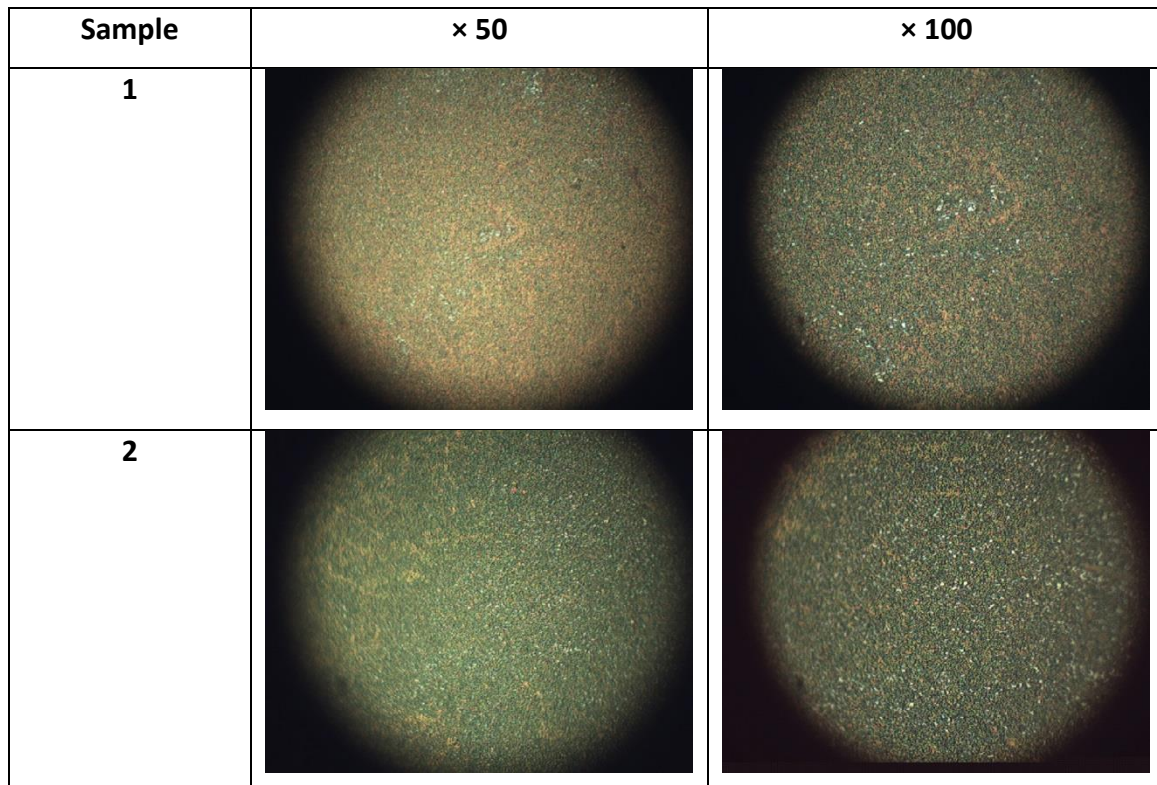


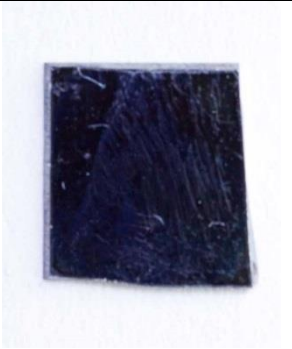
**Figure 26:** Optical microscope images comparing diamond films on silicon substrates after one hour MWCVD. The first sample was washed in DI water, acetone, ethanol and methanol and washed with DI water and ethanol after immersion in each polymer. Sample 2 was cleaned with DI water, acetone and ethanol and washed in DI water only.

As seen from the images above, there is little difference in the uniformity of the diamond films achieved with different washing processes. Therefore, a standard process was adopted for silicon substrates that was both repeatable and resist compatible, involving no methanol rinse during the cleaning step and washing of the substrate in just DI water after each polymer immersion. Resist-coated substrates are only cleaned with DI water before nucleation.

### 10.1.2 Investigation into the ionic polymer coating method

A second variable in the standard self-assembly nucleation using PDDA and PSS solutions investigated, was the way in which the polymer layers are applied to the substrate. To do this, spin-coating was used to apply PDDA solution to nine clean silicon substrates to determine if this would affect the quality of the diamond film obtained after microwave chemical vapour deposition. A Pasteur pipette was used to apply just enough of the polymer solution to the substrate surface to cover it completely (40  $\mu$ l). The substrate, held in place in the Laurell spin-coater by a vacuum, was then spun very rapidly to produce a thin layer across the surface, while removing the need for washing and drying after the polymer has been applied. This minimises any drying patterns that may arise from using compressed-air drying. The spin rate and acceleration were varied between experiments to try to achieve the most uniform polymer layer possible. A full description of the conditions used to coat each sample, together with a photograph of each taken after the spin-coating, is given in **Appendix 14.3**.

None of the samples looked particularly uniform after the spin-coating, although the best two samples (samples 2 and 3) were taken and immersed in the PSS-ND solution for 1 h as normal, before a 15 min MCD deposition was carried out on each.

	After spin-coating with PDDA	After immersion in PSS-ND (1 h)	After 15 min MCD
<b>Sample2</b> <b>Spin rate: 5000 rpm</b> <b>Acceleration: 500 rpm s<sup>-1</sup></b> <b>Spin time: 1 min</b>			

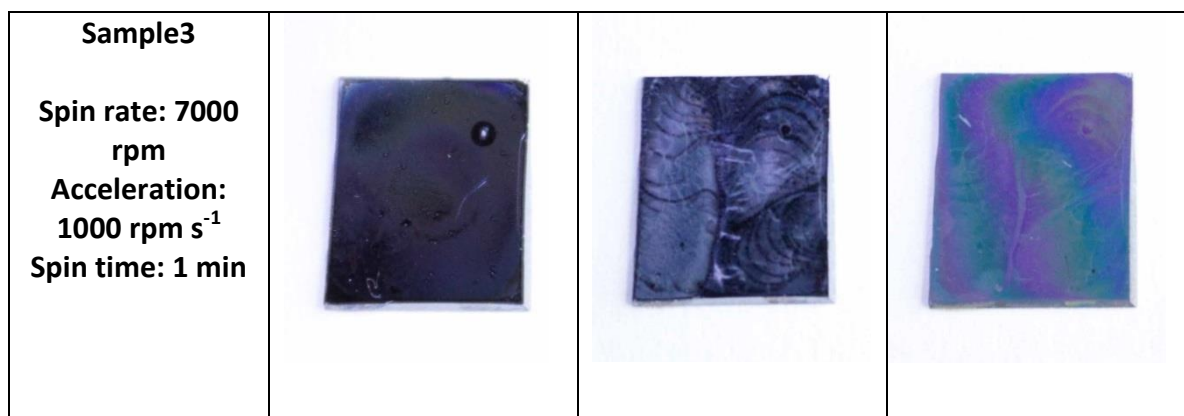


**Figure 27:** Photographs of samples 2 and 3 after each step in the seeding process.

It can easily be seen in the photography, where various patterns and colours are visible on the samples, that spin-coating does not lead to an evenly distributed polymer layer on the substrate surface. Furthermore, these patterns remain visible after diamond growth, making the procedure unsuitable for use in self-assembly nucleation. It was concluded that substrate immersion in the polymer solutions is the method that would be adhered to.

## 10.2 Investigating the use of a silane molecule to replace PDDA and PSS

In order to optimise the self-assembly process further, replacement of the PDDA and PSS polymers with a silane molecule was investigated. First reported in the 1940s by Zisman, there has been much research into self-assembled monolayers of silanes on a variety of substrates.<sup>64</sup> Kessel *et. al* report that monolayer self-assembly is an excellent method for producing highly ordered, well characterised monolayers on various substrates<sup>65</sup> and Haensch *et al.* found that silicon is a particularly good substrate, forming monolayers that are both physically and chemically very stable.<sup>66</sup>

Silanes spontaneously form monolayers on silicon due to favourable interactions between both the individual silane molecules and the silane with the substrate surface.<sup>67</sup> There are three main components of a silane molecule; the head group, the spacer and the terminal functional group.<sup>68</sup> The formation of a strong siloxane (Si – O) bond between the silanol head group and the substrate surface provides the driving force for the reaction. Additional stability arises in the monolayer due to the favourable van der Waals' intermolecular interactions between the alkyl spacer groups on neighbouring silane molecules, and tuning of the terminal functional group allows control of the monolayer properties.<sup>67</sup> The decrease in entropy of the system on ordering must be overcome by the gain in energy, as a result of

the thermodynamically favourable interactions, to cause the molecules to align into a densely packed, highly ordered monolayer.<sup>68</sup>

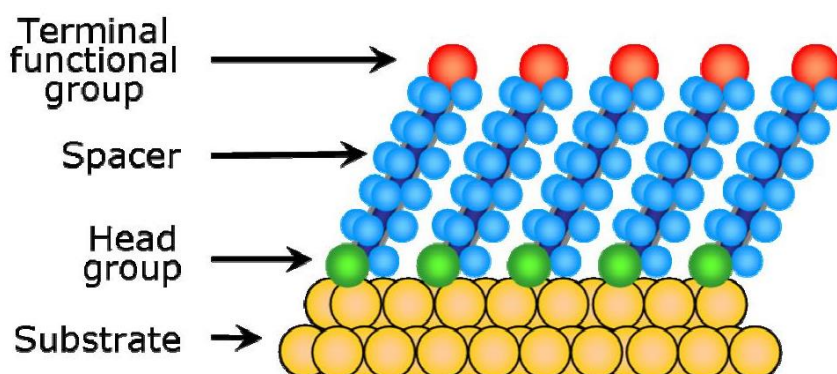


**Figure 28:** Schematic diagram showing an assembled silane monolayer on a substrate and the three key constituents of a silane molecule. Image reproduced from reference 68.

Since nanodiamond particles are positively charged at the surface, a silane molecule with an existing anionic functional group, or one that can be pre-treated to make it anionic, is needed. For this reason tetraethoxysilane (TEOS) was tested first.

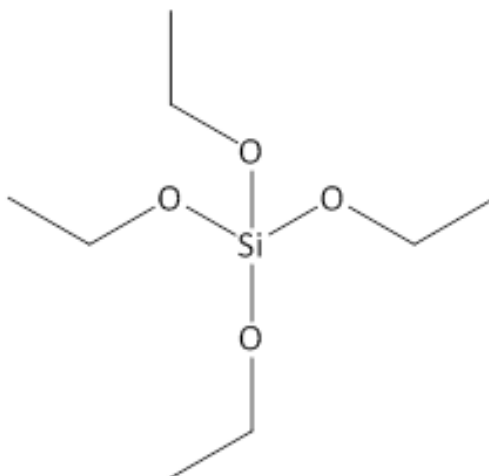


**Figure 29:** Schematic drawing showing the structure of TEOS.

The ester functional groups in this molecule needed pre-hydrolysing before TEOS could be used in the seeding process. The purpose of this was to cleave the ester groups, leaving the negatively charged oxygen that is able to interact with both the silicon substrate and the nanodiamond particles later in the process. To do this, a base-catalysed hydrolysis was carried out using sodium hydroxide. Aqueous NaOH with a concentration of  $1 \text{ mol dm}^{-3}$  was

added to the TEOS solution and stirred until monophasic. Jalali describes the formation of silane monolayers on silicon after immersion of the clean substrate in the silane solution<sup>68</sup> and Banga *et al.* found that the monolayer forms after an immersion time of just 5 min.<sup>69</sup> Therefore, after two 1 cm<sup>2</sup> silicon substrates had been thoroughly cleaned, they were immersed in the hydrolysed silane solution for 5 min, followed by rinsing in DI water and drying with compressed air. The substrates were then submerged in a ND solution with a concentration of 10 w/v % in DI water and rinsed and dried again. A nanocrystalline diamond deposition was then carried out on each substrate; the first for 5 min and the second for 30 min. As a control experiment, a silicon substrate, which had been cleaned but not immersed in the silane solution, was also submerged in the ND solution and then grown on for 5 min under nanocrystalline diamond conditions.

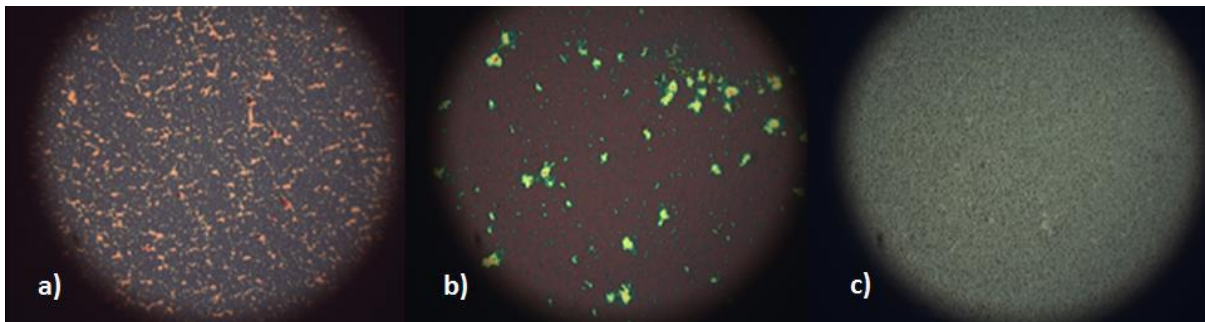


**Figure 30:** Optical microscope images (magnification  $\times 100$ ) of the diamond films grown on a) a silane seeded substrate after a 5 min NCD b) a silicon control substrate after a 5 min NCD and c) a silane seeded substrate after a 30 min NCD.

These images show that the silane molecule is effective in nucleating the substrate with nanodiamond particles. The diamond layer after the 30 min NCD looks more uniform than the 5 min NCD, but after such a short deposition time this layer is not yet continuous and so small patches of silicon can still be seen. It can also be seen that the films grown on the silane seeded substrates are more uniform than that on the control substrate, suggesting that the silane molecule is useful in aiding uniformity.

After these promising results, experiments were conducted with a different silane molecule. Carboxyethylsilanetriol (CEST) was chosen as it contains an existing anionic functional group and hence renders the pre-hydrolysis step unnecessary.

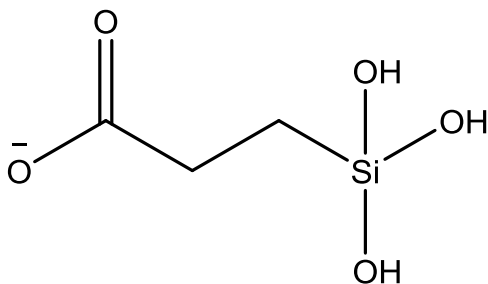


**Figure 31:** Schematic drawing showing the structure of CEST.

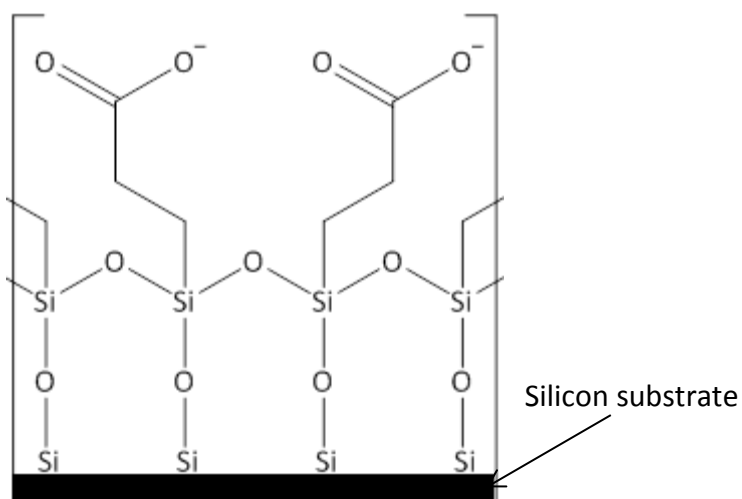


**Figure 32:** Schematic drawing of the CEST on silicon monolayer.

To trial the effectiveness of CEST in the seeding process, two silicon substrates were first seeded using the same cleaning and washing conditions as were used with TEOS and also the same 10 w/v % in DI water, ND solution. The only difference was 5 min immersion in CEST, rather than in TEOS. A 5 min NCD was then done on the first sample and a 2.5 min NCD on the second.

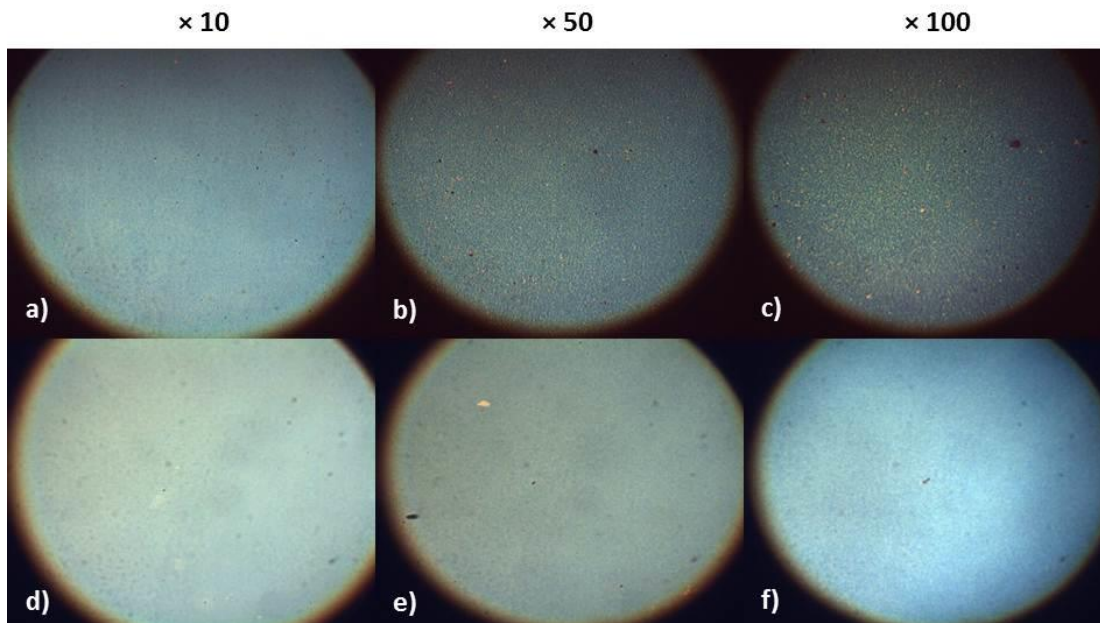


**Figure 33:** Optical microscope images, at different magnifications, of the first two diamond films grown on CEST-seeded substrates. Images a), b) and c) are after a 5 min NCD deposition, whereas d), e) and f) are after a 2.5 min NCD deposition.

From **Fig.33**, it is evident that very uniform films were achieved by employing CEST to form a seed layer of nanodiamond on silicon. The diamond layers grown after independent 5 min NCD depositions on three silicon substrates that had been seeded differently were then compared. To do this, the first sample was seeded with PDPA and PSS-ND, the second with TEOS/ND and the third with CEST/ND.

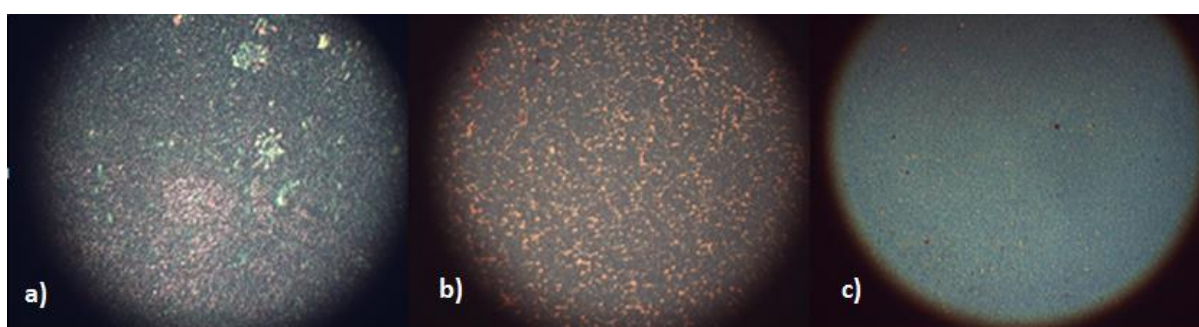


**Figure 34:** Optical microscope images (magnification  $\times 100$ ) comparing the diamond films grown after 5 min NCD deposition on Si substrates seeded with ND and a) PDPA and PSS b) TEOS and c) CEST.

This image shows that using CEST in the seeding procedure yields the most uniform diamond film. There are fewer patches of exposed silicon and the layer is already

continuous after a 5 min deposition. Therefore, in order to devise a best practice self-assembly nucleation with the use of CEST, experiments with various concentrations of both the CEST solution and the ND in DI water solution were carried out. In each experiment only one parameter was changed, whilst keeping all other variables constant. At first the concentration of CEST was changed, trying it again without dilution and then diluted by 50 % in DI water. These samples were then both immersed in the ND solution of 10 w/v % in DI water. ND in DI water concentrations of 5 w/v % and 2.5 w/v %, on samples seeded with the undiluted CEST solution, were then investigated. A final sample was seeded with a pre-mixed solution of non-diluted CEST and 10 w/v % nanodiamond in DI water solution. All samples were grown on in the microwave reactor for 2.5 min. The sample seeded in the same way as the trial substrates (undiluted CEST and 10 w/v % ND in DI water) was grown on in the absence of nitrogen (500 sccm H<sub>2</sub> and 35 sccm CH<sub>4</sub>) to try to achieve a non-continuous film (as the lack of nitrogen will reduce the growth rate) and enable calculation of nucleation density. The other four samples were grown on under normal nanocrystalline diamond deposition conditions. A full comparison of the samples at three different magnifications is given in **Appendix 14.4**.

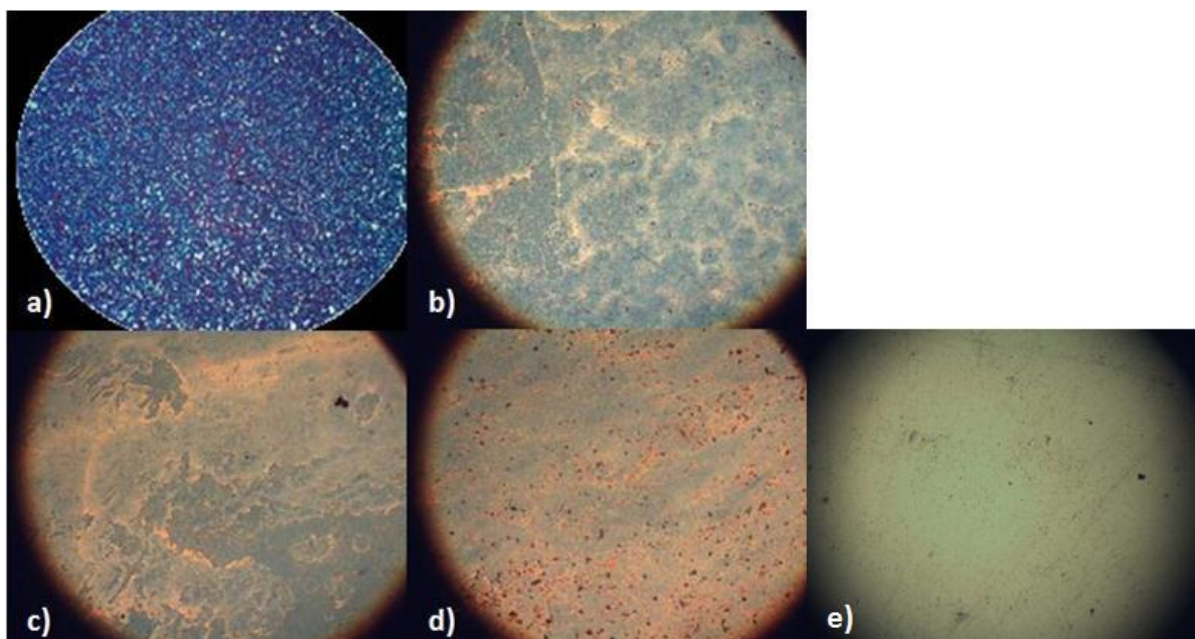


**Figure 35:** Comparison of the effect of solution concentration on the nucleation density and uniformity of the diamond films a) undiluted CEST and 10 w/v % ND in DI water b) undiluted CEST and 5 w/v % ND in DI water c) undiluted CEST and 2.5 w/v % ND in DI water d) 50 w/v % CEST in DI water and 10 w/v % ND in DI water and e) pre-mixed undiluted CEST and 10 w/v % ND in DI water. All imaged with optical microscopy (magnification  $\times 5$ ).

Comparing the five samples in **Fig.35**, it appears that a) is the most dense, uniform layer. This was not surprising since it would be predicted that the most concentrated CEST solution would give a more coherent coverage of the substrate, increasing uniformity, and the most concentrated ND solution the most nucleation sites, increasing density. The white area seen in e) is all silicon, with the only diamond present being the sparse black spots. Therefore, it was concluded that using pre-mixed silane and ND in DI water is the least effective method.

Scanning electron microscopy (complete results shown in **Appendix 14.5**) was then used to confirm that using undiluted CEST and a 10 w/v % ND in DI water solution produces the best diamond film.

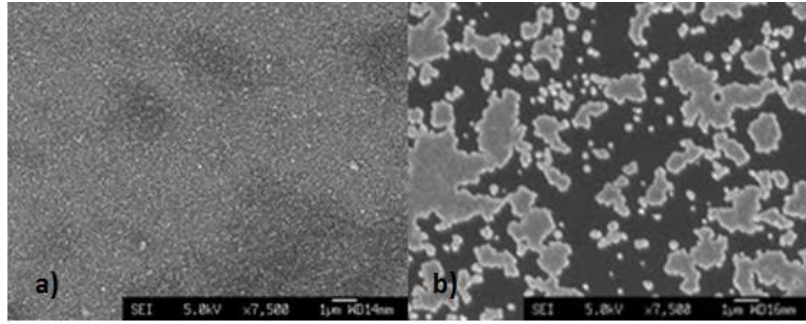


**Figure 36:** SEM images (magnification  $\times 7500$ ) showing the diamond films after a) 2.5 min MCD deposition on Si seeded with undiluted CEST and ND in DI water (10 w/v %) and b) a 2.5 min NCD deposition on Si seeded with CEST diluted by 50 % with DI water and ND in DI water (10 w/v %).

It is clear from looking at **Fig.36** that using CEST diluted with DI water decreases the nucleation density and consequently prevents a continuous layer growing after 2.5 min. Furthermore, it is noticeable that the films generally looked patchy when viewed with the SEM. This is likely to be due to ineffective washing of any unbound silane from the surface before immersion in the ND solution. For this reason, CEST seeding procedures carried out after this were washed in water for longer to ensure all unbound silane was removed, leaving a uniform monolayer coverage of the substrate surface.

At this point a recommended procedure for self-assembly using CEST could be suggested. This involves, after solvent cleaning, the substrate being immersed in the undiluted CEST solution for 5 min. It is then thoroughly washed in DI water and dried in air, followed by immersion in a ND solution of 10 w/v % in DI water. A final wash in DI water and dry in air then completes the process.

**Fig.36(a)** also shows that a continuous diamond film has already grown after just 2.5 min, even in the absence of nitrogen. Following this, two more Si substrates were seeded with undiluted CEST and 10 w/v % ND in DI water and grown on, each for 2.5 min in the absence of nitrogen and also reduced methane flow, to try and achieve a non-continuous diamond layer. The first gas mixture used was 500 sccm  $H_2$  and 25 sccm  $CH_4$  and the second was 500 sccm  $H_2$  and 15 sccm  $CH_4$  and SEM images were taken of the resulting films.

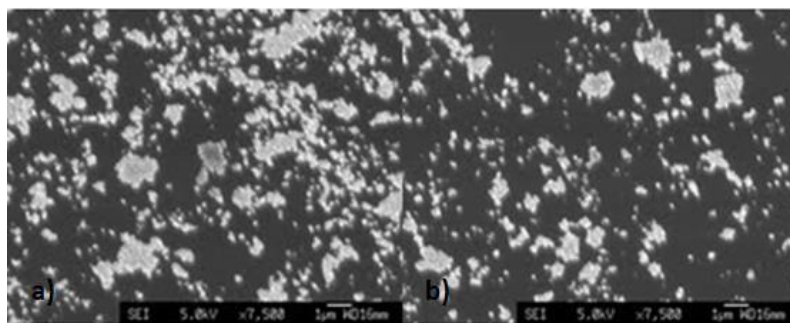


**Figure 37:** SEM images (magnification  $\times 7500$ ) of the diamond grown in a) 25 sccm  $\text{CH}_4$  and b) 15 sccm  $\text{CH}_4$ .

Whilst both films grown were non-continuous, the individual diamond grains have already begun to coalesce. For an accurate calculation of nucleation density, the individual diamond crystals are required so a calculation of nucleation density was still not possible. As expected, a smaller degree of coalescence is seen in b) since the gas mixture contained less methane.

To ensure repeatability of the CEST standard method, a further two silicon samples were seeded and longer depositions of one hour conducted on each; one under nanocrystalline diamond conditions, the other under microcrystalline diamond conditions.

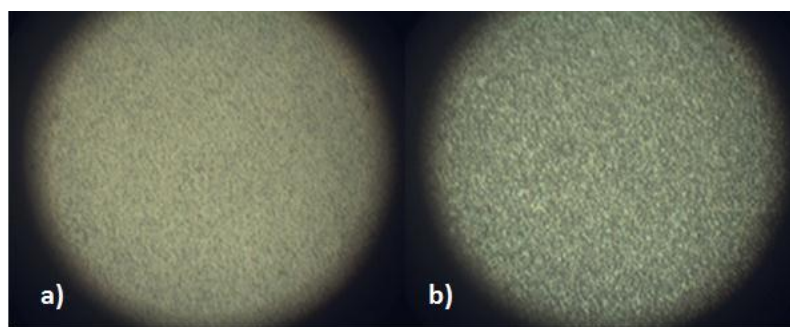


**Figure 38:** Optical microscope images (magnification  $\times 100$ ) of a) a NCD film and b) a MCD film after a deposition time of one hour.

The absence of any patches in these images confirms the effectiveness of self-assembly nucleation with CEST.

This novel seeding method has several advantages over the conventional PDDA/PSS-ND electrostatic self-assembly nucleation. The covalent bond between the substrate and the silane head group is very strong and prevents the monolayer being washed off or disrupted

during the washing and drying steps. In addition, the much smaller CEST molecule, with a molecular mass of  $137 \text{ g mol}^{-1}$  compared with  $\approx 70,000 \text{ g mol}^{-1}$  and  $<100,000 \text{ g mol}^{-1}$  for PSS and PDDA, respectively, gives a much denser seed layer. The whole seeding process is also more efficient, since the functionality at both ends of the CEST molecule enables replacement of two polymers with just one silane and the time the substrate must spend immersed in solution is reduced from 70 min to just 15 min.

### **10.3 The use of different substrates in chemical vapour deposition**

Once standard self-assembly procedures using either PDDA/PSS-ND or CEST/ND had been developed, they were applied to a number of different substrates to see if uniform diamond layers would grow as well as they do on silicon. If a layer of CVD diamond can be deposited on a particular substrate, then the material will have the desirable properties, such as hardness, chemical inertness and stress resistance, of diamond, without the expense of being made entirely from it. All thermal expansion coefficients given were reported in the CRC Handbook of Chemistry and Physics.<sup>70</sup>

#### **10.3.1 Diamond on titanium**

Experiments were first conducted with six titanium discs. After seeding the samples using PDDA and PSS-ND, each one was grown on for 1 hour in the microwave reactor under microcrystalline diamond conditions.

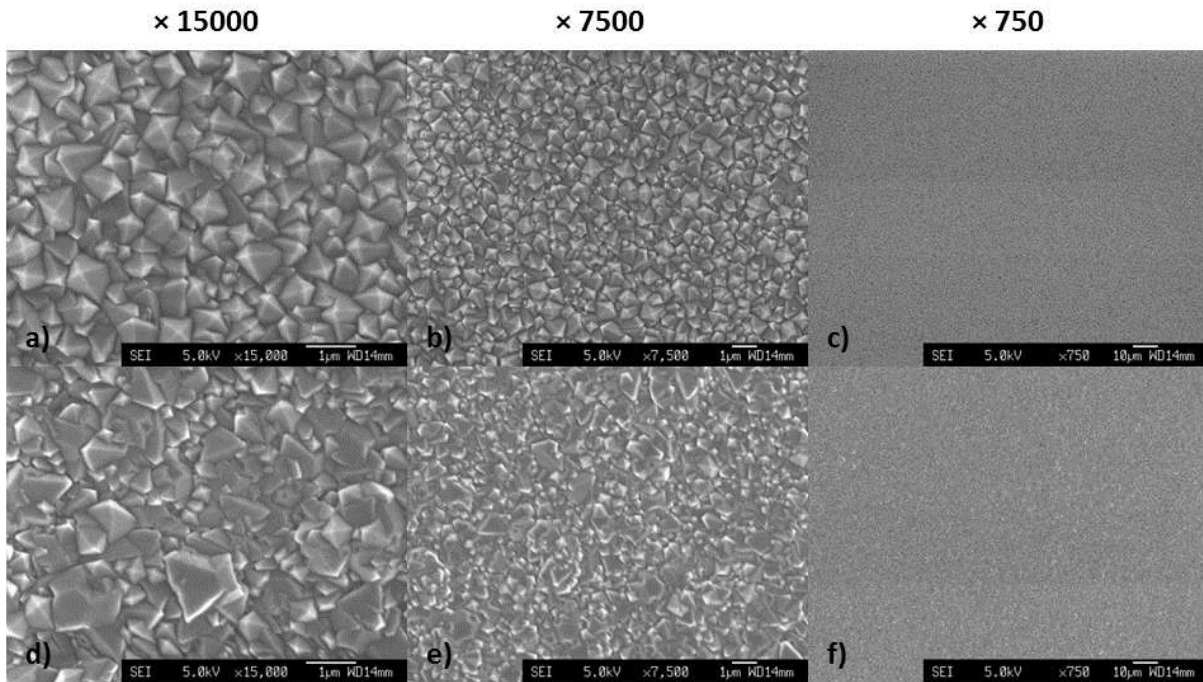


**Figure 39:** SEM images, after diamond deposition, comparing two of the titanium samples at three different magnifications. Images a), b) and c) show a microcrystalline diamond film, grown at  $P = 850$  W and  $p = 110$  Torr, and images d), e) and f) a microcrystalline diamond film grown at  $P = 800$  W and  $p = 80$  Torr.

The noticeable difference between the two films is the morphology of the diamond crystals, which has been induced by the variation in power density and consequent difference in substrate temperature. The first film has the predominantly  $\langle 111 \rangle$  oriented surface, whereas the second film contains other crystal planes. It is also clear that the diamond coverage of the substrate surface of both samples is very even and therefore the seeding method works very well with titanium discs. For this reason, seeding thick titanium squares was then investigated.

Before each deposition, the square titanium substrate was seeded according to the standard procedure using PDDA and PSS-ND. Since these squares were 5 mm thick, they were placed in a recessed molybdenum holder in the microwave reactor to lower the surface temperature during the deposition. The first sample was grown on under standard microcrystalline diamond conditions for 1 h but the film delaminated from the metal during switch off of the plasma. Titanium has a thermal expansion coefficient of  $8.6 \times 10^{-6} \text{ K}^{-1}$ , whereas that of diamond is  $1.0 \times 10^{-6} \text{ K}^{-1}$ . This mismatch causes the diamond film to delaminate from the substrate as it cools. In the first Ti substrate test the diamond film

broke up because of the thermal shock on cooling as the plasma was extinguished. The power and pressure of the next deposition were lowered to 800 W and 75 Torr, respectively, in an attempt to lower the Ti substrate temperature and the thermal shock. The titanium substrate did reach a lower surface temperature of 800 °C, but this was still too high for the film to survive on cooling. For the next deposition, the power and pressure remained at 800 W and 75 Torr, but 50 sccm of CH<sub>4</sub> were flowed into the reaction chamber for the first 15 min of the deposition, before the flow rate was turned back down to the usual 25 sccm for the remaining 45 min. The purpose of a higher methane concentration at the beginning was to form a metal carbide layer, providing a strong interfacial layer to bond the diamond and the metal. Despite this, the film still broke up at the point of plasma switch off. The fourth deposition involved the usual MCD gas mixture and lower power and pressure decided on after the first deposition. At the end of the deposition, the gas mixture was varied and the plasma slowly switched off, in an attempt to cool the titanium more slowly. Over the final 5 min of the deposition the flow rate of CH<sub>4</sub> was reduced from 25 sccm to 5 sccm, before being switched off completely. A decrease in the flow rate of H<sub>2</sub> from 500 sccm to 100 sccm, in increments of 100 sccm per min, whilst increasing that of Ar from 40 sccm to 100 sccm then to 400 sccm, also in increments of 100 sccm per min, was employed. Then, at 59 min into the deposition, the flow rate of H<sub>2</sub> was decreased by 50 sccm to 50 sccm and that of Ar increased to 450 sccm. Increasing the content of argon increases the size of the plasma and, as a result, the heat is dissipated from the substrate more effectively. The hydrogen content was going to be reduced simultaneously so that the total gas flow remained the same. However, this method did not succeed as the plasma became unstable once the methane had been completely switched off and had to be quickly turned off, causing the film again to delaminate. As a final trial a UNCD deposition was carried out for 1 h but, despite using a slow plasma switch off, this film also broke up. It was concluded that microwave chemical vapour deposition of diamond is not compatible with these thick titanium substrates.

### **10.3.2 Diamond on zirconium**

The growth of microcrystalline diamond on two square zirconium samples was also investigated. Before a standard MCD deposition could be carried out on the samples, they first needed to be exposed to an argon-rich plasma (50 sccm H<sub>2</sub> and 450 sccm Ar), in order

to etch away the surface oxide layer. On the first sample, a power of 700 W was used with a pressure of 200 Torr. However, the metal substrate got too hot, bending 33 min into the 60 min treatment, and the reactor had to be prematurely switched off. An MCD deposition step could not be carried out on this sample as the substrates used for diamond deposition in the microwave reactor should be flat. A second etch was carried out at a lower power of 600 W and a pressure of 170 Torr. This time the sample remained flat but, at the same time, the lower temperature meant the oxide layer was less likely to be removed. An MCD deposition was carried out at a CH<sub>4</sub> flow rate of 40 sccm and power of 900 W to try to maximise diamond growth and keep the temperature of the zirconium substrate down. Even with this change in conditions and a slow plasma switch off, the diamond film delaminated on cooling. At  $5.7 \times 10^{-6} \text{ K}^{-1}$ , zirconium has a higher thermal expansion coefficient than diamond and the result is that the mismatch is too great for growth of CVD diamond on zirconium to be feasible.

### **10.3.3 Diamond on strontium titanate**

Another substrate experimented with was polished strontium titanate (SrTiO<sub>3</sub>). After seeding two samples with PDDA and PSS-ND, a 30 min standard NCD deposition was conducted on one and a 30 min standard MCD deposition on the other. The nanocrystalline film delaminated from the substrate intact but, during the microcrystalline diamond deposition, the substrate got much hotter and the film did not survive the plasma switch off. There is a difference between the thermal expansion coefficients of diamond and SrTiO<sub>3</sub> ( $9.4 \times 10^{-6} \text{ K}^{-1}$ ), but because the strontium titanate substrates were highly polished, it allowed the nanocrystalline diamond film to completely delaminate and give free-standing diamond films with the dimensions of the substrate. Therefore, experiments to enable slower cooling of the substrate during the switching off of the plasma could lead to successful delamination of microcrystalline diamond films.

### **10.3.4 Diamond on aluminium nitride**

Extensive research was carried out into the use of aluminium nitride (AlN) to form free-standing films or membranes. Both seeding procedures (PDDA/PSS-ND and CEST/ND) were applied to highly polished aluminium nitride substrates to discover if they would work as diamond substrates, in the hope of producing thin diamond membranes. A full list of each

AlN deposition carried out, together with the conditions used and seeding process applied, is detailed in **Appendix 14.1**.

It was found that microcrystalline, nanocrystalline and ultrananocrystalline diamond films, grown on 1 cm<sup>2</sup> AlN squares, all readily delaminate to give large 1 cm<sup>2</sup> free-standing diamond films, provided the plasma is switched off slowly at the end of the deposition. This leaves free-standing diamond thin membranes, which have many potential applications, for example in electronics and as optical windows<sup>71</sup>, and reusable substrates.

After establishing that both micro- and nanocrystalline films could repeatedly be grown for 1 h and easily removed from the substrate, experiments with shorter deposition times were carried out to discover the thinnest membrane that could be obtained. Therefore MCD and NCD depositions of 45 min, 30 min, 15 min and 7 min were carried out on substrates seeded with PDDA/PSS-ND. After a 7 min deposition the film is very thin and it was found that, as the film grows over the edges of the substrate, it was sometimes necessary to use laser machining to remove the film from the AlN surface. The films were analysed using SEM and the film widths were determined from the resulting images using a program called Inkscape, which allowed the film width, and growth rate, to be quantified (see **Appendix 14.6** for a complete table of SEM images).

**Table 2:** Film thicknesses of nanocrystalline diamond films, grown on AlN, after different deposition times.

Deposition Time [min]	Film Thickness [nm]
7	83.0700
15	512.3400
30	1006.3000
45	1438.0300
<b>Growth Rate [<math>\mu\text{m h}^{-1}</math>]</b>	<b>1.9350</b>

**Table 3:** Film thicknesses of microcrystalline diamond films, grown on AlN, after different deposition times.

Deposition Time [min]	Film Thickness [nm]
7	231.9700
15	1191.7200
45	1523.4000
<b>Growth Rate [<math>\mu\text{m h}^{-1}</math>]</b>	<b>2.1371</b>

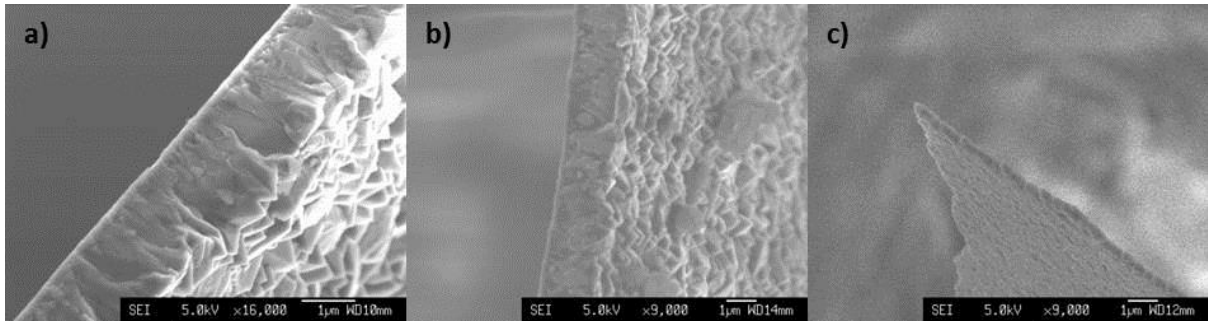


**Figure 40:** SEM images of the cross-sections of the freestanding microcrystalline diamond films after a) 45 min b) 30 min and c) 7 min.

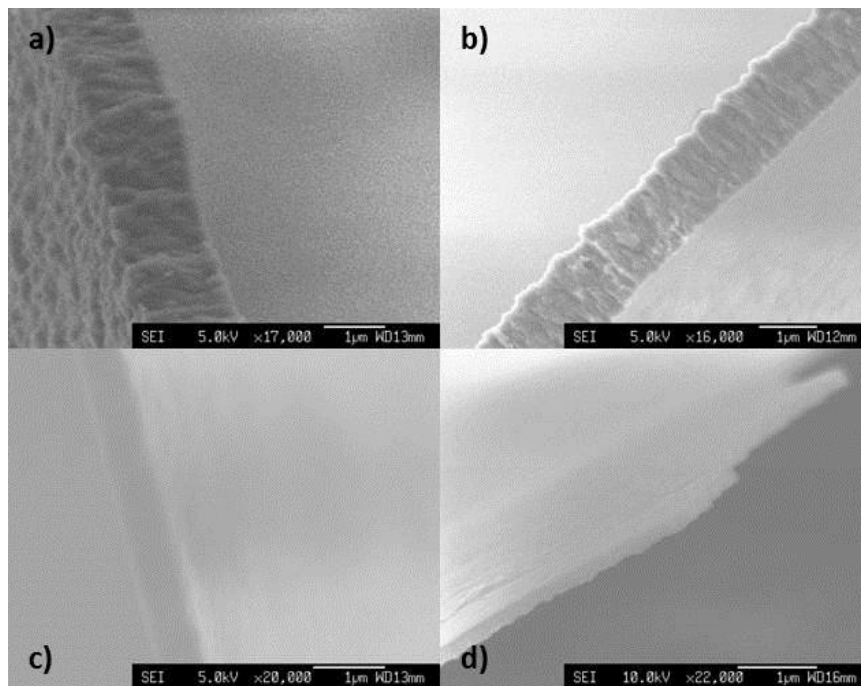


**Figure 41:** SEM images of the cross-sections of the freestanding nanocrystalline diamond films after a) 45 min b) 30 min c) 15 min and d) 7 min.

These images show uniform diamond membranes with decreasing thickness as time decreases. The triangular morphology of the microcrystalline diamond crystals after a 45 min deposition is also apparent.

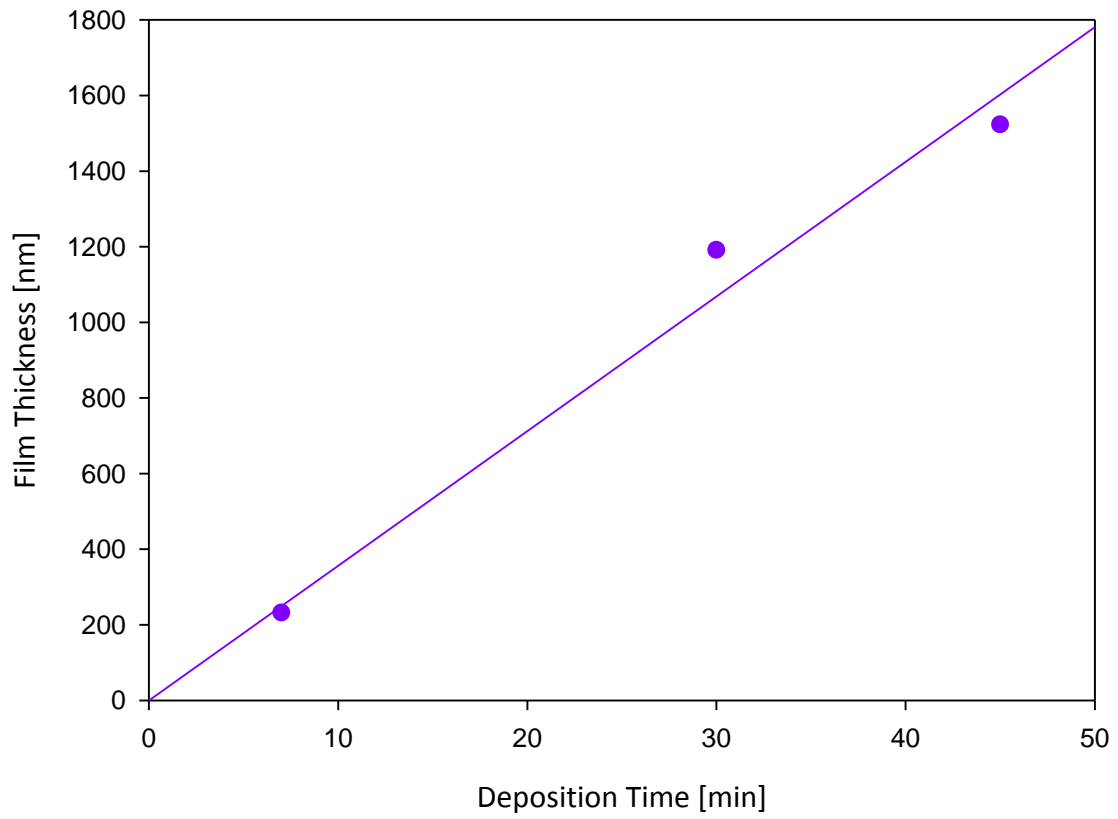


**Figure 42:** Graph showing the growth rate of microcrystalline diamond on AlN.

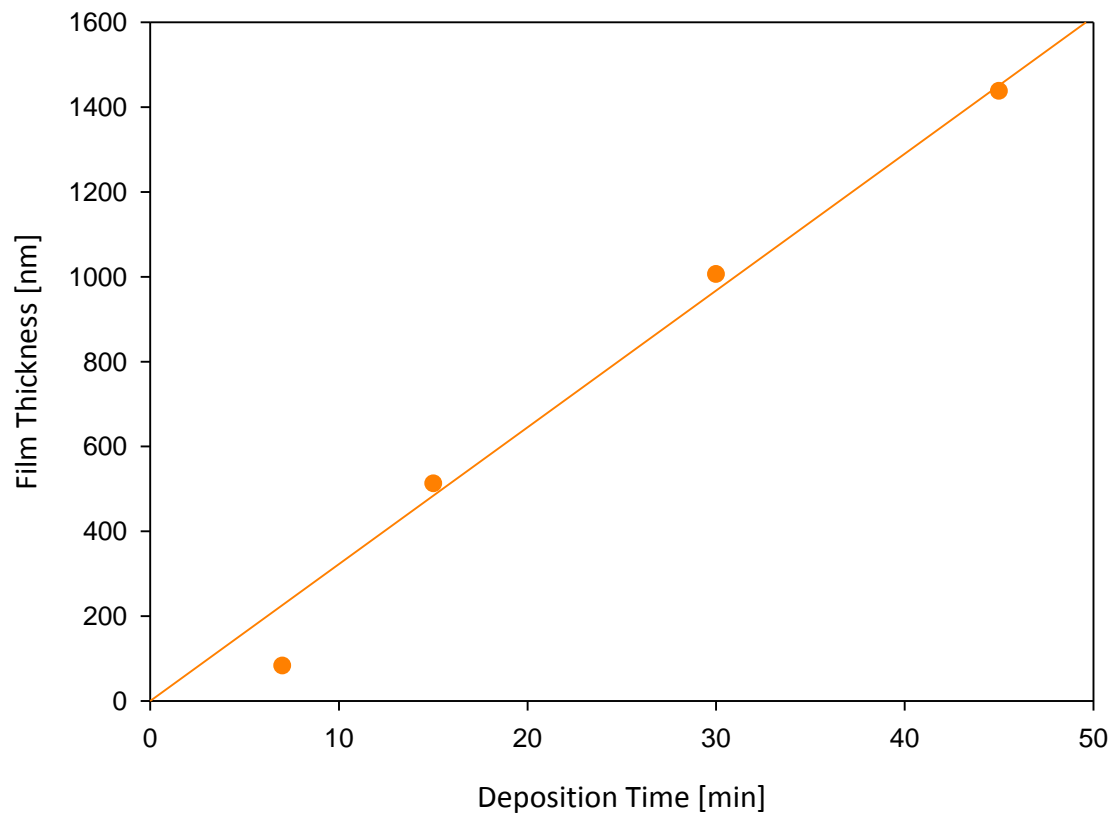


**Figure 43:** Graph showing the growth rate of nanocrystalline diamond on AlN.

The gradients of these graphs yielded growth rates of  $2.14 \mu\text{m h}^{-1}$  for microcrystalline diamond CVD and  $1.94 \mu\text{m h}^{-1}$  for nanocrystalline diamond CVD. The graphs also show that the thickness of the microcrystalline diamond films is greater than the thickness of the nanocrystalline one grown for the same amount of time. It can also be seen that the first data point on the graph in **Fig.42** is lower than predicted by the trendline. Obtaining well-focused SEM images of these thin diamond membranes was sometimes difficult, particularly for the thinnest films, as charging becomes an issue. This is because the sample was not well attached to the metallic stub and the conductivity was compromised. As a result, calculating film width was more difficult for the films grown for 7 min and so the determined thickness has a greater associated error. This sample may also be thinner than expected due to the fact that deposition time was started as soon as the methane was turned on. In actual fact it takes a short time for the methane to enter the reaction chamber and initiate diamond growth so the measured film had, in reality, been growing for less than 7 min.

The thinnest standalone diamond membrane achieved was nanocrystalline with an estimated thickness of 83 nm over a large surface area of  $1 \text{ cm}^2$ , depicted in **Fig.43**.



**Figure 44:** Photograph of the free-standing, nanocrystalline diamond film after a 7 min deposition.

A final investigation completed with AlN substrates was the seeding of two samples using CEST/ND. A 7 min NCD deposition was carried out on the first sample and a 30 min NCD deposition on the second. The growth of a uniform film was successful but it was more difficult to remove from the substrate than when PDDA and PSS-ND were used in the self-assembly procedure. This may be due to the nature of the bonding of the silane monolayer

to the AlN surface. The Si-N bond strength ( $437.1 \text{ kJ mol}^{-1}$ )<sup>7</sup> is much weaker than that of the Si-O bond ( $799.6 \text{ kJ mol}^{-1}$ )<sup>70</sup> and therefore the driving force for spontaneous formation of a self-assembled monolayer on AlN is smaller than it is on silicon. As a result, less silane binds to the substrate surface, which in turn reduces the number of electrostatic interactions that can occur between the silane molecules and nanodiamond particles. Nucleation density decreases and, as a consequence, so does growth rate as it takes longer for a diamond film to become continuous in one plane and begin upwards growth. Thinner films grow in the same amount of time on CEST/ND seeded AlN substrates than on those seeded with PDDA and PSS-ND and they are therefore more difficult to remove. The nanocrystalline diamond membrane grown for 7 min on a CEST/ND seeded substrate is shown in **Fig.45**.



**Figure 45:** Photograph of the diamond membrane after a 7 min NCD deposition, before being removed from the AlN substrate.

#### **10.4 Investigation into the properties of the nanodiamond solution used in self-assembly nucleation**

Nanodiamond solutions with a small average particle size will generate seed layers with a high nucleation density when used in the self-assembly procedure. Four different nanodiamond solutions were investigated, using dynamic light scattering apparatus to determine the average particle size. The particle sizes in solutions of different concentrations, and the influence of sonicating them at different powers and for different lengths of time, were then measured.

### 10.4.1 Nanodiamond from the Carbon Research Institute, Japan

An aqueous colloid dispersion of nanodiamond in water was obtained from the Carbon Research Institute in Japan and was used to make up the PSS-ND solutions (10 w/v %) used in all polymer self-assembly nucleation processes throughout this project. It was also used to make up the nanodiamond solutions used in the CEST seeding processes, unless otherwise stated.

The first investigation with the PSS-ND solution was to measure the effect of sonication on the average size of the polymer-coated nanodiamond particles. To do this a dynamic light scattering measurement of the solution that had not been sonicated was taken first. After this the solutions were sonicated, at 30 % power, for 1 min, 2 min, 3 min, 5 min, 10 min and 20 min and the particle sizes measured again after each sonication. The sonication treatments were consecutive which meant, for example, that the solution sonicated for 2 min had also been sonicated for 1 min previously.

From graph (a) in **Fig.46** it is clear that the amount of sonication time decreases the particle size in the PSS-ND solution. It can also be seen that the solution has a low polydispersity index, indicated by the presence of only one main peak.

After the 20 min sonication, the sample was sonicated for 1 min at 60 % power and finally 1 min at 90 % power to determine if sonication power further reduced the particle size. Average particle sizes were found to be similar to that obtained for the 20 min sonication, as shown in **Table 4** below. This highlighted that once the solution had undergone initial sonication, increasing sonication power makes no difference to the average particle size in the solution.

Following these experiments, the particle sizes in this solution were measured again but with the solution divided into four samples before independent sonication of each one for different amounts of time; 5 min, 10 min and 20 min. One was also left untreated. This enabled a comparison of the two approaches to sonication and whether they have different effects on the average particle size.

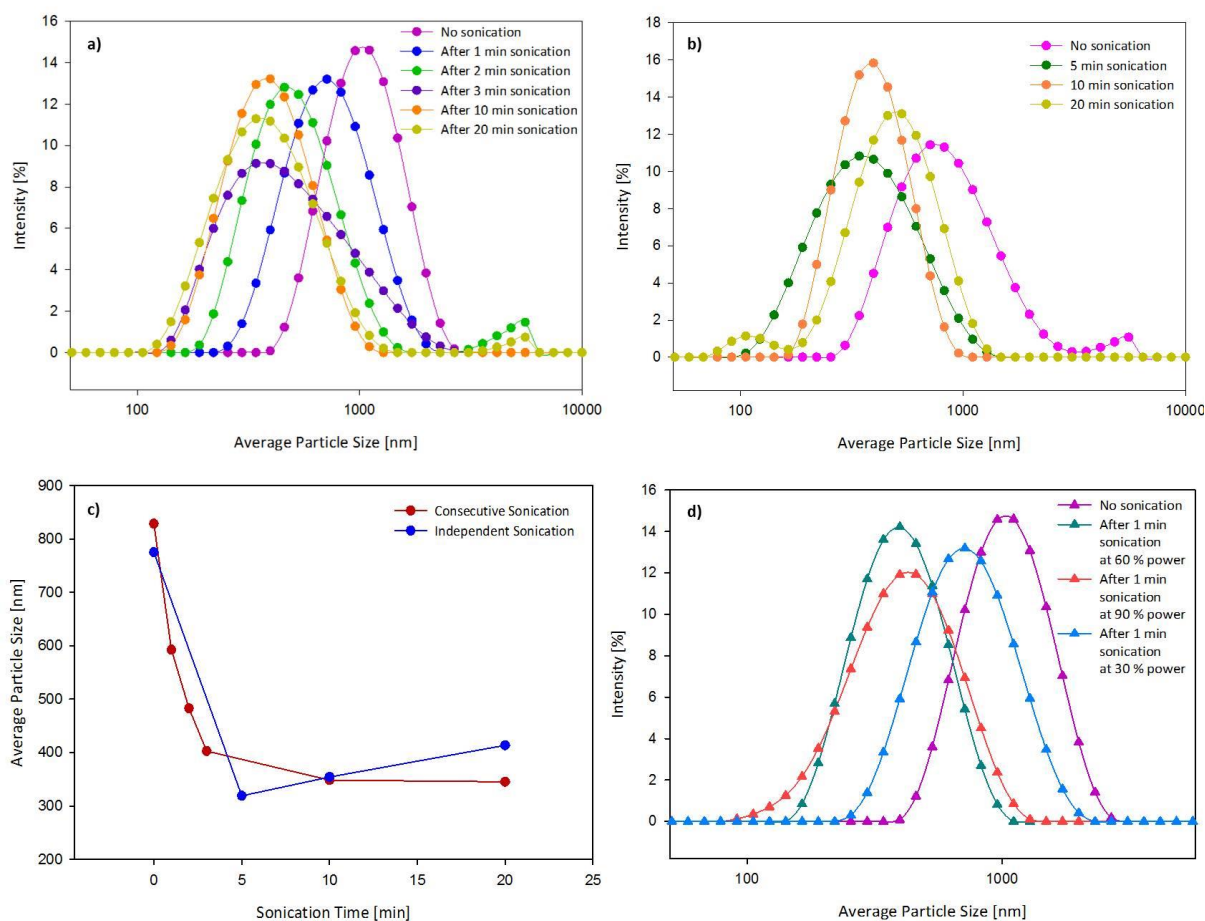


**Figure 46:** Graphs from dynamic light scattering measurements for the PSS-ND (10 w/v %) solution showing a) the effect of sonication time on the particle size distribution when sonication is consecutive b) the effect of sonication time on the particle size distribution when sonication is independent c) the effect of sonication time on the average particle size and d) the effect of sonication power on the particle size distribution.

It is apparent, from **Fig.46(b)**, that the average particle size decreases after 5 min of sonication. There then seems to be little change with longer sonication times of 10 min and 20 min.

**Fig.46(c)** shows a plot of average particle size against sonication time for both consecutive and independent sonication, and allows confirmation of the trends and comparison of the two sonication methods. The plot for consecutive sonication shows a decrease in the average particle size of the solution after the 1 min sonication. The average particle size then continues to decrease, albeit less quickly, until 10 min is reached. At this point the average size is roughly constant and further sonication makes no difference.

Similarly, the plot for independent sonication treatments shows a decrease in the average particle size after the first sonication but then a slight increase is observed with longer sonication times. However, the increase is small and may be attributed to having slightly larger average particle sizes in those particular samples before sonication.

A general trend of an initial decrease in the average particle size after short sonication times, followed by a roughly constant average particle size of around 350 nm, where the average particle size does not change with increasing sonication time, is observed in both plots. Sonication leads to a decrease in the average particle size of colloidal dispersions, breaking up the nanodiamond particle agglomerates that form over time due to strong Coulombic interactions.<sup>72</sup> Sonication provides the driving force necessary to break up these agglomerates until a state is reached where they have all been de-agglomerated. From this point, further sonication will have no effect, visible in **Fig.46(c)** as a constant particle size.

It was concluded that, to achieve a seed layer with the highest nucleation density, the PSS-ND solution should be sonicated for 5 min before being applied to the substrate in seeding processes.

Investigations into the effect of sonication time, sonication power and the concentration of nanodiamond on the average particle size of the ND in water solution that was used in CEST self-assembly processes then took place.

The sonication treatments were carried out consecutively at a power of 30 %, with those at higher powers being conducted after the longest sonication time of 3 min.

From **Tables 4-6** and the graphs in **Fig.47** it is apparent that increasing the sonication time and sonication power makes no noticeable difference to the average particle size of ND in water (**Fig.47(a-b)**). It was concluded that sonication of this solution before use in seeding is unnecessary. It is also evident that decreasing the concentration of the nanodiamond solution increases the particle size (**Fig.47(c-d)**). This is because the solution becomes increasingly unstable with dilution so the solution of 10 w/v % is the best one to use when seeding samples, as it will achieve a high nucleation density with the smallest particle size.

From comparison of the average particle sizes in the PSS-ND solution with those of the ND in water solution, it was observed that the particles are significantly larger in the polymer dispersion. This is due to the nanodiamond particles being coated with high  $M_w$  polymer molecules, compared to being surrounded by small water molecules.

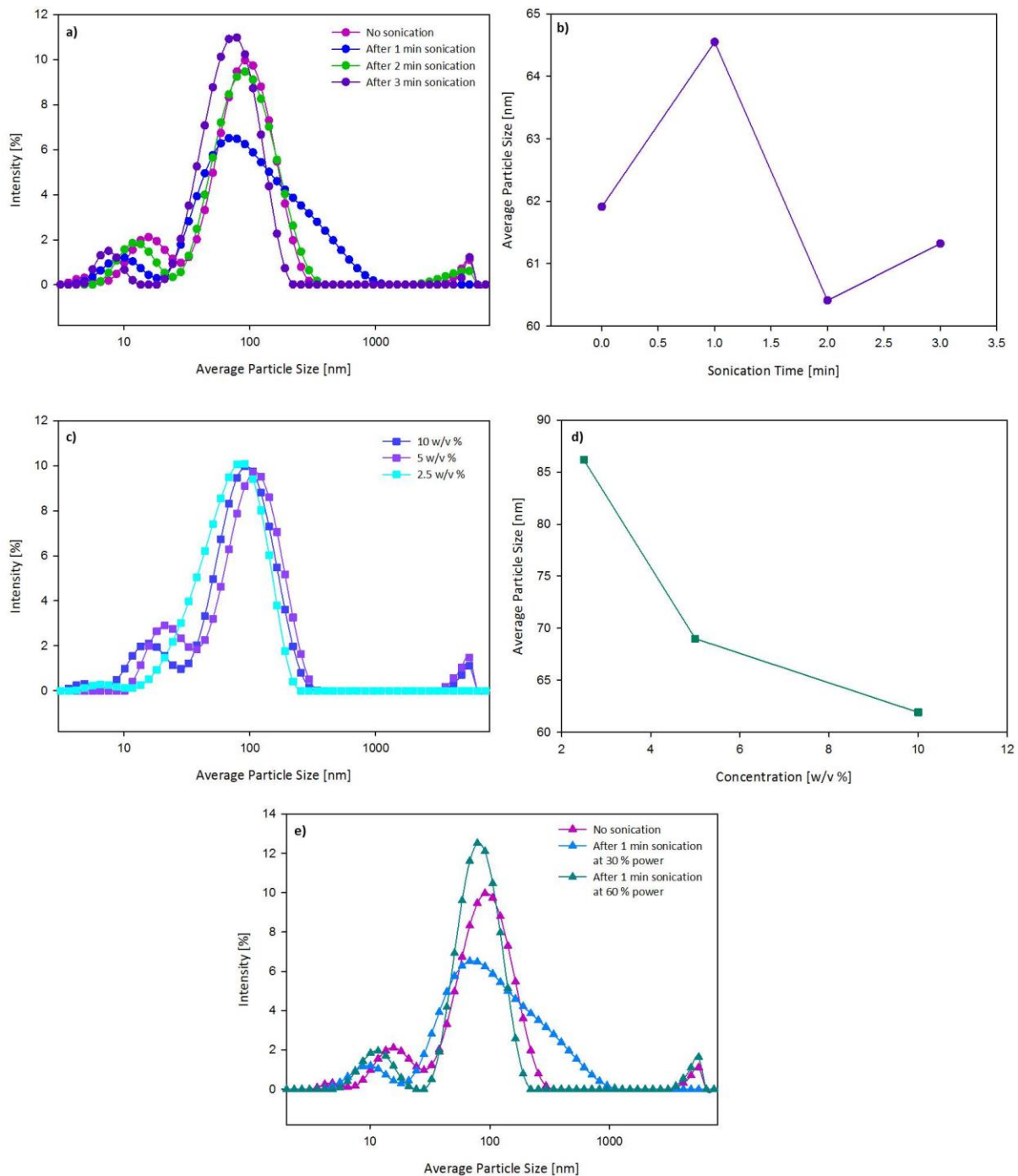


**Figure 47:** Graphs from dynamic light scattering measurements for the ND in DI water solution (10 w/v %) showing a) the effect of sonication time on the average particle size distribution b) the effect of sonication time on the average particle size c) the effect of concentration on the average particle distribution d) the effect of concentration on the average particle size and e) the effect of sonication power on the particle size distribution.

## 10.4.2 Nanodiamond from MicroDiamant: XP 0.018 and XPC 0.018

Measurements of the average particle size found in these two other ND solutions, XP 0.018 and XPC 0.018, obtained from MicroDiamant, Switzerland, were then undertaken in order to evaluate whether they would be better for use in the self-assembly nucleation process.

Although having nominally identical size distributions, it was found that the average particle size in the XP 0.018 solution, before any sonication has taken place, is larger than in XPC 0.018. All further experiments then involved the XPC 0.018 solution, as the smallest average particle size is desirable for use in seeding. The XP 0.018 ND solution is polydisperse, with larger agglomerates as well as smaller ones, and the population of these distributions changes with sonication (**Fig.48(a)**).

The graphs plotted for XPC 0.018 (**Fig.49**) reflect the trend found for the PSS-ND solution. The average particle size in the solution decreases with sonication time until a plateau is reached at around 35 nm (**Fig.49(b)**). As with PSS-ND solutions, 1 min sonication treatments at higher powers of 60 % and 90 %, carried out after the 10 min sonication, make no significant difference to the average particle size.

Furthermore, diluting both the XP 0.018 and XPC 0.018 solutions in DI water increases the average particle size, seen in **Fig.48(b)** and **Fig.49(e)**.

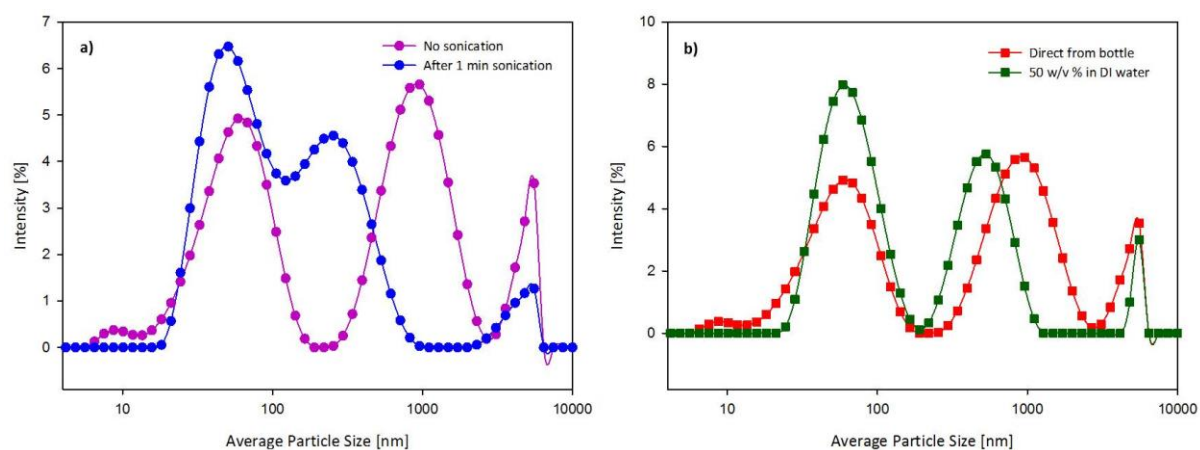


**Figure 48:** Graphs from the dynamic light scattering measurements for the MicroDiamant XP 0.018 solution showing a) the effect of sonication time on the particle size distribution and b) the effect of concentration on the particle size distribution.

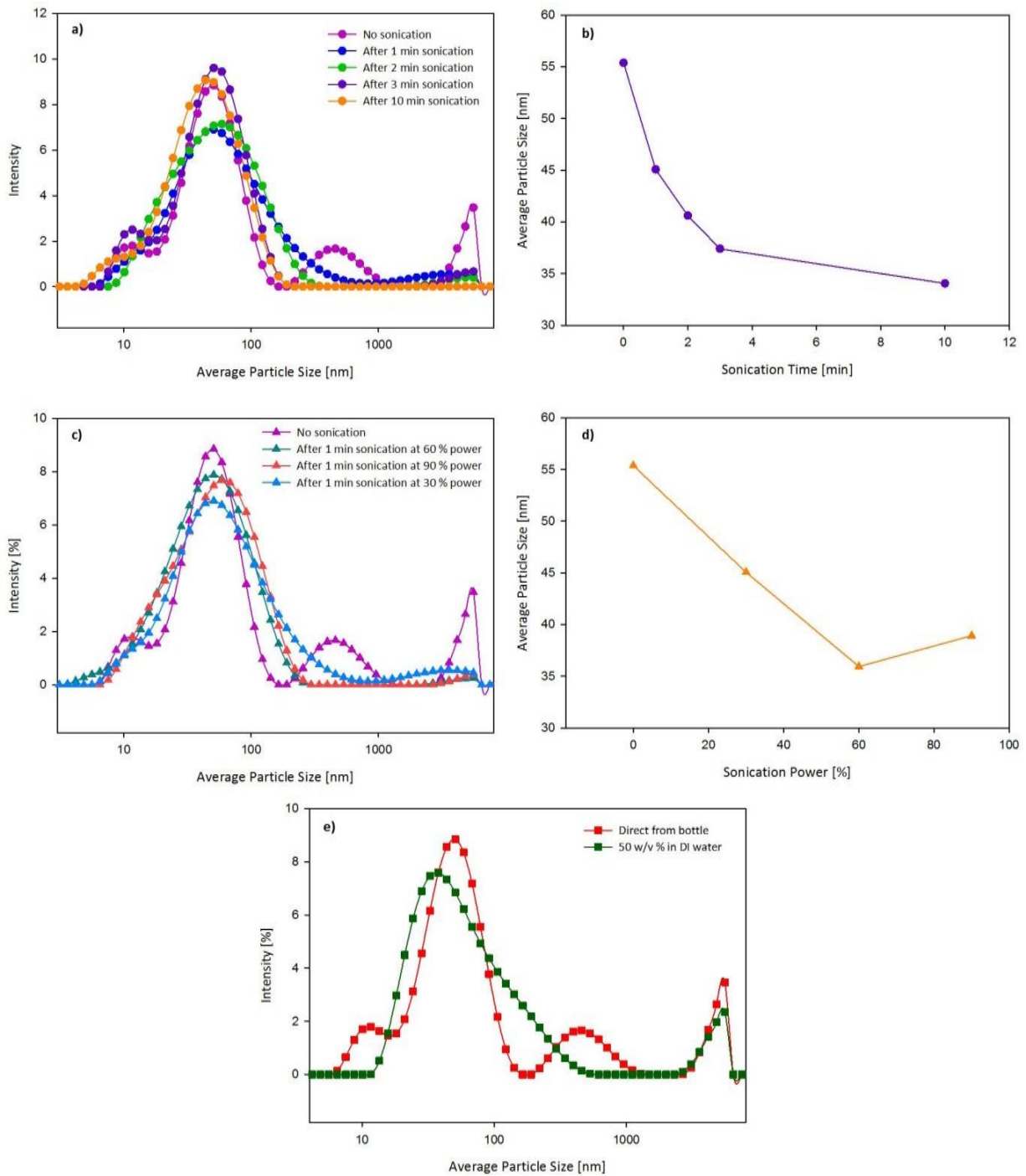


**Figure 49:** Graphs from dynamic light scattering measurements for the MicroDiamant XPC 0.018 solution showing a) the effect of sonication time on particle size distribution b) the effect of sonication time on the average particle size c) the effect of sonication power on average particle size d) the effect of sonication power on the average particle size and e) the effect of concentration on the particle size distribution.

After analysing these results, the self-assembly nucleation process using CEST was attempted on two silicon substrates, replacing the 10 w/v % solution of Japanese ND in DI water with the MicroDiamant XPC 0.018 solution after 3 min sonication.

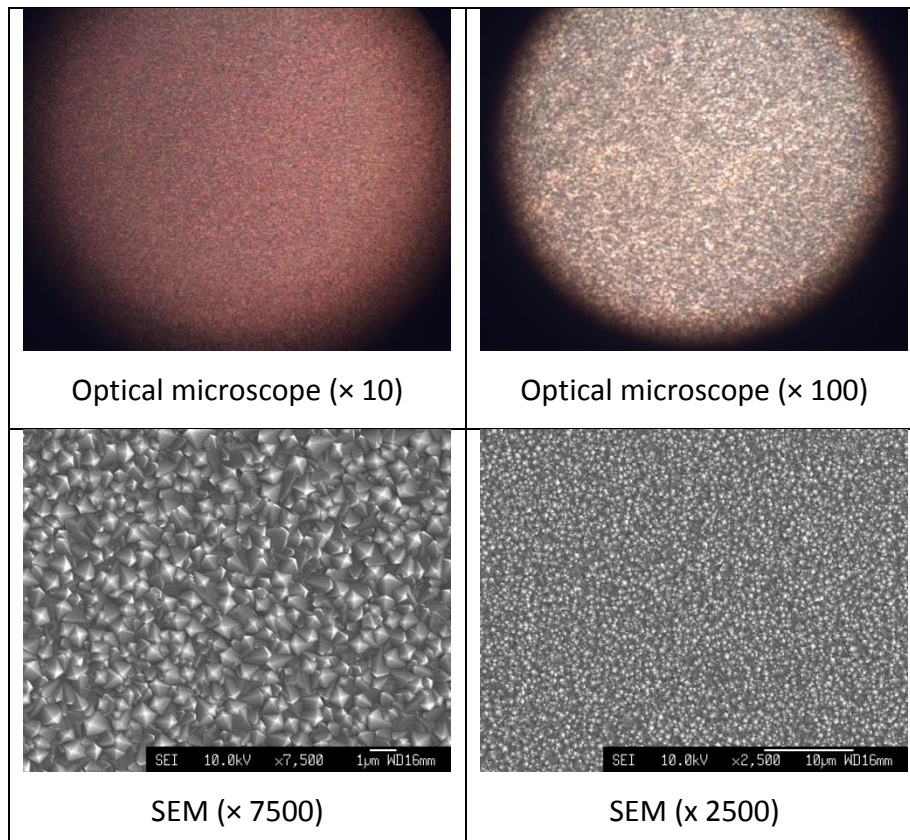


**Figure 50:** Optical microscope and SEM images showing the diamond film after 30 min MCD deposition when the MicroDiamant XPC 0.018 solution was used in the self-assembly process with the silane, CEST.

The diamond layer that resulted from this seeding method was uniform and dense and it can be concluded that this nanodiamond solution is effective in self-assembly nucleation processes.

#### 10.4.3 Nanodiamond in DMSO from University of Gdansk, Poland

The last solution analysed using dynamic light scattering was a colloidal dispersion of deagglomerated nanodiamond in DMSO. This solution exhibited a large decrease in average particle size after a sonication time of 1 min. However, further sonication then led to an increase in particle size, while sonication power, as seen with the other solutions, made no difference to the average particle size. In addition, 50 % dilution with DI water led to a large

increase in average particle size from 93 nm to 1282 nm, as the change of solvents caused spontaneous flocculation of the particles.

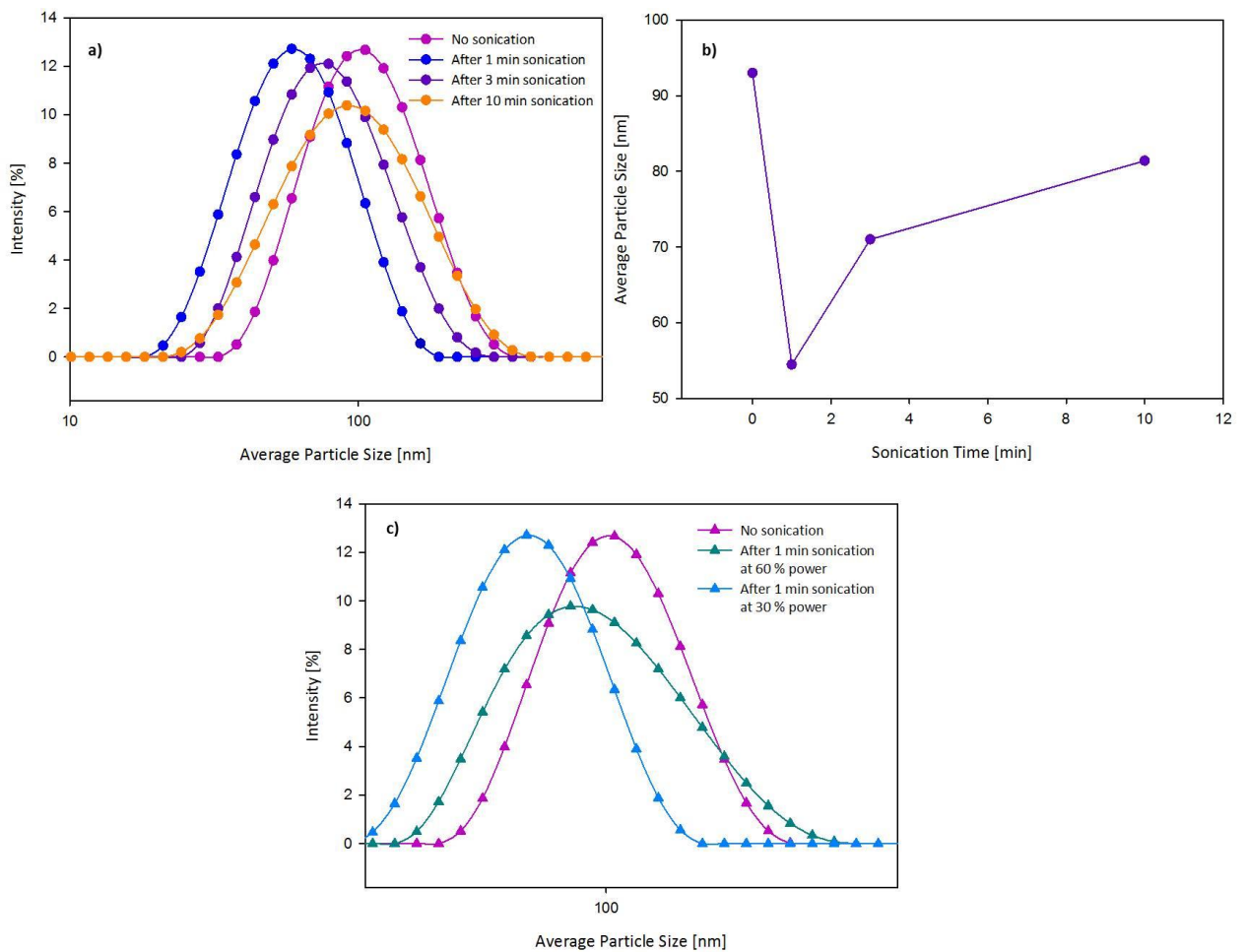


**Figure 51:** Graphs from the dynamic light scattering measurements for the ND in DMSO solution showing a) the effect of sonication time on the particle size distribution b) the effect of sonication time on the average particle size and c) the effect of sonication power on the particle size distribution.

The CEST self-assembly seeding method was trialled on two silicon substrates, using the undiluted ND in DMSO solution after it had been sonicated for 1 min. One substrate was grown on for 15 min and the other for 60 min, both under microcrystalline diamond conditions.

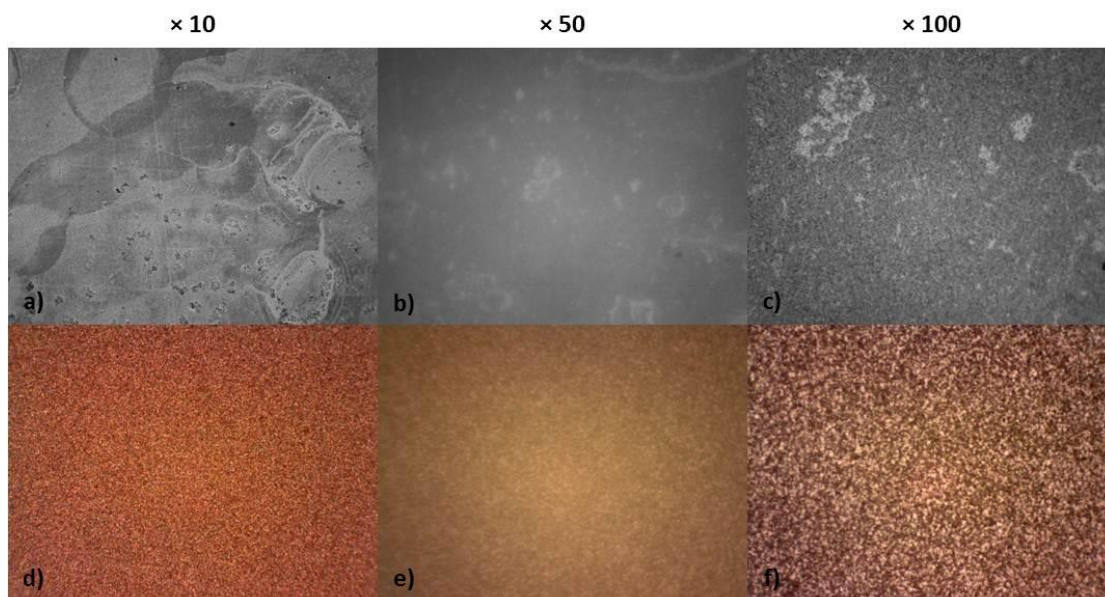


**Figure 52:** Optical microscope images of the films after seeding with CEST and ND in DMSO. Images a), b) and c) are after a 15 min MCD deposition and d), e) and f) after a 60 min MCD deposition. The variation in colour between the two sets is due to adjustments made to the camera to highlight the imperfections in the grown samples.

The diamond sample grown for longer is very uniform, whereas the film grown for only 15 min is not homogenous across the surface. This experiment should be repeated to see if either one is an anomaly, before being able to conclude whether this ND in DMSO solution can be used in self-assembly nucleation processes to produce uniform, dense seed layers.

**Table 4:** The effect of sonication time on the average particle size in the various nanodiamond solutions analysed using dynamic light scattering apparatus.

Solution	Sonication Time [min]	Z-Average [nm]
<b>PSS-ND (10 w/v %)</b>	0	907
<b>(Consecutive sonication)</b>	1	593
	2	483
	3	403
	10	348
	20	345
<b>PSS-ND (10 w/v %)</b>	0	775
<b>(Independent sonication)</b>	5	319
	10	354
	20	414
<b>ND in DI water (10 w/v %)</b>	0	62
	1	65
	2	60

	3	61
<b>XP 0.018</b>	0	134
	1	84
<b>XPC 0.018</b>	0	55
	1	45
	2	41
	3	37
	10	34
<b>ND in DMSO</b>	0	93
	1	54
	3	71
	10	81

**Table 5:** The effect of sonication power on the average particle size in the various nanodiamond solutions analysed using dynamic light scattering apparatus.

<b>Solution</b>	<b>Sonication Power [%]</b>	<b>Z-Average [nm]</b>
<b>PSS-ND (10 w/v %)</b>	0	907
	30	593
	60	382
	90	361
<b>ND in DI water (10 w/v %)</b>	0	62
	30	65
	60	61
<b>XPC 0.018</b>	0	55
	30	45
	60	36
	90	39
<b>ND in DMSO</b>	0	93
	30	54
	60	81

**Table 6:** The effect of concentration on the average particle size in the various nanodiamond solutions analysed using dynamic light scattering apparatus.

<b>Solution</b>	<b>Concentration</b>	<b>Z-Average [nm]</b>
ND in DI water	10 w/v %	62
	5 w/v %	69
	2.5 w/v %	86
XP 0.018	Direct from bottle	134
	50 w/v % in DI water	141
XPC 0.018	Direct from bottle	55
	50 w/v % in DI water	67
ND in DMSO	Direct from bottle	93
	50 w/v % in DI water	1282

## 10.5 Selected-area nucleation

Silicon lens substrates, which are used as moulds for diamond x-ray lenses, can be selectively nucleated so that diamond is deposited in the mould only and not on the top surface, as discussed in **Section 7.2**. During this project experiments were conducted with two methods that can be used to achieve selected-area diamond deposition. The first was to use substrates coated in resist layers that could be lifted off in a suitable solvent and the second was to grow on silicon oxide-coated silicon substrates, then use a buffered oxide etch to remove the oxide layer and any diamond that had grown on it.

### 10.5.1 Resist layer removal

Patterned silicon substrates were used where a photoresist layer remains on their top surfaces after the lens structure has been etched and can, therefore, be used in selected-area nucleation of diamond. Once the substrate had been seeded, the resist layer was removed, taking the nanodiamond particles from the surface that was resist-coated, while leaving the polymer-ND seeding in the etched features that were free from resist. This layer had to be lifted off as quickly as possible in solution to minimise removal of seed particles from within the mould as well.

The lift-off process of different photoresist layers from silicon substrates was investigated, in order to devise a procedure for the most efficient removal. The first two resists experimented with were ma-N2410 and UV-III as they had been used to mask substrates etched in the most recent lens fabrication runs. Ma-N2410 was then investigated again in relation to a new resist, ma-N415, although these tests were carried out on samples that were un-etched and the resist layer likely to be less well attached to the substrate. The ma-N resist layers were removed with acetone and the UV-III resist layers lifted off in a solution of Nanostrip® (a mixture of sulfuric acid and hydrogen peroxide) while varying the amount of agitation, heating, time in the lift-off solution and substrate treatment (cleaning and seeding).

After conducting this series of experiments, procedures to completely remove the various resist layers in the shortest amount of time were devised. It was found that both ultrasonic agitation and heating of the lift-off solution reduce the time required to remove the resist layer and that seeding the sample on top of the resist makes no difference to the lift-off

time. It was shown that submerging the substrate in the lift-off solution for 30 seconds is more effective than submerging it for a total of 30 seconds but in 10 second intervals, with drying in between each immersion. This is because the drying step dries the resist back onto the substrate, making it harder to remove. The resultant method to remove ma-N2410 is to agitate it for 10 s in a solution of acetone heated to 50 °C. UV-III was found to be most effectively removed using a similar approach, using Nanostrip® rather than acetone. Ma-N415 was found to lift-off the substrate very easily by agitating in acetone in an ultrasonic bath for just 2.5 s and ma-N2410, on silicon substrates that had not been etched after resist application, lifted off under the same conditions for 5 s. It is evident that the resist layers on substrates that had not yet been etched were more easily removed. This is due to the fact that during the etch process the resist layer gets baked onto the substrate, making it more difficult to remove.

After resist removal, 15 min MCD depositions were conducted on the samples where the resist layer had completely lifted-off. The first ma-N2410 and UV-III test samples were initially entirely coated in a resist layer (not patterned) and so after lift-off of the resist, no diamond deposition on the silicon substrate, after 15 min in the CVD system, confirmed the successful nucleation layer removal. Conversely, with the ma-N415 and second set of ma-N2410 samples, the resist layer was only present on particular areas of the substrate. When these samples were grown on in the microwave reactor, selected-area deposition was achieved. This indicated that the ND nucleation layer was successfully removed only from the areas where the resist layer was located and diamond growth occurred exclusively on the seeded silicon areas.

**Table 7** shows the conditions used to remove the resist layers from each sample and photographs of each substrate after each stage in the resist removal process, and after CVD in the microwave reactor if applicable, are depicted in **Appendix 14.7**.

**Table 7:** Conditions used to remove the resist layer from each sample.

Resist	Sample	Lift-off Solution	Substrate Treatment	Manual Shaking?	Ultrasonic Bath?	Time	Heat?
<b>ma-N2410</b>	1	Acetone	Seeded	Y	N	30 s (5 s intervals)	N
	2	Acetone	Seeded	Y	N	30 s	N
	3	Acetone	Seeded	Y	Y	30 s (5 s intervals)	N
	4	Acetone	Seeded	Y	Y	30 s	N
	5	Acetone	Seeded	Y	N	30 s (10 s intervals)	30 °C
	6	Acetone	Seeded	Y	N	10 s	50 °C
	7	Acetone	Seeded	Y	Y	5 s	50 °C
	8	Acetone	Seeded	Y	Y	5 s	30 °C
	9	Acetone	Washed with DI water	Y	Y	10 s	N
	10	Acetone	Non-washed, non-seeded	Y	Y	10 s	N
	11	Acetone	Seeded	Y	Y	10 s	N
	12	Acetone	Seeded	y	Y	5 s	N
	13	Acetone	Seeded	Y	Y	7 s	N
	CRL	Acetone	Seeded	Y	Y	30 s (5 s intervals)	50 °C
	Kinoform	Acetone	Seeded	Y	Y	10 s	50 °C
<b>UV-III</b>	1	Nanostrip	Seeded	Y	Y	40 s (10 s intervals)	N
	2	Nanostrip	Seeded	Y	Y	30 s	N
	3	Nanostrip	Seeded	Y	Y	60 s	N
	4	Nanostrip	Seeded	Y	Y	20 s (10 s intervals)	30 °C
	5	Nanostrip	Seeded	Y	Y	10 s	30 °C
	6	Nanostrip	Seeded	Y	Y	10 s	30 °C
	7	Nanostrip	Non-seeded	Y	Y	20 s (10 s intervals)	30 °C
	8	Nanostrip	Non-seeded	Y	Y	10 s	30 °C
	9	Nanostrip	Non-seeded	Y	Y	20 s	30 °C
	10	Nanostrip	Non-seeded	Y	Y	15 s	50 °C
	11	Nanostrip	Non-seeded	Y	Y	20 s	50 °C

<b>ma-N415</b>	55(1)	Acetone	Seeded	Y	Y	10 s	N
	55(2)	Acetone	Seeded	Y	Y	5 s	N
	55(3)	Acetone	Seeded	Y	Y	5 s	N
	55(4)	Acetone	Seeded	Y	Y	2.5 s	N
	70(1)	Acetone	Seeded	Y	Y	5 s	N
	70(2)	Acetone	Seeded	Y	Y	2.5 s	N
	85(1)	Acetone	Seeded	Y	Y	5 s	N
	85(2)	Acetone	Seeded	Y	Y	2.5 s	N
	115(1)	Acetone	Seeded	Y	Y	5 s	N
	115(2)	Acetone	Seeded	Y	Y	2.5 s	N
<b>ma-N2410(2)</b>	100	Acetone	Seeded	Y	Y	5 s	N
	200(1)	Acetone	Seeded	Y	Y	2.5 s	N
	200(2)	Acetone	Seeded	Y	Y	5 s	N
	300	Acetone	Seeded	Y	Y	5 s	N
	400	Acetone	Seeded	Y	Y	5 s	N



**Figure 53:** Photographic sequence of selected-area deposition.

In **Fig.53** the various stages of selected-area deposition are visible. From left to right, the first image shows the resist substrate after it had been seeded using the PDDA and PSS-ND method. The darker patches are the ma-N415 layer and the lighter areas are the bare silicon. The second image shows the substrate after resist removal according to the procedure for ma-N415 outlined previously. The right-hand image shows the substrate after it had been grown on in the microwave reactor. It is clear that diamond, visible as the light areas in the image, has selectively grown only in the areas where the resist was absent prior to lift-off. After these promising results, the ma-N2410 resist layer removal method was applied to two lens-mould substrates and is discussed in **Section 10.6**.

### **10.5.2 Buffered oxide etch (BOE)**

A buffered oxide etch is a technique that removes the thermal silicon oxide layer from the surface of a silicon substrate by treating it with a buffered solution containing hydrofluoric acid.<sup>73</sup> Therefore, it can be used to remove silicon oxide coatings, and any diamond on the oxide, from silicon substrates that have had a diamond layer applied using chemical vapour deposition. When carried out on a lens-mould substrate partially coated with an oxide layer, the diamond would be removed from the substrate surface with the silicon oxide layer, but remain in the mould features where there is no silicon oxide. A non-continuous diamond layer would be most effective in this process as the wet etch would then undercut the diamond quickly.

To investigate whether this method might be feasible with lens-mould substrates, diamond depositions were carried out on a number of silicon oxide-coated silicon substrates, both seeded and non-seeded, under varying deposition conditions, given in **Table 8**. Each one was imaged using SEM before it underwent a buffered oxide etch. The samples were then imaged again for comparison of before and after the wet etch step (**Appendix 14.8**. SEM images after the wet etch step were not taken of SiO7 and SiO8).

**Table 8:** Seeding and deposition conditions used on the silicon oxide-coated samples.

	Seeding	CVD parameters	Time [min]	
<b>SiO1</b>	-	NCD	2.5	
<b>SiO2</b>	-	NCD	30	
<b>SiO3</b>	-	MCD	30	
<b>SiO4</b>	-	NCD	30	+ Si11
<b>SiO5</b>	-	MCD	30	+ Si12
<b>SiO6</b>	PDDA/PSS-ND	MCD	2.5	
<b>SiO7</b>	PDDA/PSS-ND	MCD	2.5	
<b>SiO8</b>	PDDA/PSS-ND	NCD	2.5	
<b>SiO9</b>	PDDA/PSS-ND	NCD	2.5	
<b>SiO10</b>	CEST/ND	MCD (25 sccm CH <sub>4</sub> )	2.5	
<b>SiO11</b>	CEST/ND	MCD (15 sccm CH <sub>4</sub> )	2.5	

The first three samples were grown on to evaluate the diamond deposition on un-nucleated substrates and determine the deposition time that should be used. Not enough diamond was grown in a 2.5 min deposition to provide a useful comparison after a buffered oxide etch step so the second and third samples were grown for 30 min under NCD deposition conditions and 30 min MCD deposition conditions, respectively. It was found that enough diamond had grown after 30 min to test the buffered oxide etch process so this time was used for the remainder of the investigation with un-nucleated substrates.

The next silicon oxide substrates (SiO4 and SiO5) were both un-nucleated and there was minimal diamond growth after 30 min NCD or MCD depositions but enough to test the wet etch. After the buffered HF wet etch, there is even less diamond present in both cases, indicating that the buffered oxide etch is a successful technique at lifting off the oxide layer and some, though not all, diamond. However, it is difficult to ascertain the extent to which

the process is useful for selected-area nucleation, since there was minimal diamond to begin with. When the substrates were seeded before NCD or MCD deposition, there was significantly more diamond present before the etch step after only a 2.5 min growth step. It was again evident that the diamond coverage was less dense after the buffered oxide etch. However, there was still a significant amount of diamond present on the silicon surface and it was concluded that the technique is not likely to be suitable for the purpose of inducing selected-area nucleations for fabricating high-aspect-ratio lenses from diamond.

On comparison of the diamond growth on subsequent silicon oxide samples (SiO10 and SiO11) with that on SiO9, it was noticeable that the coverage was less uniform on samples SiO10 and SiO11. These samples were seeded using CEST/ND whereas SiO9 was seeded using PDDA and PSS-ND. As has already been seen, the use of CEST in self-assembly usually generated a very uniform diamond layer. This was not the case with silicon oxide surfaces as the mechanism of self-assembled monolayer formation cannot proceed. The formation of a siloxane bond between the silanol head group of the CEST molecule and a surface silicon atom of the substrate cannot take place as the surface is oxygen terminated. Therefore, there is a much smaller driving force for the reaction and a monolayer assembles much less readily. As a consequence, the resultant seed particles are less evenly distributed across the silicon oxide substrate surface and this is reflected in the inhomogeneous diamond film that grows.

### **10.5.3 Diamond deposition on substrates fabricated by Kelvin Nanotechnology**

To investigate other partial-oxide removal processes, five silicon-oxide coated silicon substrates, with a number of trenches etched with different aspect ratios (DL10, DL11, DL13, DL15 and DL16), were fabricated at Kelvin Nanotechnology, Glasgow. After a short diamond seed layer deposition, each sample had its silicon oxide layer etched off in a different way in an attempt to achieve selected-area diamond deposition when grown on for a second time in the microwave reactor. The trenches of varying aspect ratios etched into each sample enabled comparison of diamond filling across different aspect ratios. The etch procedures employed were as follows: etching of the oxide layer using 1) un-buffered HF (DL16), 2) Al PAD etch (DL13) and 3) buffered HF etch with native oxide removal before diamond seed layer deposition (DL11) and without native oxide removal (DL10 and DL15). For the second deposition step each one was grown on for 3 h before being cleaved with

the laser machining system to enable the cross-section of each sample to be viewed by SEM. The trench height,  $H$ , width,  $W$ , (top and bottom), aspect ratio, thickness of the diamond growth in various areas,  $\tau$ , and percentage filling,  $\varphi\%$ , for each different sized trench of each sample were then calculated from the images.

**Table 9:** Mould filling measurements for the DL samples where  $H$  and  $W$  are the height and width of the trenches, respectively.

Sample	Feature	$H$ ( $\mu\text{m}$ )	$W$ (Bottom) ( $\mu\text{m}$ )	$W$ (Top) ( $\mu\text{m}$ )	Aspect Ratio	$\tau_B$ ( $\mu\text{m}$ )	$\tau_T$ ( $\mu\text{m}$ )	$\tau_C$ ( $\mu\text{m}$ )	$\tau_S$ ( $\mu\text{m}$ )	$\varphi\%$
<b>DL10</b>	<b>Trench1</b>	49.94	23.40	19.61	2.13	1.80	5.27	4.95	2.18	3.60
	<b>Trench2</b>	40.74	8.59	6.93	4.74	0.64	5.28	5.06	0.75	1.56
	<b>Trench3</b>	50.51	22.91	20.10	2.20	1.97	5.82	6.91	2.07	3.90
	<b>Trench4</b>	24.76	1.69	1.05	14.64	0.00	5.99	0.00	0.00	0.00
<b>DL11</b>	<b>Trench1</b>	50.79	23.14	20.66	2.19	2.08	5.04	4.68	2.16	4.09
	<b>Trench2</b>	45.79	14.42	11.74	3.18	1.16	4.79	4.22	1.41	2.52
<b>DL13</b>	<b>Trench1</b>	54.38	22.93	19.36	2.37	1.99	6.71	4.92	1.94	3.67
	<b>Trench2</b>	48.48	13.89	11.11	3.49	1.08	5.23	4.26	1.01	2.22
	<b>Trench3</b>	25.85	6.50	3.78	3.98	1.36	-	-	1.10	5.25
<b>DL15</b>	<b>Trench1</b>	28.40	3.00	3.38	9.47	0.00	5.90	1.62	0.00	0.00
	<b>Trench2</b>	52.63	23.40	19.88	2.25	1.81	5.32	4.62	2.42	3.44
	<b>Trench3</b>	47.43	14.07	11.37	3.37	1.10	4.99	4.03	1.12	2.32
	<b>Trench4</b>	42.33	7.46	6.45	5.68	0.00	5.34	3.17	0.00	0.00
<b>DL16</b>	<b>Trench1</b>	54.93	23.33	20.57	2.35	1.96	5.27	5.38	2.11	3.57
	<b>Trench2</b>	50.04	14.36	11.24	3.48	0.90	6.83	5.33	0.71	1.79
	<b>Trench3</b>	42.86	8.56	7.42	5.01	0.00	4.09	0.00	0.00	0.00

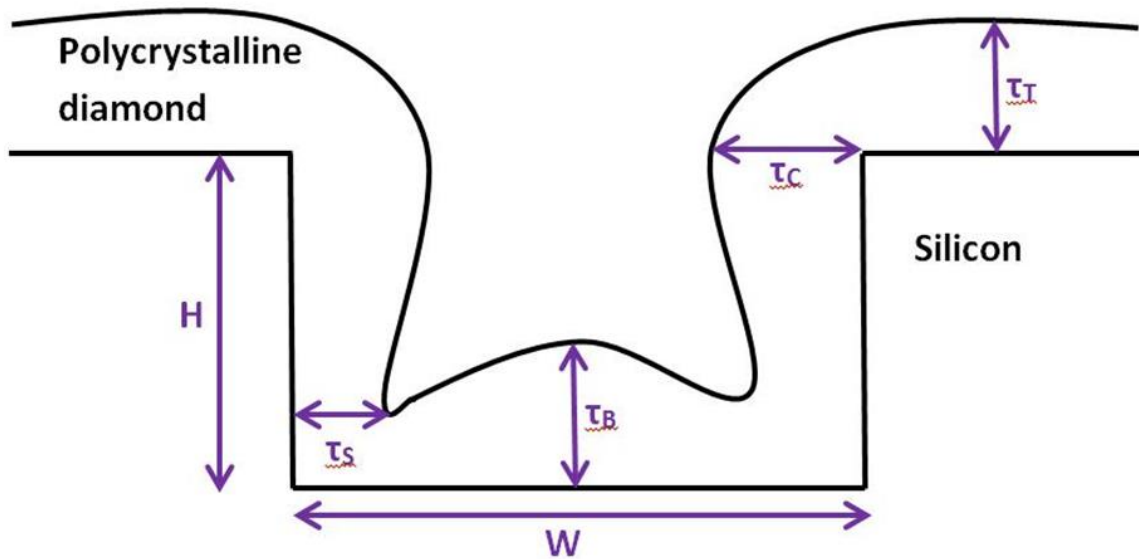


**Figure 54:** Schematic drawing of an etch feature partially filled with polycrystalline diamond. The dimensions where mould-filling measurements were taken are labelled.

From the SEM images (**Appendix 14.9**), it is evident that none of the methods achieved complete suppression of diamond deposition on the substrate surface where the oxide had been. Diamond had also grown over the opening of many of the narrowest trenches, preventing any further diamond deposition at the bottom of the trench. That means that the highest aspect ratio trenches have percentage filling values of 0. The images of the sample surfaces show that the method used to etch DL10 has worked most successfully as the density of diamond is the least on this top surface. DL13 and DL16 have continuous diamond layers on their surfaces and so have been etched least effectively using the unbuffered and Al PAD processes.

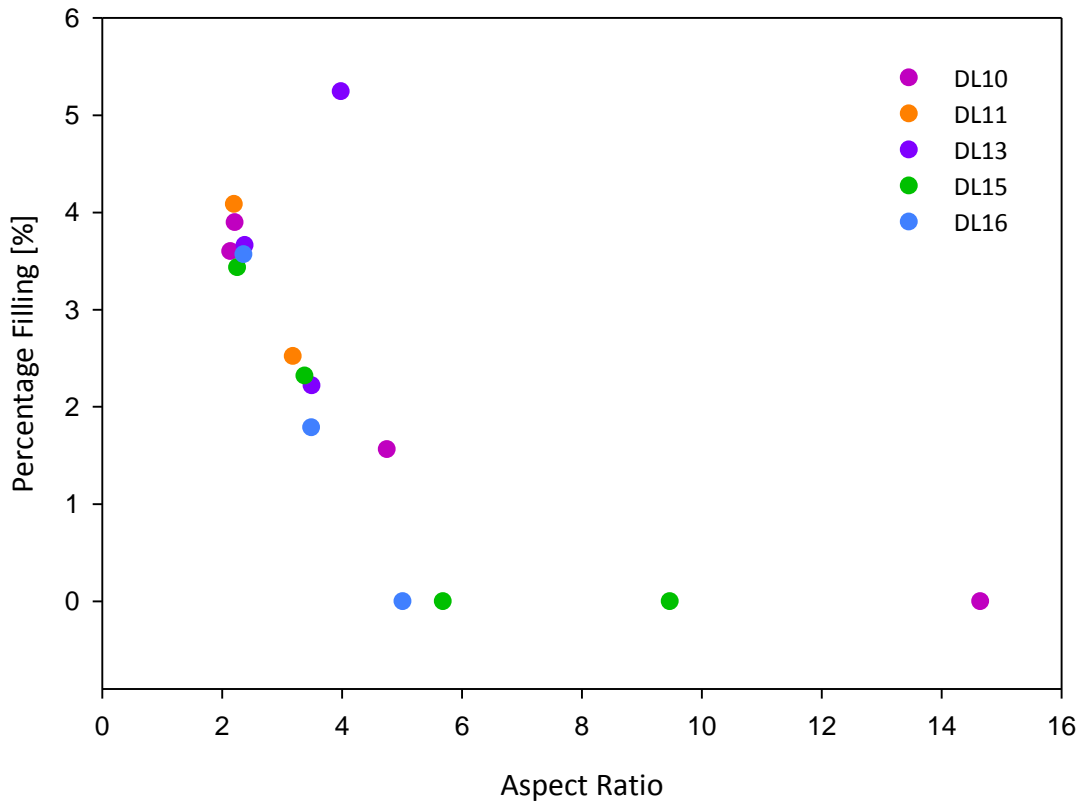


**Figure 55:** Graph showing percentage filling against aspect ratio for the DL samples.

**Fig.55** shows the plot of aspect ratio against percentage filling of the trenches and the trend of decreasing diamond filling at higher aspect ratios. This trend is expected as it has already been seen that the filling of deep, narrow trenches (high aspect ratios) is stopped when diamond grows over the trench opening. This problem is particularly important to address as future lens-mould substrates will have increasingly high aspect ratio features that must be effectively filled with diamond.

After the analysis of each sample and comparison between them, the conclusion was reached that none of the oxide-etch techniques yielded a selected-area deposition that was selective enough to be used on lens substrates to generate freestanding nanofocusing refractive lenses from diamond. It was decided that further development of the resist lift-off process was a better route to take towards selected-area nucleation.

## 10.6 Application of selected-area, self-assembly nucleation using resist lift-off to lens-mould substrates

Since the aim of this project was to work towards fabricating a refractive nanofocusing lens from polycrystalline CVD diamond, it was important to apply both the optimised electrostatic self-assembly nucleation involving PDDA and PSS-ND, and the new self-assembly using CEST and ND, to real lens-mould substrates to ensure they worked.

When the CEST/ND self-assembly nucleation was applied to two silicon CRL substrates coated in the ma-N2410 resist, the silane started to attack the edges of the resist layer and caused it to degrade before nucleation was complete. This meant that this could not be used as a viable technique to seed ma-N coated substrates. If more time were available, experiments with further resist layers could be carried out to determine if there are resist layers that CEST-seeding is compatible with.

The next experiment with lens-mould substrates was to apply the polymer seeding method to two kinoform lens substrates, (RAL132 and RAL133), partially coated with ma-N2410 resist. After seeding, these resist layers were removed by agitating the samples in acetone in an ultrasonic bath until the resist had lifted off. RAL132 required longer in the acetone than RAL133 so a 10 h MCD deposition was conducted on each sample to discover if this had an adverse effect on the amount of diamond deposited after the same amount of time.

The SEM images (**Appendix 14.10**) and measurements in **Table 10** of diamond deposition in each trench show that the amount of diamond growth is similar in both samples. There is slightly less diamond in each recess of RAL132 and this is expected as it spent longer time in the acetone bath and, hence, more nucleation sites were removed from the etch features than in RAL133. It is also evident that selected-area deposition has not been very successful as there is still diamond deposited on the top surface of both substrates. The conclusion was reached that a more effective resist removal method needed to be devised. This was carried out and has already been discussed in **Section 10.5.1**.

After the successful selected-area depositions described in **Section 10.5.1**, the ma-N2410 resist layers were removed from two PDDA/PSS-ND-seeded lens-mould substrates, according to the standard procedure, to see if the same selectivity could be achieved. One was a compound refractive lens and the other a kinoform lens, labelled RAL135 and RAL136

in **Table 10**, respectively. The resist did not lift off the CRL lens-mould substrate as easily as it had performed with the planar substrates so it was deposited on for only 3 h. Typically, lens-mould substrates were grown on for 18 h, so that deep trenches can be filled, but it was decided that this would not have been worthwhile considering some of the resist layer was still present and selected-area deposition was unlikely to be successful. In contrast, resist removal from sample RAL136 worked faster and this substrate was grown on for the full 18 h. After deposition, both samples were analysed with SEM imaging of the cross-sections (**Appendix 14.11**) and the percentage filling of the moulds, and growth rates on the surface and at the bottom of the trenches, were calculated.

The SEM images of RAL 135 show a much lower nucleation density on the substrate surface than in the mould, as individual diamond crystals can be seen on the surface. The diamond in the moulds appears smooth and uniform, with approximately the same amount of diamond growing on the sides,  $\tau_s$ , as at the bottom,  $\tau_b$ . A uniform diamond coating is essential for x-ray lens fabrication because it will result in fewer lens aberrations and less scattering of radiation, leading to a more intense focal spot and better resolution. From the images of the substrate surface there are clear areas of much higher diamond density than others, which are the areas where the resist layer did not lift-off completely.

The images of RAL136 also show good selectivity between the substrate surface and the mould, even after a much longer deposition of 18 h. Much less diamond has grown on the top surface of this substrate than on both RAL132 and RAL133 (**Fig.56**), despite a longer deposition time. This suggests that the resist removal method used on RAL136 was much more effective. Furthermore, very good percentage filling of the trenches had been achieved, with a maximum of 82.59 % in trench 2.

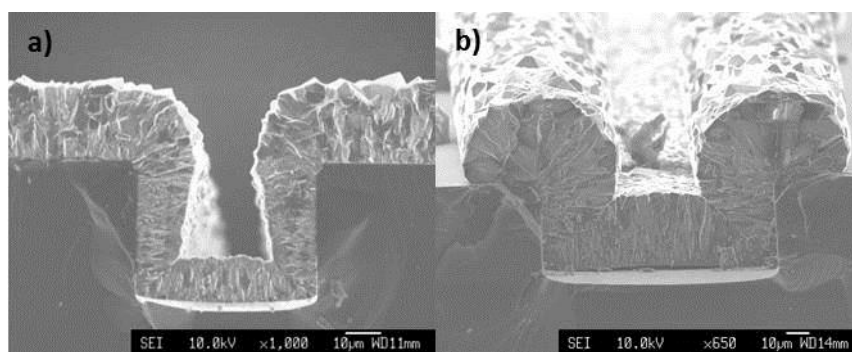


**Figure 56:** Diamond deposition in an etch feature of a) RAL133 and b) RAL136.

On comparison of samples RAL135 and RAL136, significant diamond growth can be seen on the surface of both substrates at the corners of the etch features. This has caused the closing of trench 1 of RAL136 and prevented further filling of that mould. The rate of deposition on these edges is increased by both the spontaneous nucleation of diamond along a silicon defect (edge) and an increased electric field density leading to higher surface temperature, and therefore deposition rate, at these corners.

From the diamond growth measurements it can be seen that the diamond growth rate at the bottom ( $G_B$ ) of trenches with the highest aspect ratios is slowest, leading also to the lowest percentage filling,  $\phi_{\%}$ , for these features. This might become problematic since lens-mould substrates with high aspect ratio features will be required in future designs. However, the etch feature with the highest aspect ratio on sample RAL136 has a filling percentage of 44.23 %, which is much higher than was achieved with trenches of comparable aspect ratios in the other resist substrates.

Additionally, the growth rate of diamond on the top surface is faster than at the bottom of the trenches for all RAL samples. From the data in **Table 10** it is apparent that the two rates are most similar for sample RAL136, highlighting once again the fact that this was the most successful selected-area, self-assembly nucleation attempt. In conclusion, the selectivity seen when using the resist removal method developed in **Section 10.5.1** is much higher than has been achieved previously. More effective resist masking at the edge of the trenches could increase this still further, leading to a more efficient, selective way to fabricate diamond x-ray lenses.

**Table 10:** Mould filling measurements for RAL132, RAL133, RAL135 and RAL136.

Sample	Trench	$H$ [ $\mu\text{m}$ ]	$W$ [ $\mu\text{m}$ ]	Aspect Ratio	$\tau_B$ [ $\mu\text{m}$ ]	$\tau_T$ [ $\mu\text{m}$ ]	$\tau_C$ [ $\mu\text{m}$ ]	$\tau_S$ [ $\mu\text{m}$ ]	$\varphi\%$ [%]	$G_T$ [ $\mu\text{m h}^{-1}$ ]	$G_B$ [ $\mu\text{m h}^{-1}$ ]
RAL132	Trench1	36.449	51.402	0.71	10.561	20.951	15.177	9.625	28.97	2.10	1.06
	Trench2	36.355	26.168	1.39	5.140	21.088	11.548	5.227	14.14	2.11	0.51
	Trench3	36.542	26.822	1.36	5.421	21.738	12.137	5.813	14.83	2.17	0.54
	Trench4	36.449	26.355	1.38	5.234	21.278	12.800	5.48	14.36	2.13	0.52
	Trench5	37.850	51.495	0.74	11.215	21.252	14.763	9.55	29.63	2.13	1.12
RAL133	Trench1	38.972	50.561	0.77	12.710	24.191	16.775	12.03	32.61	2.42	1.27
	Trench2	38.598	25.981	1.49	5.888	23.196	13.195	5.706	15.25	2.32	0.59
	Trench3	38.785	25.794	1.50	5.794	21.863	13.684	6.028	14.94	2.19	0.58
	Trench4	38.972	51.495	0.76	12.804	21.809	17.333	12.02	32.85	2.18	1.28
RAL135	Trench1	42.783	53.821	0.79	4.151	5.077	5.151	4.174	9.70	1.69	1.38
	Trench2	44.982	46.169	0.97	3.871	5.587	5.127	3.871	8.61	1.86	1.29
	Trench3	44.784	35.195	1.27	3.083	5.304	4.711	3.722	6.88	1.77	1.03
RAL136	Trench1	38.539	51.248	0.75	17.045	33.966	27.75	17.22	44.23	1.89	0.95
	Trench2	37.403	98.464	0.38	30.892	34.616	31.912	30.81	82.59	1.92	1.72
	Trench3	38.972	75.112	0.52	24.738	35.348	31.065	26.20	63.48	1.96	1.37

## 10.7 The effect of varying the concentration of N<sub>2</sub> and Ar added to the H<sub>2</sub>/CH<sub>4</sub> gas mixture used in diamond MWCVD

The gas mixture used in diamond MWCVD affects the morphology, surface roughness and grain size of the deposited diamond crystals. To determine the effect that nitrogen and argon additions to the standard H<sub>2</sub>/CH<sub>4</sub> plasma have on the diamond film, a methodical investigation was implemented. Thirty silicon substrates were seeded using PDDA and PSS-ND and deposited on for 1 h, in a gas mixture containing a different concentration of nitrogen and argon in addition to H<sub>2</sub> and CH<sub>4</sub>. The various gas mixtures used are shown in a table in **Appendix 14.1**. Analysis of each film using both the optical microscope and SEM analysis (**Appendices 14.12 and 14.13**) enabled comparison of the size, orientation and surface roughness of the crystals of each film. (Five samples (Si16, Si26, Si27, Si42 and Si43) could not be imaged by SEM and are therefore missing from **Appendix 14.13**). Analysis using UV-Raman spectroscopy (**Fig.57**) allowed characterisation of some of the films.

**Table 11:** Table of calculated  $I(sp^3)$  values for the various diamond films.

$\chi_0(N_2)$ [%]	$\chi_0(Ar)$ [%]	Background Intensity	Diamond Peak Intensity	$I(sp^3)$
<b>0.00</b>	0.0	284.8	9044.0	8759.2
	3.8	288.9	8707.7	8418.8
	11.4	289.7	8547.2	8257.5
	22.9	293.7	3617.9	3324.2
	38.1	254.3	865.8	611.5
	<b>0.38</b>	0.0	289.5	1759.9
3.8		293.7	2127.9	1834.3
7.6		284.8	2084.2	1799.4
11.4		294.5	1773.3	1478.8
22.8		276.3	1265.1	988.8
38.0		257.6	782.9	525.3

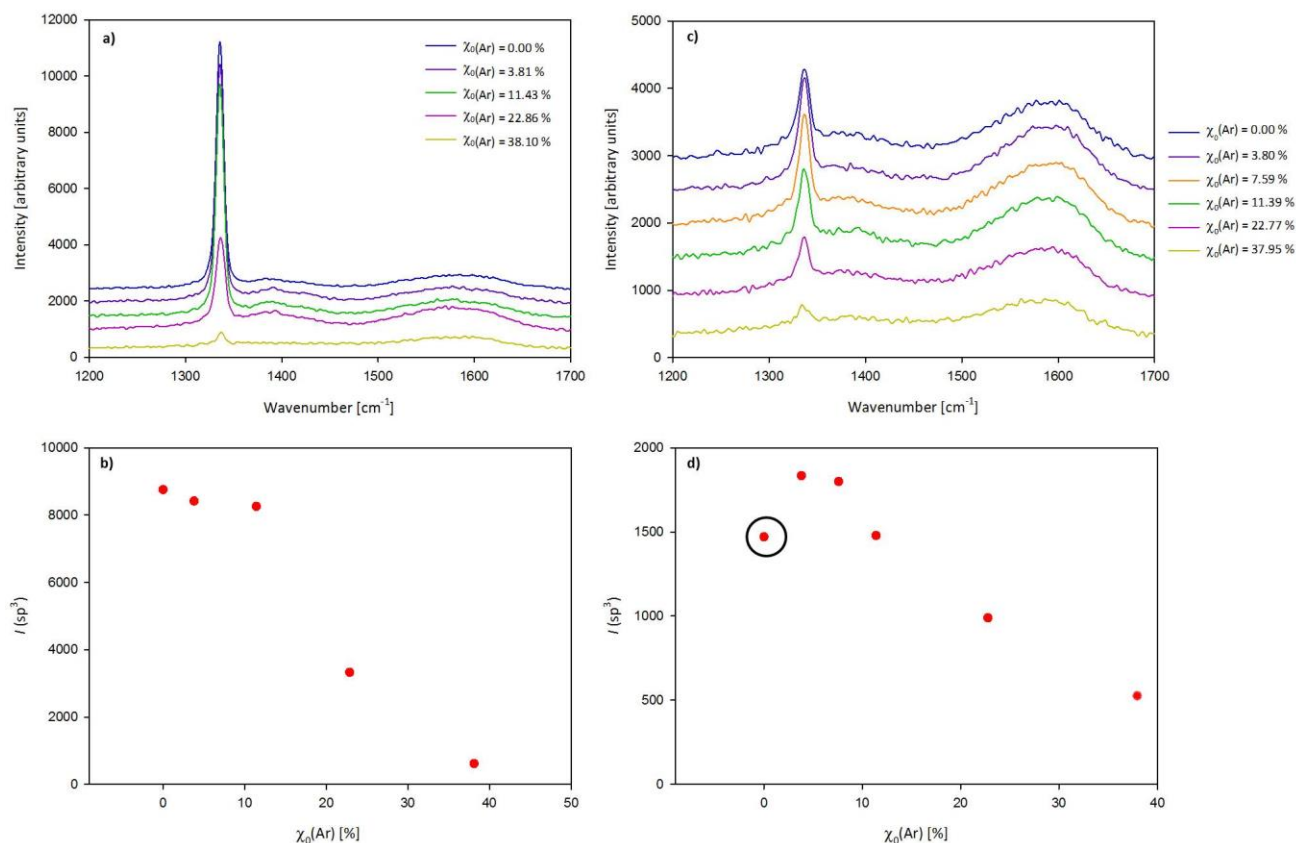


**Figure 57:** a) Stacked UV-Raman spectra of the diamond films grown in the gas mixtures containing no nitrogen and an increasing Ar:H<sub>2</sub> ratio, b) plot of the argon fraction in the input gas mixture against the background-subtracted intensity of the  $sp^3$  peak for the films grown in the gas mixtures containing no nitrogen, c) stacked UV-Raman spectra of the films grown in the gas mixtures containing 0.38 % N<sub>2</sub> and an increasing Ar:H<sub>2</sub> ratio, and d) plot of the argon fraction against the background-subtracted intensity of the  $sp^3$  peak for the films grown in the gas mixtures containing 0.38 % N<sub>2</sub>.

From the UV-Raman spectra in **Fig.57(a)** and (b), it can be seen that increasing the concentration of argon decreases the intensity of the diamond peak at 1332 cm<sup>-1</sup>. This trend is also evident in **Fig.57(c)** and (d), for the case where some N<sub>2</sub> is present, and indicates a decreasing grain size with a transition from microcrystalline to nanocrystalline diamond as the concentration of argon increases. The point circled in **Fig.57(d)** might be expected to be higher than it is and is probably the result of a noisy spectrum so can be considered an anomaly.

The influence of increasing the nitrogen concentration on the diamond film can be analysed by comparing the two sets of Raman spectra. The peaks between 1500 cm<sup>-1</sup> and 1600 cm<sup>-1</sup>

correspond to  $sp^2$  carbon and are more intense in **Fig.57(b)**. There is a decrease in the phase purity of the diamond as the concentration of nitrogen increases and non- $sp^3$ -bonded constituents increase in concentration.

Visible from the optical microscope images is the uniformity of the diamond films and the evident repeatability of the seeding method. The decrease in crystal size of the diamond, as the argon content increases in the absence of nitrogen, can be seen and also the diamond films all grown with nitrogen look different from those grown with no nitrogen. Nothing more conclusive can be derived from the optical microscope pictures.

The SEM images of these samples (**Appendix 14.13**) show a decrease in crystal size with increasing argon content, confirming the conclusion from UV-Raman analysis that there is a transition from microcrystalline to nanocrystalline diamond with increasing argon fraction. This is also a change in the crystalline morphology, with diamond samples grown in the absence of nitrogen having triangular (111) crystallographic facets. A marked difference can then be seen when an argon concentration of 38 % in  $H_2$  is reached. The sides of the crystals are still pyramidal but the top surfaces of the crystals are now (100) square facets as the diamond morphology is transitioning from microcrystalline to nanocrystalline. The images also show an increased surface roughness of the crystals as the argon content increases. This is significant when considering gas mixtures used for growing diamond on the x-ray lens moulds because the surface smoothness is important to minimise lens aberrations. When nitrogen is introduced into the  $H_2/CH_4/Ar$  gas mixture, all the diamond films are nanocrystalline with no triangular facets. Increasing the nitrogen content further does not appear to have much effect on the size of the crystals but it does increase their surface smoothness. An ideal gas mixture for depositing smooth diamond layers would therefore contain a small amount of nitrogen and an argon content of around 10 %. From **Fig.57(c)** and (d) it is apparent that an argon concentration higher than 10 % is where the graph begins to slope downwards more rapidly. This gas mixture would therefore produce nanocrystalline, smooth crystals without sacrificing phase purity.

## **11 Future Work**

The future work will entail generating more nanodiamond refractive lenses that can focus high energy x-rays down to nanosized focal spots. In order to achieve this, lens substrates must be selectively nucleated with a high density, uniform layer of nanodiamond seed particles before the diamond layers are deposited by MWCVD. The self-assembly procedures and resist lift-off methods developed in this project will be applied to new kinoform lens substrates fabricated by Kelvin Nanotechnology. The resultant lenses will be tested on the I13 undulator beamline at the Diamond Light Source, the UK's National Synchrotron Source, in May 2014.

## 12 Conclusions

This project involved carrying out a series of experiments, with a view to improving the method with which structured silicon substrates are seeded, via self-assembly of polymers and nanodiamond particles, in a way that will optimise selected-area nucleation. Application of this procedure to silicon lens-mould substrates, of both CRL and kinoform lens designs, furthered the progress towards the ultimate goal of generating x-ray nanofocusing refractive lenses from polycrystalline diamond.

Since high-density, smooth diamond layers are required for x-ray focusing lenses, the first part of this investigation involved the development of a repeatable self-assembly procedure that produced a dense, uniform diamond layer on  $1 \text{ cm}^2$  silicon substrates. The devised method was also compatible with various resist layers as the lenses are fabricated using a silicon mould transfer process.

To try to further optimise this process, experiments in the way that the polymer layer was applied to the substrate in electrostatic self-assembly were performed, with the conclusion that substrate immersion in the polymer is more effective than spin-coating. The use of the silane molecule, carboxyethylsilanetriol, as an alternative to PDDA and PSS-ND in self-assembly nucleation was also trialled, resulting in a much quicker method that yields both uniform and dense diamond conformal layers. Finally, various nanodiamond solutions were analysed using dynamic light scattering and investigations into the effect of sonication on the average particle size in each solution were implemented. It was found that each solution had an optimum sonication time, after which the average particle size was smallest. Seed layers with a higher nucleation density were achieved when the nanodiamond solution was sonicated before being used in self-assembly.

Once the optimum self-assembly methods had been developed, experiments into how best to remove various resist layers were conducted, in order to improve selected-area nucleation. Successful removal methods for three different resist layers, ma-N2410, UV-III and ma-N415, were achieved through extensive testing of resist-coated silicon substrates. Application to real lens substrates of the ma-N2410 lift-off process then followed and much better selectivity was observed compared with previous work. The use of a buffered oxide etch on silicon oxide-coated silicon samples after a short diamond deposition was investigated as a potential way to achieve selected-area deposition. However, it was found

that this method was not very successful and the resultant selectivity was deemed not good enough to be feasible for use in lens fabrication.

Investigations were undertaken into the use of different materials as growth substrates in diamond MWCVD. Zirconium and titanium proved unsuccessful, whereas freestanding diamond films were produced when SrTiO<sub>3</sub> or AlN were used as substrates. Research was carried out with aluminium nitride, growing a series of films for different lengths of time and under different conditions. The thinnest membrane obtained was around 80 nm in thickness over a large surface area of 1 cm<sup>2</sup>. This work has potential uses in diamond thin membranes. Finally, investigations into the effect of the concentrations of nitrogen and argon added to the H<sub>2</sub>/CH<sub>4</sub> gas mixture used in diamond CVD led to the suggestion of an ideal gas mixture. It was found that increasing the argon concentration in the input gas mixture decreases the diamond crystal size but also increases surface roughness, whilst nanocrystalline diamond always grows if nitrogen is present and surface smoothness increases with increasing nitrogen concentration. Increasing the concentration of both results in a decrease in the intensity of the characteristic diamond peak at 1332 cm<sup>-1</sup> in Raman spectra, indicating a decrease in phase purity and diamond content of the films, particularly above an argon concentration of around 10 %. Smooth, nanocrystalline diamond, without compromising purity, can be obtained if a gas mixture containing a small amount of nitrogen and an argon concentration no higher than 10 % is used.

## 13 References

1. May, P. W., *Phil. Trans. R. Soc. Lond. A*, **358** (2000) 473.
2. Wilks, J., & Wilks, E., *Properties and Applications of Diamond*, Butterworth-Heinemann Ltd (1991) **1**, 8.
3. Harlow, G. E., *The Nature of Diamond*, Cambridge University Press (1998) **13**, 255.
4. Fox, O. J. L., PhD Thesis, University of Bristol (2011).
5. Field, J. E., *The Properties of Natural and Synthetic Diamond*, Academic Press (1992).
6. Berman, R., *Physical Properties of Diamond*, Clarendon Press (1965) **12**, 325.
7. Berman, R., *Physical Properties of Diamond*, Clarendon Press (1965) **9**, 266.
8. Pierson, H. O., *Handbook of Chemical Vapour Deposition*, Elsevier Science (1999) **7**, 172.
9. Wilks, J., & Wilks, E., *Properties and Applications of Diamond*, Butterworth-Heinemann Ltd (1991) **1**, 28.
10. Wu, B. R., & Xu, J., *J. Phys. Rev. B.*, **57** (1998) 13355.
11. Bundy, F. P., *J. Geophys. Res.*, **85** (1980) 6930.
12. Celii, F. G., & Butler, J. E., *Annu. Rev. Phys. Chem.*, **42** (1991) 643.
13. Wilks, J., & Wilks, E., *Properties and Applications of Diamond*, Butterworth-Heinemann Ltd (1991) **5**, 108.
14. [www.cleanroom.byu.edu/EW\\_orientation.phtml](http://www.cleanroom.byu.edu/EW_orientation.phtml)
15. Kobashi, K., Nishimura, K., Kawate, Y., & Horiuchi, T., *Phys. Rev. B.*, **38** (1988) 4067.
16. Kobashi, K., Nishimura, K., Kawate, Y., & Horiuchi, T., *J. Vac. Sci. Technol. A.*, **6** (1988) 1816
17. Williams, B. E., & Glass, J. T., *J. Mater. Res.*, **4** (1989) 373.
18. Govindaraju, N., Das, D., Kosel, P. B., & Singh, R. N., *ECS Transactions*, **33** (2010) 155.
19. Gruen, D. M., Shenderova, O. A., & Vul', A. Y., *Synthesis, Properties and Applications of Ultrananocrystalline Diamond*, Springer (2005) **4**, 39.
20. Spear, K. E., & Dismukes, J. P., *Synthetic Diamond*, Wiley (1994) **6**, 148.
21. Butler, J. E., & Woodin, R. L., *Phil. Trans. R. Soc. Lond. A.*, **342** (1993) 209.
22. Choi, H. W., Gu, E., Liu, C., Griffin, C., Girkin, J. M., Watson, I. M., & Dawson, M. D., *J Vac Sci Technol B Nanotechnol Microelectron*, **23** (2005) 130.

23. Fox, O. J. L., Alianelli, L., Malik, A. M., Pape, I., May, P. W., & Sawhney, K. J. S, *Opt. Express*, accepted 2013.
24. Alianelli, L., Sawhney, K. J. S., Malik, A., Fox, O. J. L., May, P. W., Stevens, R., Loader, I. M., & Wilson, M. C., *J. Appl. Phys*, **108** (2010) 123107.
25. Nöhammer, B., Hoszowska, J., Freund, A. K., & David, C., *J. Synchrotron. Radiat.* **10** (2003) 168.
26. Evans-Lutterodt, K., Ablett, J. M., Stein, A., & Kao, C., *Opt. Express*, **11** (2003) 919.
27. Margaritondo, G., *Introduction to Synchrotron Radiation*, Oxford University Press, Inc. (1988) **2**, 9.
28. [www.diamond.ac.uk](http://www.diamond.ac.uk)
29. Elleaume, P., *Nucl. Instrum. Meth. A.*, **412** (1998) 483.
30. Lengeler, B., Schroer, C., Tümmler, J., Benner, B., Richwin, M., Snigirev, A., Snigireva, I., & Drakopoulos, M., *J. Synchrotron. Rad.*, **6** (1999) 1153.
31. Isakovic, A. F., Stein, A., Warren, J. B., Narayanan, S., Sprung, M., Sandy, A. R., & Evans-Lutterodt, K., *J. Synchrotron. Rad.*, **16** (2009) 8.
32. Snigirev, A., Kohn, V., Snigireva, I., & Lengeler, B., *Nature*, **384** (1996) 49.
33. Alianelli, L., Sawhney, K. J. S., Malik, A., Fox, O. J. L., May, P. W., Stevens, R., Loader, I. M., & Wilson, M. C., *J. Appl. Phys*, **108** (2010) 123107.
34. <http://www.spts.com/banners/1000th-DRIE-module-sold>
35. Dalsa Semiconductor Inc., (2009), *Deep Reactive Ion Etching*, Canada, Patent Number: 20090242512. Downloaded from: <http://www.faqs.org/patents/app/20090242512>
36. Plasmatherm, *MEMS and Sensors Whitepaper Series*, (2012).
37. Oxford Instruments, *Comparison of the Bosch and Cryogenically Cooled Deep Silicon Etch Processes*, (2012).
38. Defforge, T., Song, X., Gautier, G., Tillocher, T., Dussart, R., Kouassi, S., & Tran-Van, F., *Sens. Actuators A*, **170** (2011) 114.
39. Oxford Instruments, *Deep Silicon Etch Applications in MEMS and NEMS*, (2013).
40. Hynes, A.M., Ashraf, H., Bhardwaj, J. K., Hopkins, J., Johnston, I., & Shepherd, J. N., *Sens. Actuat. A-Phys.*, **74** (1999) 13.
41. Srinivasan. S., Johnson, D., Lishan, D., Westerman, R., & Lai, S., *Notch Reduction in Silicon on Insulator (SOI) Structures using a Time Division Multiplex Etch Process.*

42. Owen, K. J., VanDerElzen, B., Peterson, R. L., & Najafi, K., *MEMS*, **12** (2012) 251.
43. <http://www.spts.com/products/plasma-etch/si-drie>
44. <http://www.spts.com/Banners/Morflex/Morflex.aspx>
45. Plasma-Therm, (2002), *Morphed processing of semiconductor devices*, USA, USA  
Patent Number: 6417013. Downloaded from:  
<http://www.docstoc.com/docs/51350557/Morphed-Processing-Of-Semiconductor-Devices---Patent-6417013>
46. Plasma-Therm, (2000), *Etching process for producing substantially undercut free silicon on insulator structures*, USA, 6071822. Downloaded from:  
<http://www.google.nl/patents/US6071822>
47. <http://www.oxfordplasma.de/systems/estrelas.htm>
48. <http://www.businesswire.com/news/home/20060616005548/en/Unaxis-Wafer-Processing-Awarded-10-Ranking-Seventh>
49. <http://www.southampton-nanofab.com/>
50. [http://www.kelvinnanotechnology.com/products/products\\_imprint\\_templates.html](http://www.kelvinnanotechnology.com/products/products_imprint_templates.html)
51. Ando, Y., Nishibayashi, Y., Kobashi, K., Hirao, T., & Oura, K., *Diam. Relat. Mater*, **11** (2002) 824.
52. Moldovan, N., Divan, R., Zeng, H., & Carlisle, J. A., *J. Vac. Sci. Technol., B*, **27** (2009) 3125.
53. Yamada, T., Yoshikawa, H., Uetsuka, H., Kumaragurubaran, S., Tokuda, N., & Shikata, S., *Diam. Relat. Mater.*, **16** (2007) 996.
54. Ding, G. F., Mao, H. P., Cai, Y. L., Zhang, Y. H., Yao, X., & Zhao, X. L., *Diam. Relat. Mater*, **14** (2005) 1543.
55. [www.thindiamond.com](http://www.thindiamond.com)
56. <http://www.oxford-instruments.com/products/etching-deposition-and-growth/processes/etching-processes/organics/diamond-etch>
57. Artyukhin, A., Bakajin, O., Stroeve, P., & Noy, A., *Langmuir*, **20** (2004) 1442.
58. Zhang, X., Chen, H., & Zhang, H., *Chem. Commun.*, (2007) 1395.
59. Kim, J. H., Lee, S. K., Kwon, O.M., & Lim, D. S., *J. Nanosci. Nanotechno.*, **9** (2009) 4121.
60. Tofts, E., MSci Thesis, (2012).

61. Masood, A., Aslam, M., Tamer, M. A., & Potter, T. J., *J. Electrochem. Soc.*, **138** (1991) 67.
62. Albin, S., Williams, F. R., Zhou, X., & Xiao, W., *Compos. Interfaces*, **19** (2012) 179.
63. Ha, S. C., Kang, D. H., Kim, K. B., Min, S. H., Kim, I. H., & Lee, J. D., *Thin Solid Films*, **341** (1999) 216.
64. Lessel, M., Bäumchen, O., Klos, M., Hähl, H., Fetzner, R., Seemann, R., & Jacobs, K., Dept. Exp. Phys., Saarland University (2012) .
65. Kessel, C. R., & Granick, S., *Langmuir*, **7** (1991) 532.
66. Haensch, C., Hoepfner, S., & Schubert, U., *Chem. Soc. Rev.*, **39** (2010) 2323.
67. Ulman, A., *Chem. Rev.*, **96** (1996) 1533.
68. Jalali, H., BSc Thesis (2005).
69. Banga, R., Yarwood, J., Morgan, A. M., Evans, B., & Kells, J., *Langmuir*, **11** (1995) 4393.
70. CRC Handbook of Chemistry and Physics, 94<sup>th</sup> Edition, **12** (2013) 206.
71. Kriele, A., Williams, O. A., Wolfer, M., Brink, D., Müller-Seibert, W., & Nebel, C. E., *Appl. Phys. Lett.*, **95** (2009) 031905.
72. Barnard, A. S., *J. Mater. Chem.*, **18** (2008) 4038.
73. Proksche, H., Nagorsen, G., & Ross, D., *J. Electrochem. Soc.*, **139** (1992) 521.

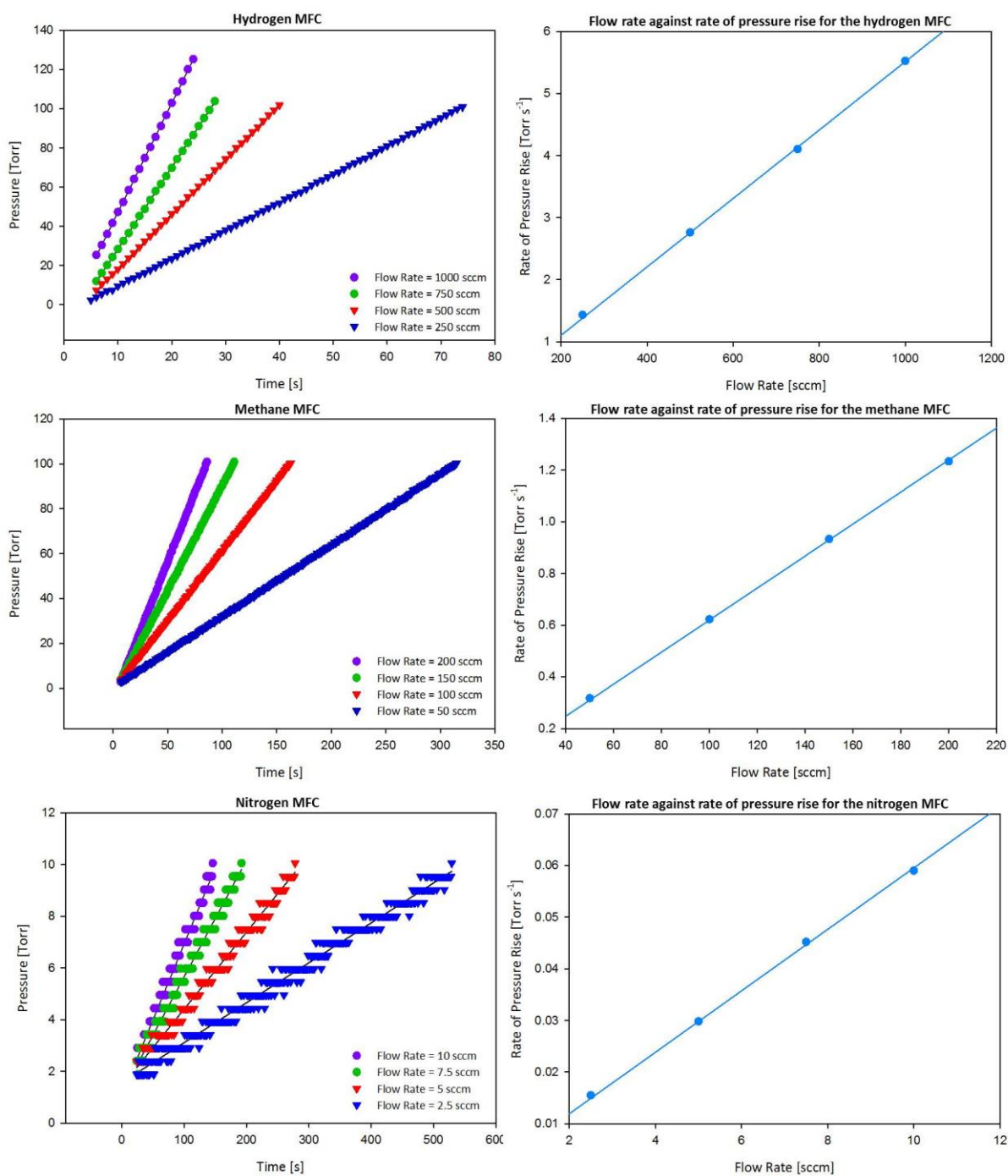


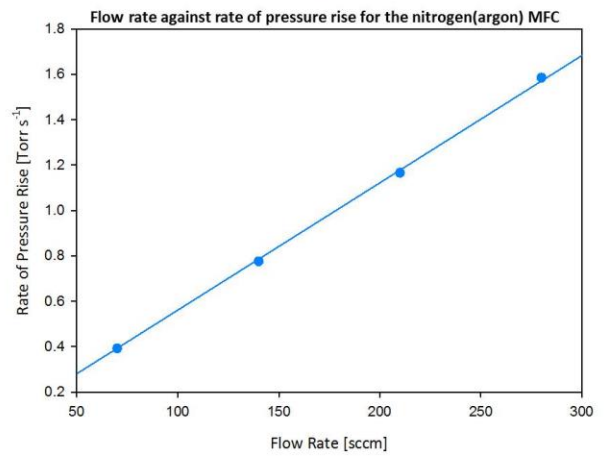
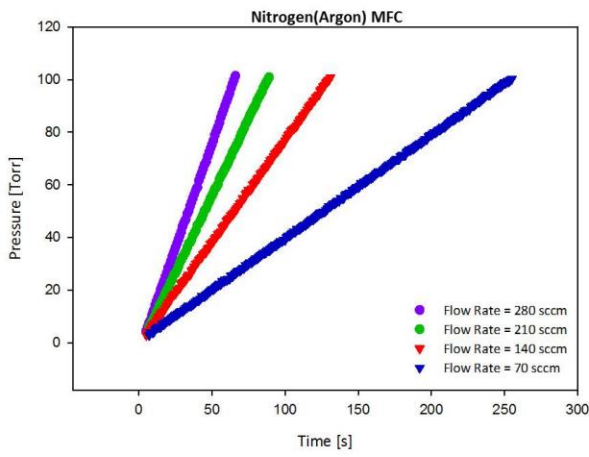
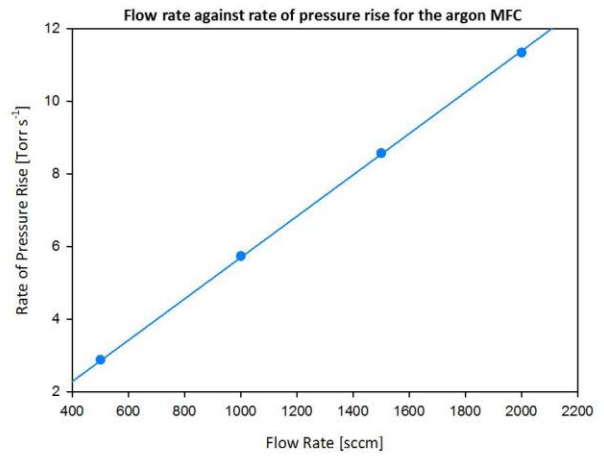
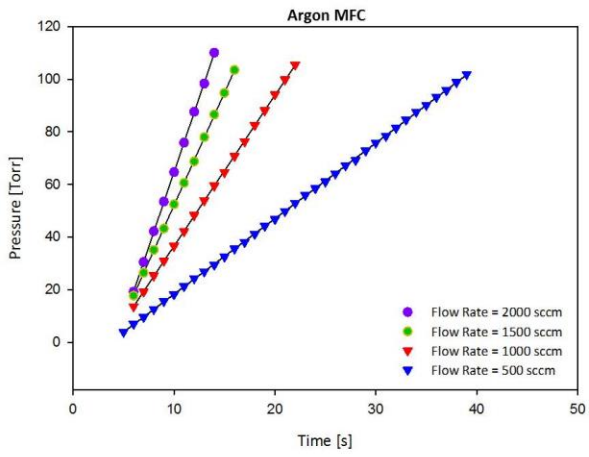




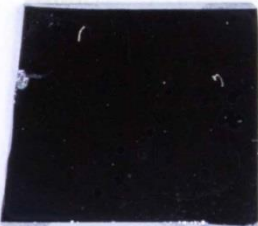


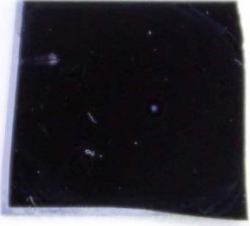
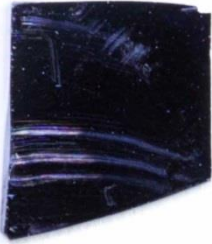
## 14.2 MFC Calibration Graphs



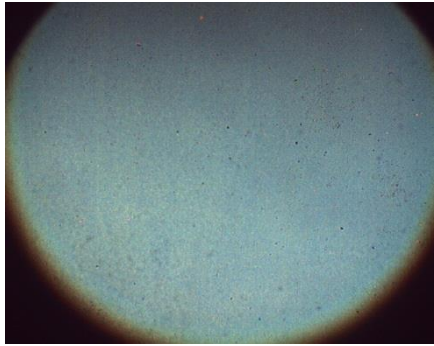
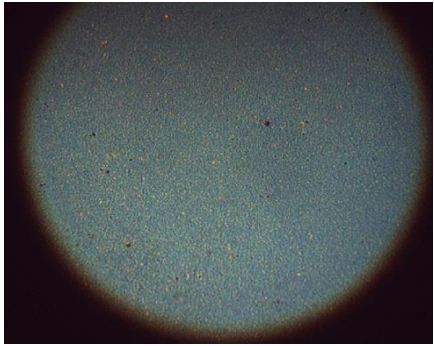
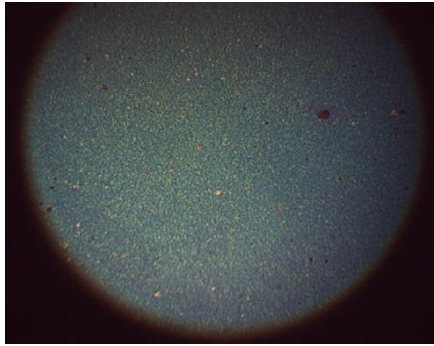
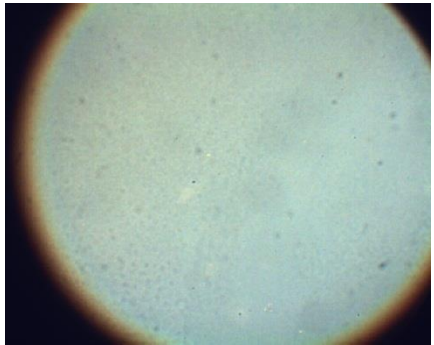
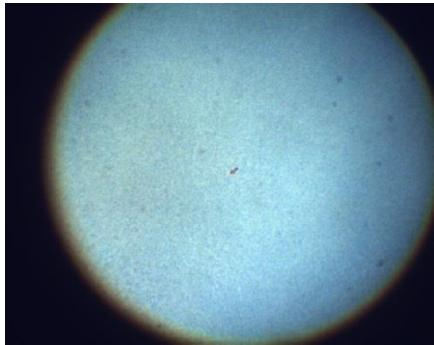


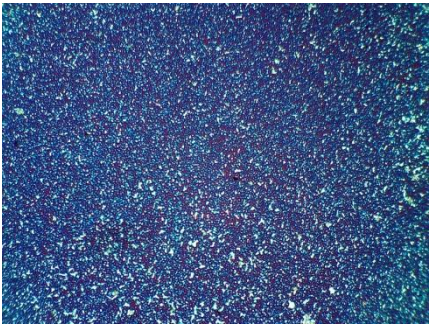
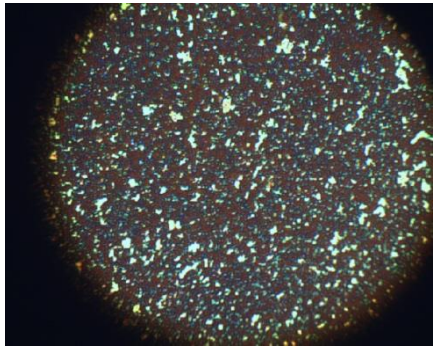
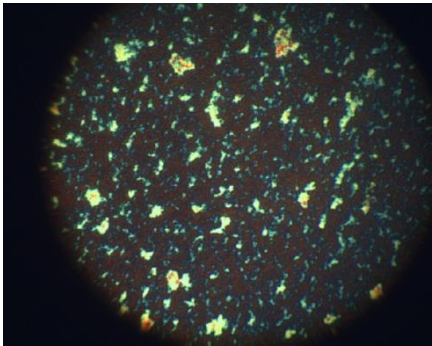
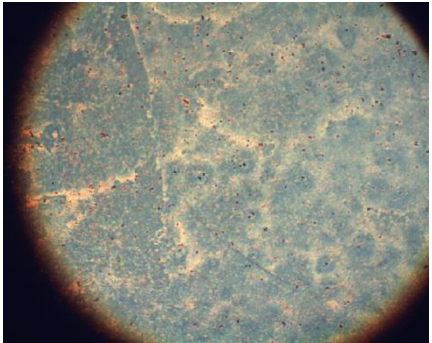
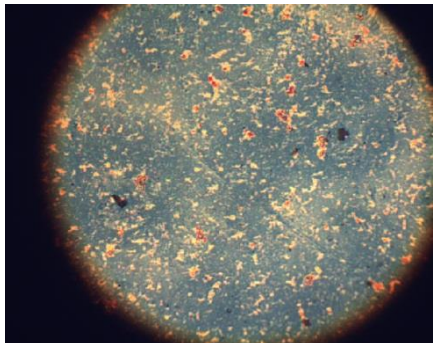
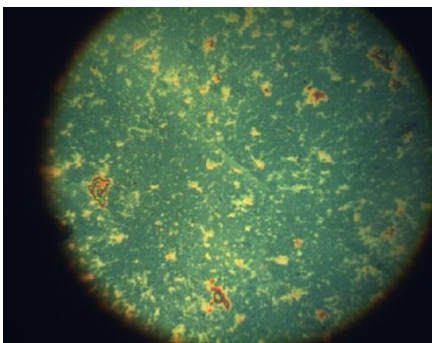
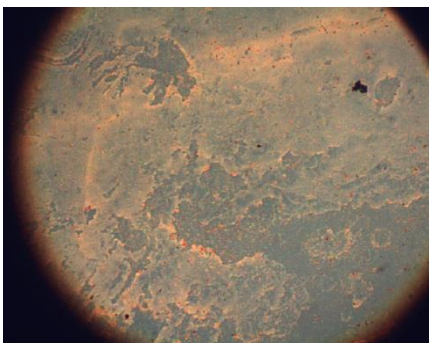
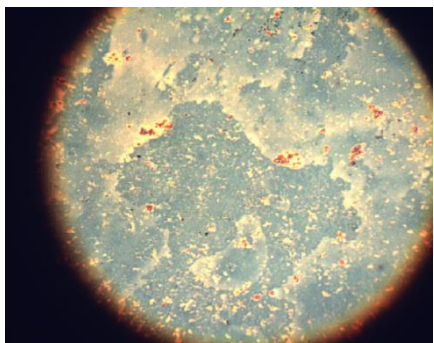
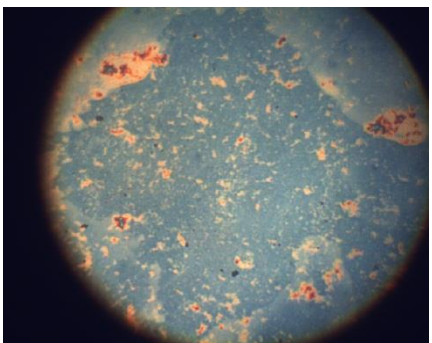
### 14.3 Photographs from the spin-coating experiments

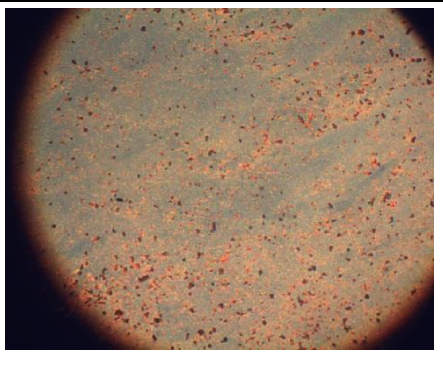
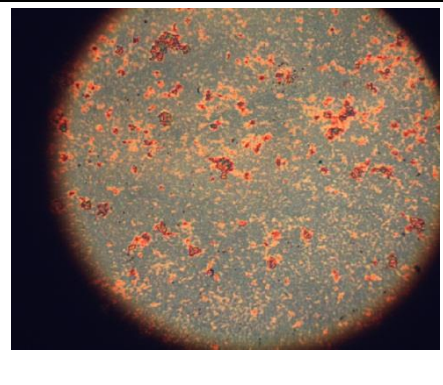
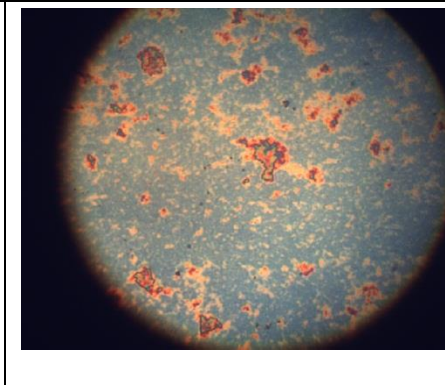
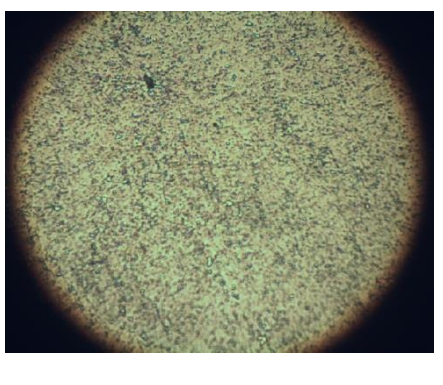
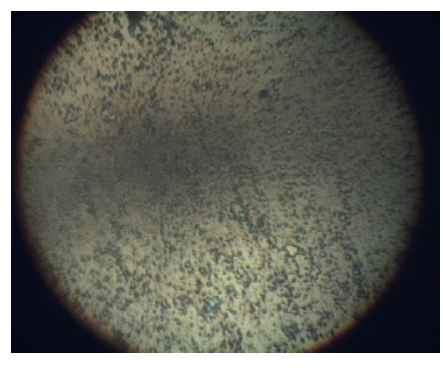
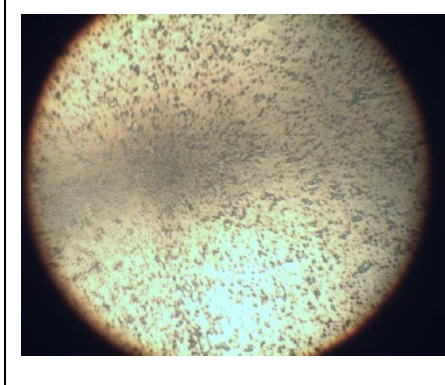
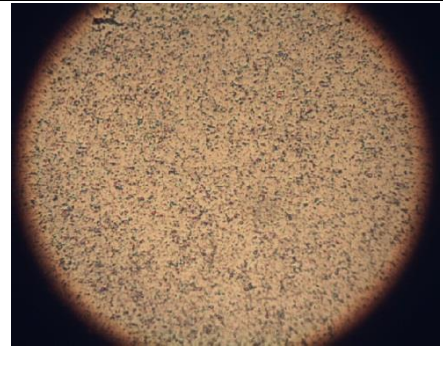
	After spin-coating with PDDA	After seeding with PSS-ND	After 15 min MCD
<p><b>Sample1</b></p> <p>Spin rate: 3000 revolutions per minute (rpm)            Acceleration: 500 rpm s<sup>-1</sup>            Spin time: 1 min</p>			
<p><b>Sample2</b></p> <p>Spin rate: 5000 rpm            Acceleration: 500 rpm s<sup>-1</sup>            Spin time: 1 min</p>			
<p><b>Sample3</b></p> <p>Spin rate: 7000 rpm            Acceleration: 1000 rpm s<sup>-1</sup>            Spin time: 1 min</p>			
<p><b>Sample4</b></p> <p>Spin rate: 7000 rpm            Acceleration: 1000 rpm s<sup>-1</sup>            Spin time: 1 min</p>			

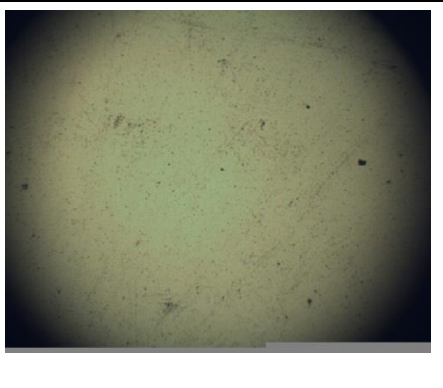
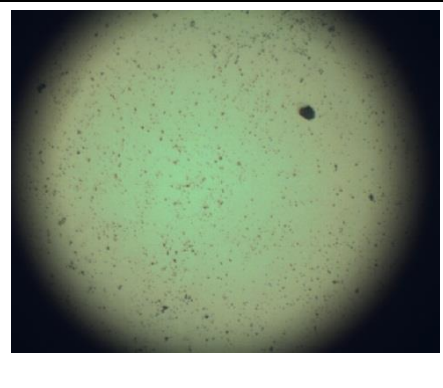
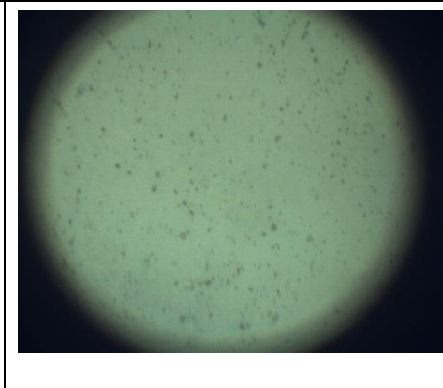
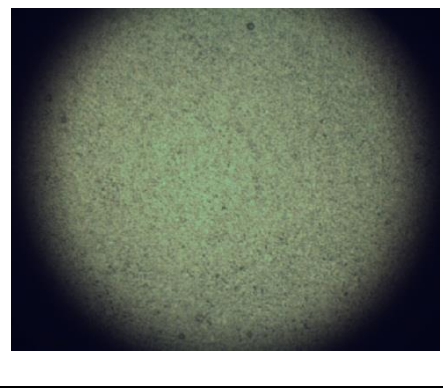
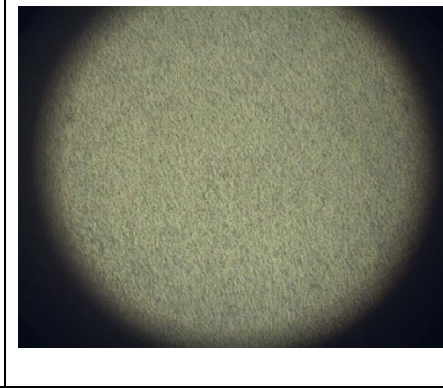
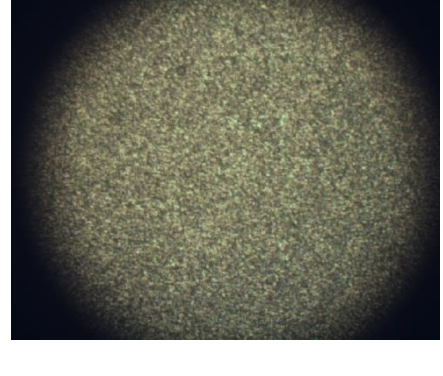
<p><b>Sample5</b></p> <p><b>Spin rate: 5000 rpm</b>  <b>Acceleration: 1000 rpm s<sup>-1</sup></b>  <b>Spin time: 1 min</b></p>			
<p><b>Sample6</b></p> <p><b>Spin rate: 9000 rpm</b>  <b>Acceleration: 1000 rpm s<sup>-1</sup></b>  <b>Spin time: 1 min</b></p>			
<p><b>Sample7</b></p> <p><b>Spin rate: 7000 rpm</b>  <b>Acceleration: 300 rpm s<sup>-1</sup></b>  <b>Spin time: 1 min</b></p>			
<p><b>Sample8</b></p> <p><b>Spin rate: 7000 rpm</b>  <b>Acceleration: 500 rpm s<sup>-1</sup></b>  <b>Spin time: 1 min</b></p>			
<p><b>Sample9</b></p> <p><b>Spin rate: 6000 rpm</b>  <b>Acceleration: 500 rpm s<sup>-1</sup></b>  <b>Spin time: 1 min</b></p>			

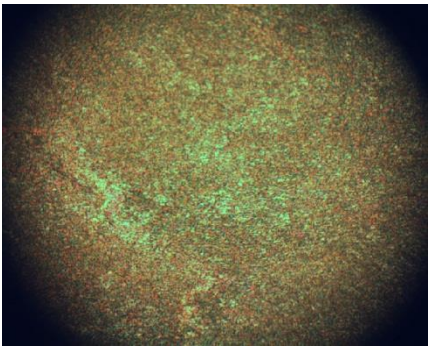
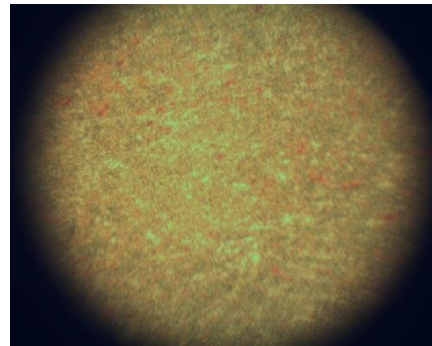
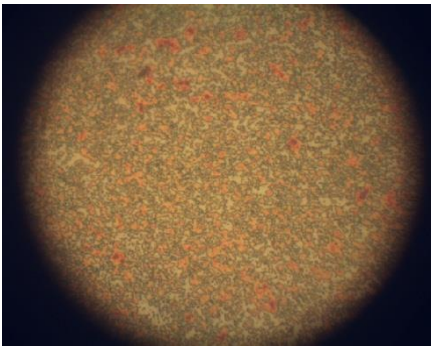
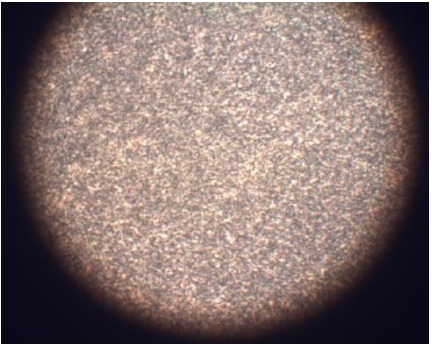
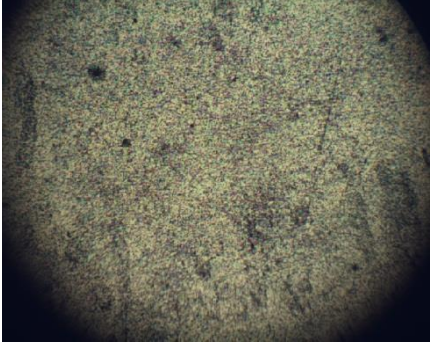
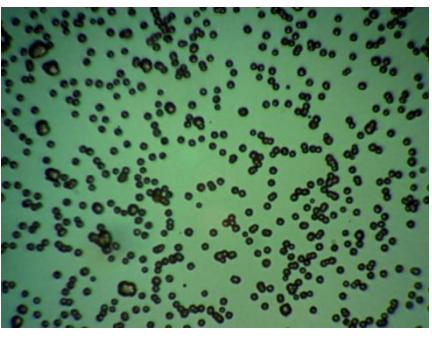
#### 14.4 Optical microscope images of the diamond films grown in the investigation of CEST self-assembly

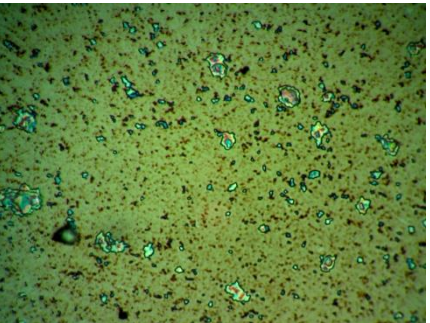
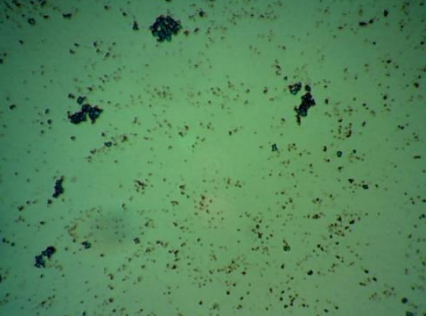
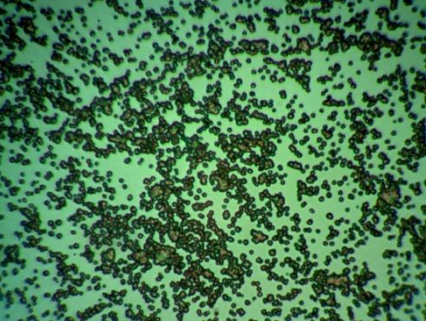
Sample Name	×10	×50	×100
<b>CEST(Trial)</b> <b>10 w/v % ND in DI</b> <b>5 min NCD</b>			
<b>CEST(Trial2)</b> <b>10 w/v % ND in DI</b> <b>2.5 min NCD</b>			

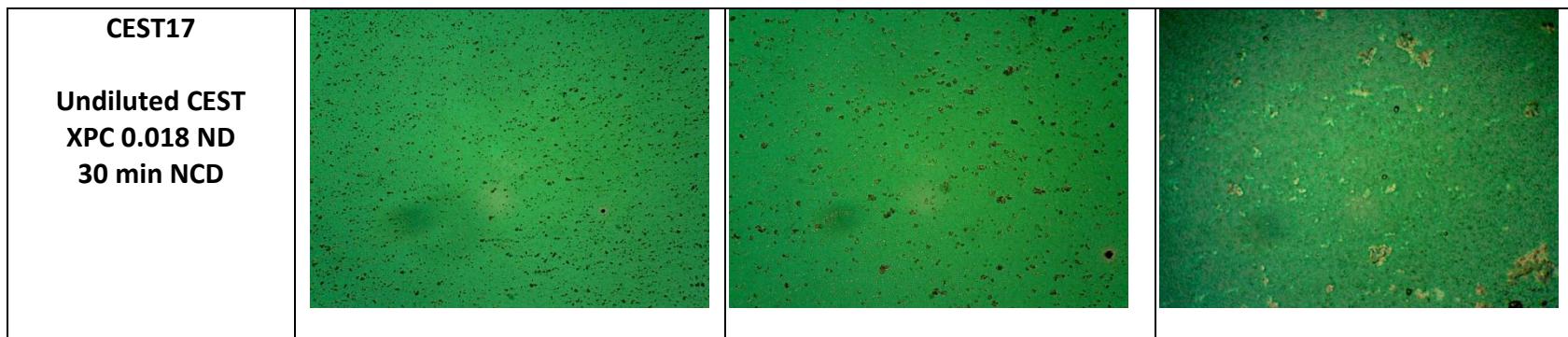
<p><b>CEST1</b></p> <p><b>Undiluted CEST</b>  <b>10 w/v % ND in DI</b>  <b>2.5 min MCD</b></p>			
<p><b>CEST2</b></p> <p><b>Undiluted CEST</b>  <b>5 w/v % ND in DI</b>  <b>2.5 min NCD</b></p>			
<p><b>CEST3</b></p> <p><b>Undiluted CEST</b>  <b>2.5 w/v % ND in DI</b>  <b>2.5 min NCD</b></p>			

<p><b>CEST4</b></p> <p>50 w/v % CEST in DI 10 w/v % ND in DI 2.5 min NCD</p>			
<p><b>CEST5</b></p> <p>Undiluted CEST 10 w/v % ND in DI 2.5 min MCD (25 sccm CH<sub>4</sub>)</p>			
<p><b>CEST6</b></p> <p>Undiluted CEST 10 w/v % ND in DI 2.5 min MCD (15 sccm CH<sub>4</sub>)</p>			

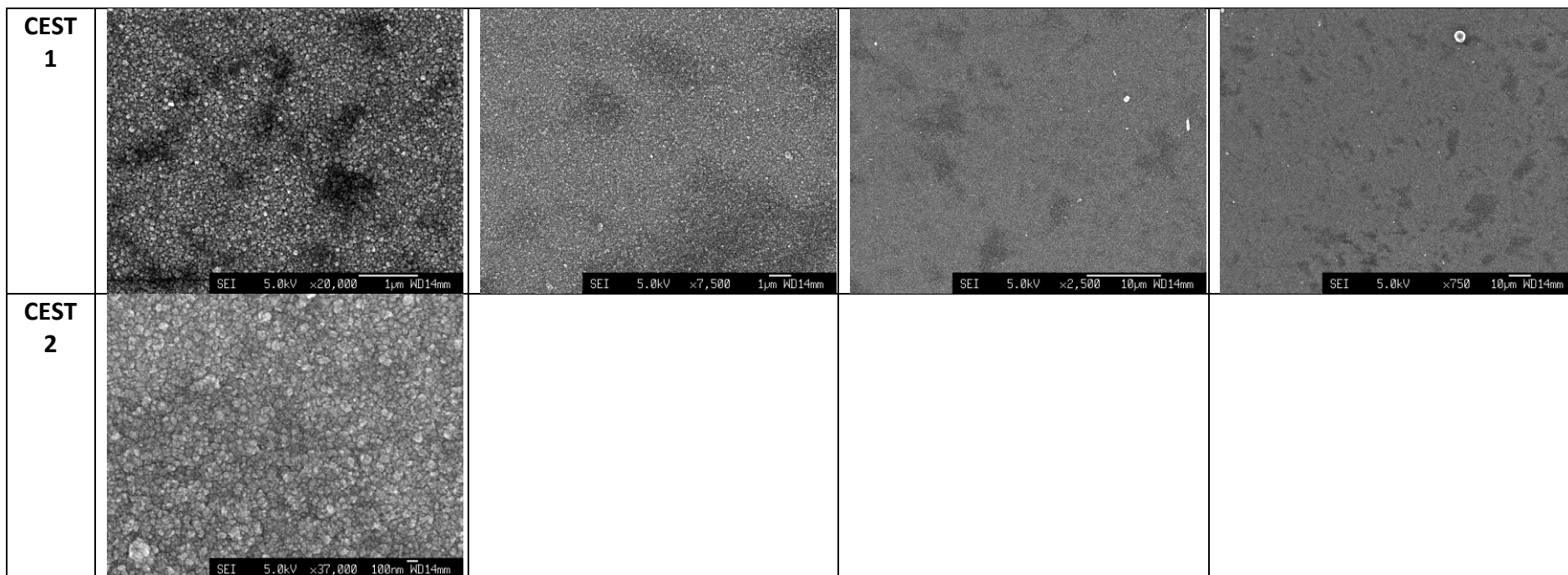
<p><b>CEST7</b></p> <p><b>Premixed undiluted CEST and 10 w/v % ND in DI 2.5 min NCD</b></p>			
<p><b>CEST8</b></p> <p><b>Undiluted CEST 10 w/v % ND in DI 60 min NCD</b></p>			
<p><b>CEST9</b></p> <p><b>Undiluted CEST 10 w/v % ND in DI 60 min MCD</b></p>			

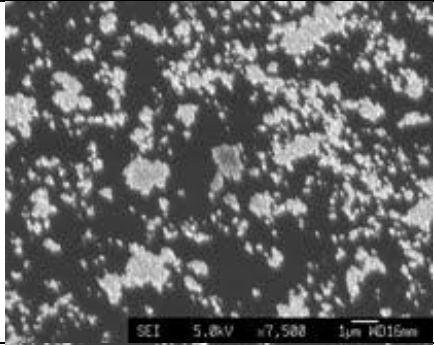
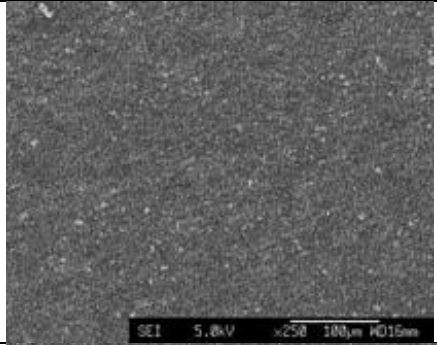
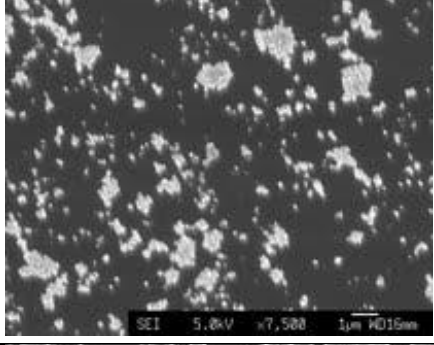
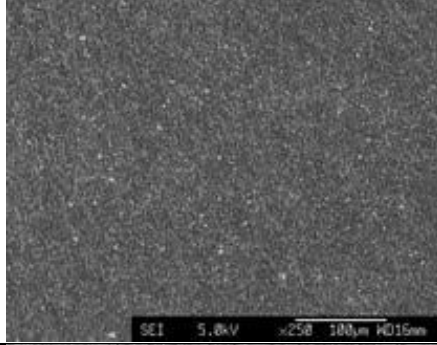
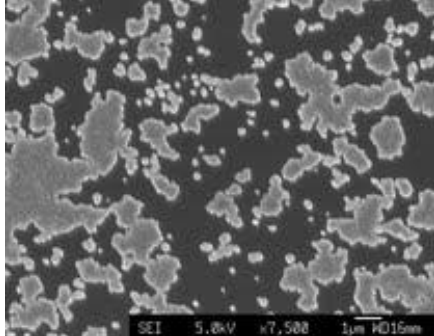
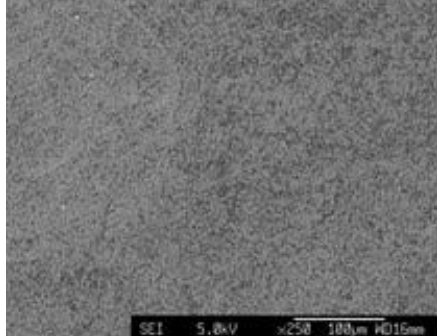
<p><b>CEST10</b></p> <p>50 w/v % CEST in DI  10 w/v % ND in DI  2.5 min NCD  (Repeat of CEST4)</p>			
<p><b>CEST12</b></p> <p>Undiluted CEST  XPC 0.018 ND  30 min MCD</p>			
<p><b>CEST13</b></p> <p>Undiluted CEST  50 w/v % in DI XPC  0.018 ND  30 min NCD</p>			

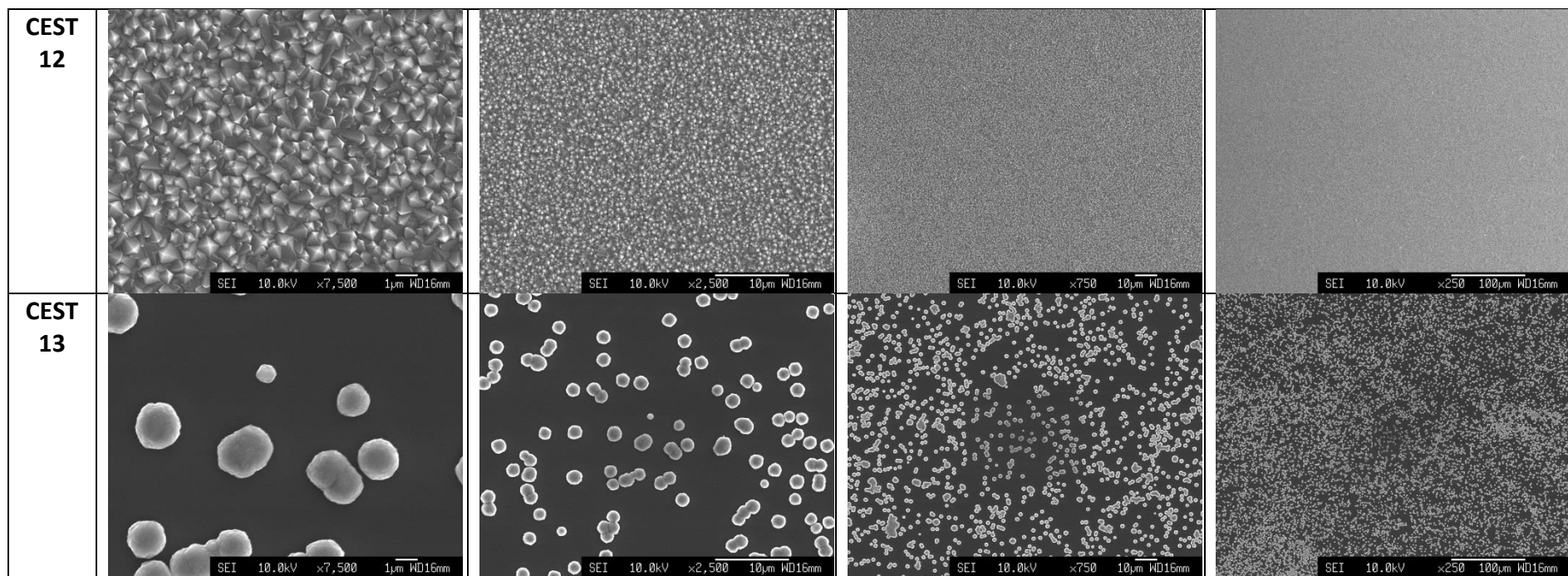
Seeded with new ND Solutions	×5	×10	×100
<b>CEST14</b>  <b>Undiluted CEST</b> <b>XPC 0.018 ND</b> <b>2.5 min MCD</b>			
<b>CEST15</b>  <b>Undiluted CEST</b> <b>50 w/v % in DI XPC</b> <b>0.018 ND</b> <b>2.5 min MCD</b>			
<b>CEST16</b>  <b>Undiluted CEST</b> <b>50 w/v % in DI XPC</b> <b>0.018 ND</b> <b>30 min MCD</b>			



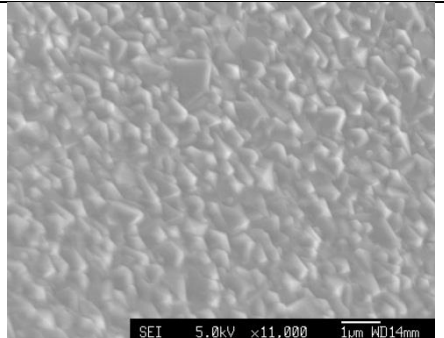
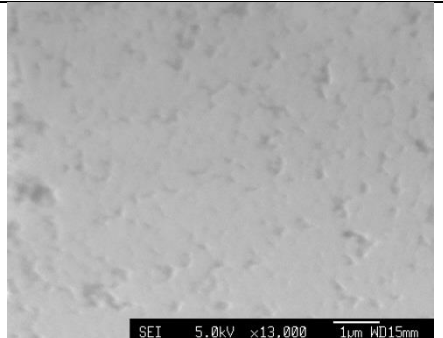
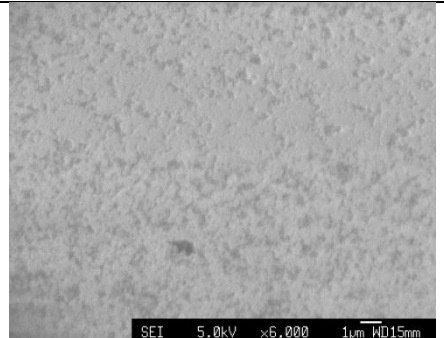
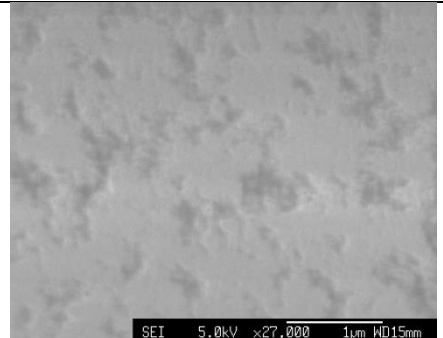
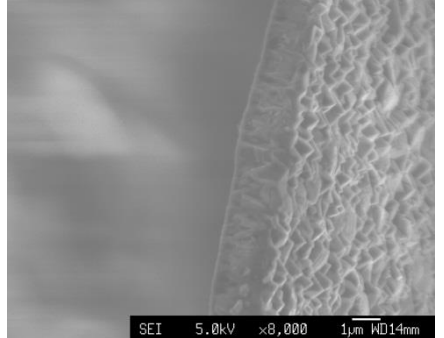
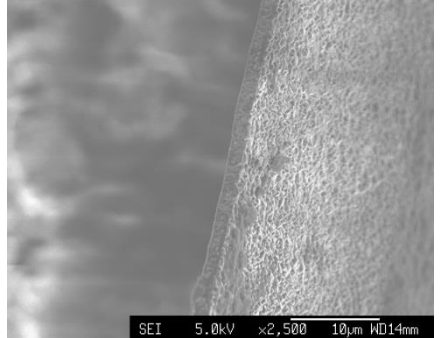
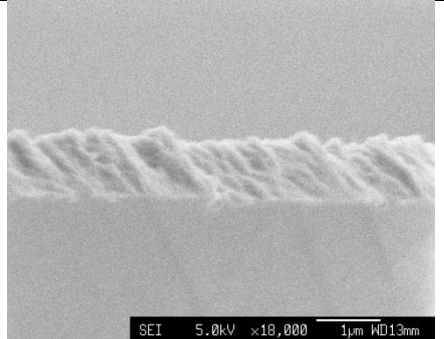
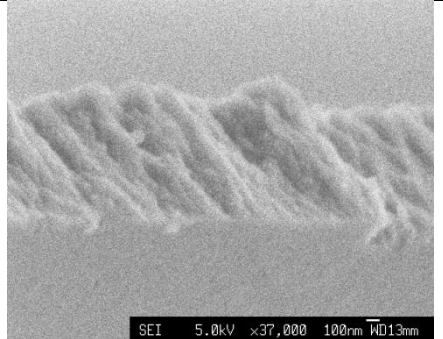
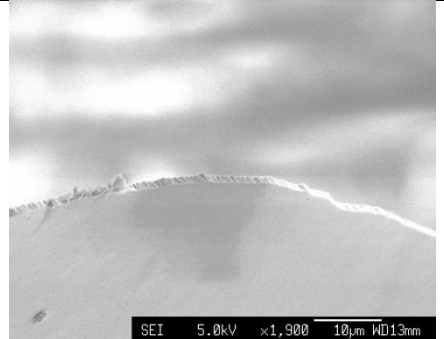
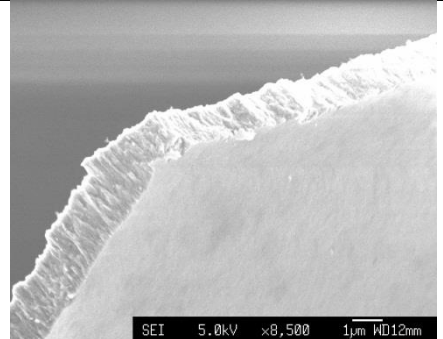
**14.5 SEM images taken of diamond films grown on CEST-seeded silicon substrates**

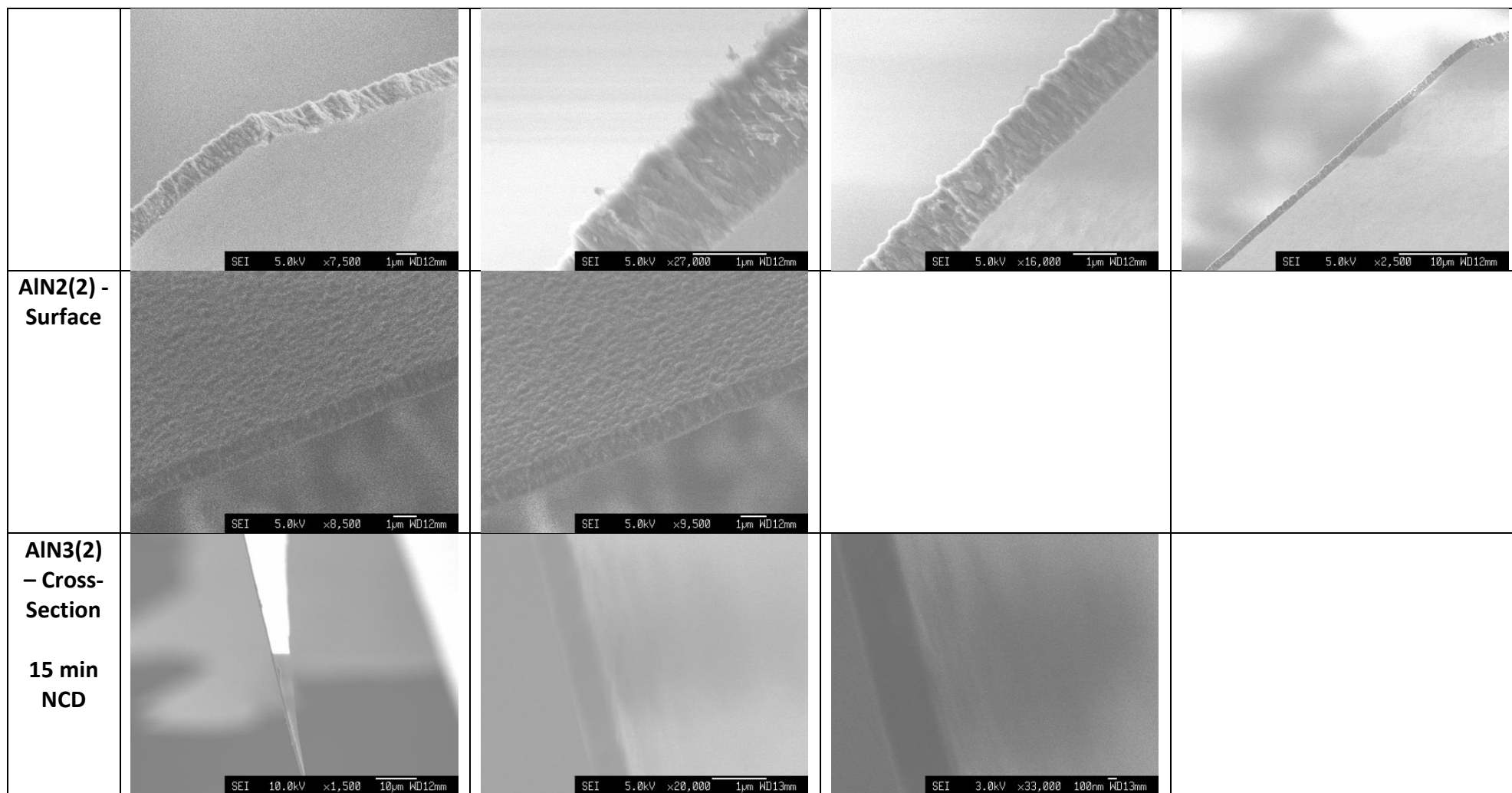


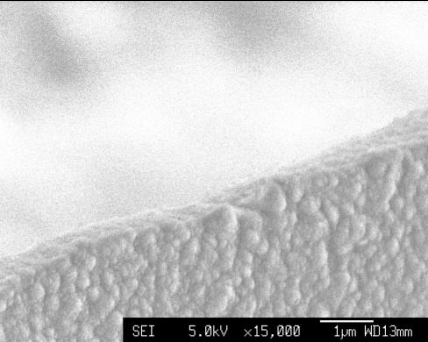
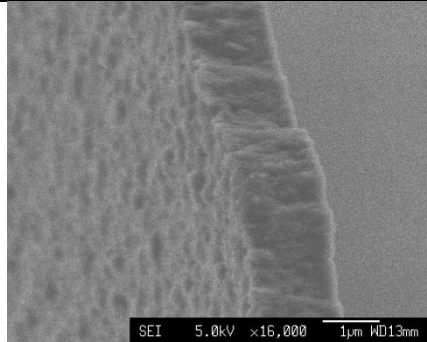
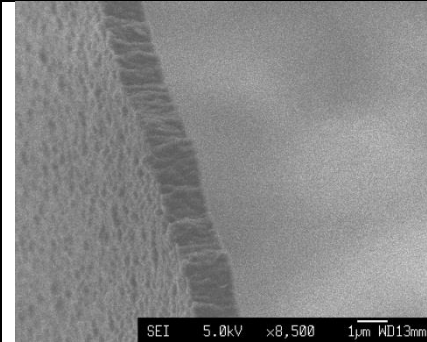
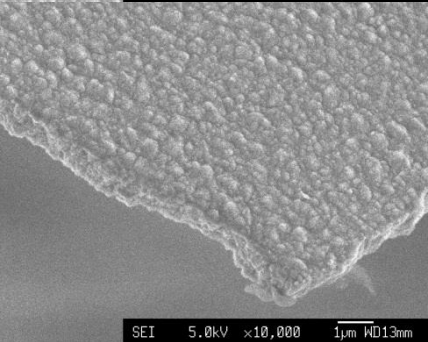
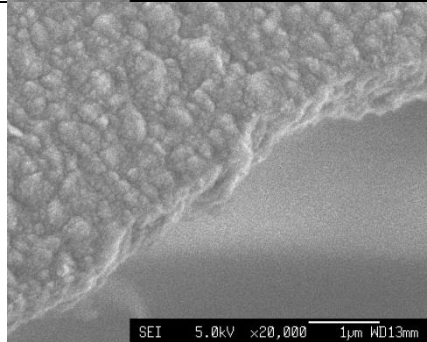
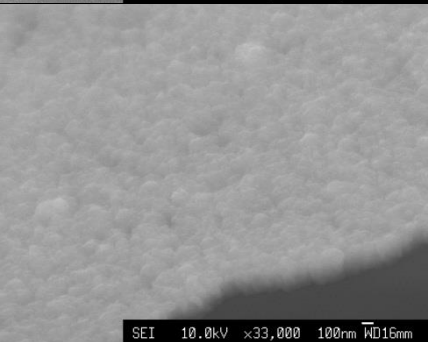
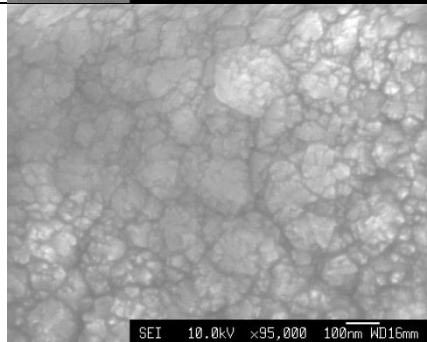
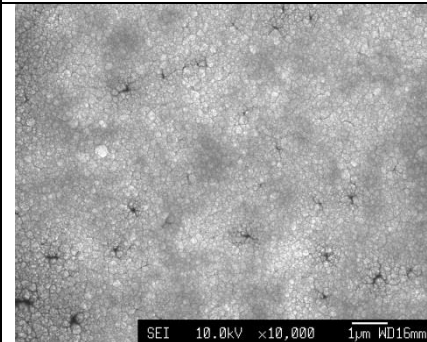
<p><b>CEST 5</b></p>				
<p><b>CEST 6</b></p>				
<p><b>CEST 10</b></p>				

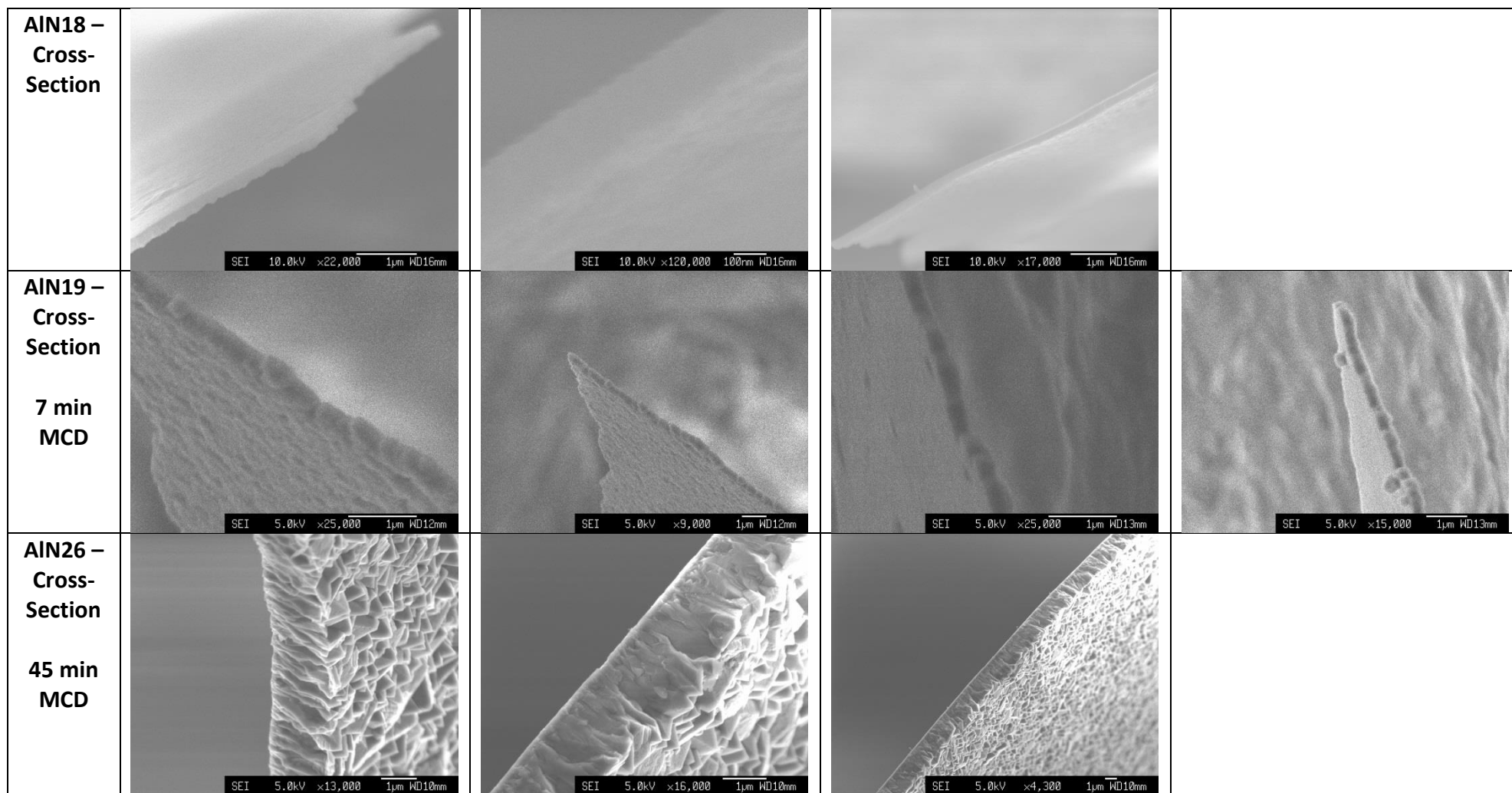


### 14.6 SEM images freestanding diamond films grown on AlN

<p><b>AlN1(2)</b> – <b>Surface</b></p> <p><b>30 min</b> <b>MCD</b></p>				
<p><b>AlN1(2)</b> – <b>Cross-Section</b></p>				
<p><b>AlN2(2)</b> – <b>Cross-Section</b></p> <p><b>30 min</b> <b>NCD</b></p>				

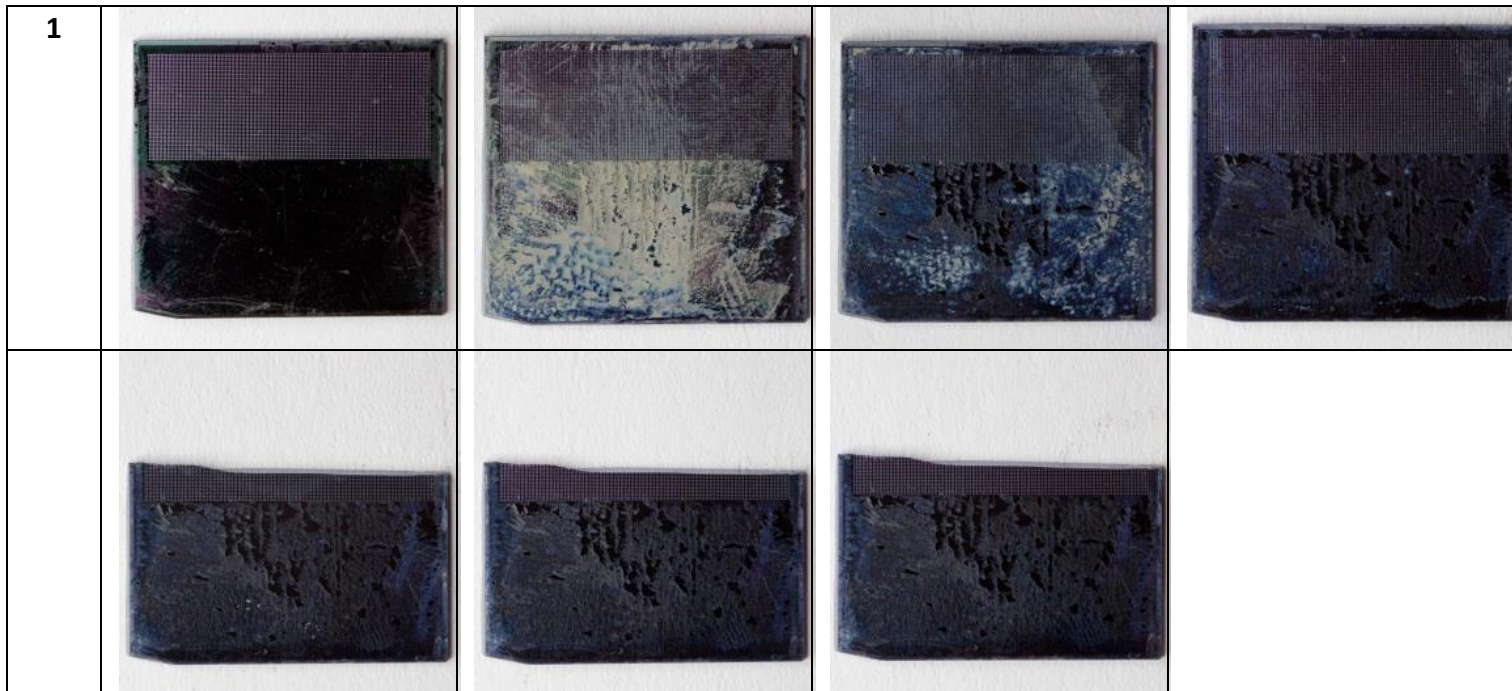


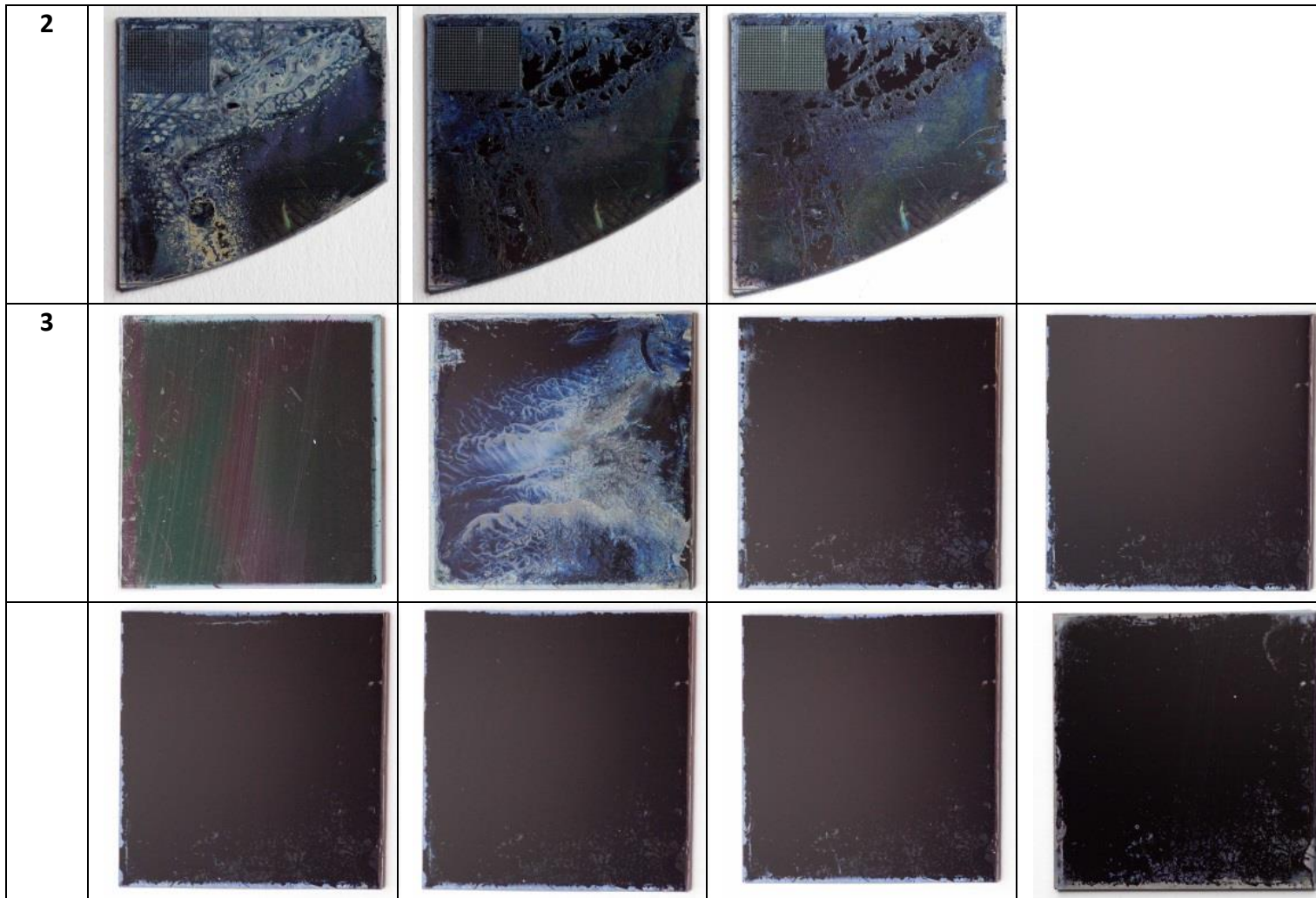
<p><b>AIN5 – Cross- Section</b></p> <p><b>45 min NCD</b></p>				
<p><b>AIN5 - Surface</b></p>				
<p><b>AIN18 – Surface</b></p> <p><b>7 min NCD</b></p>				

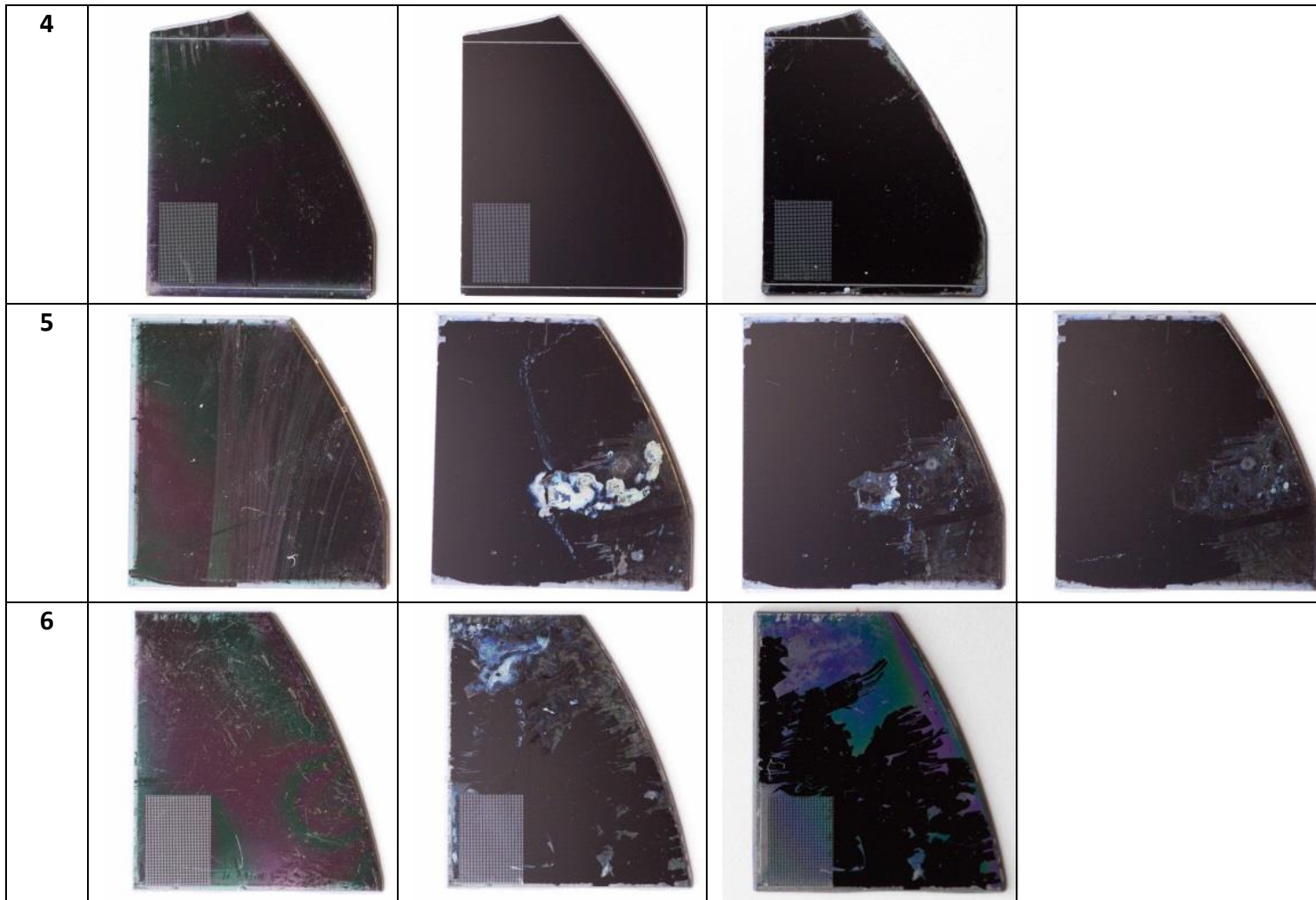


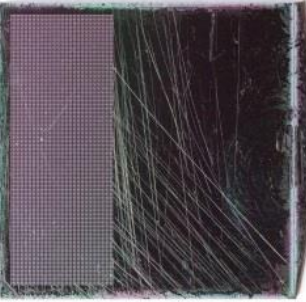
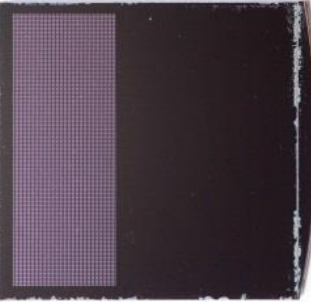
## 14.7 Resist testing photographs

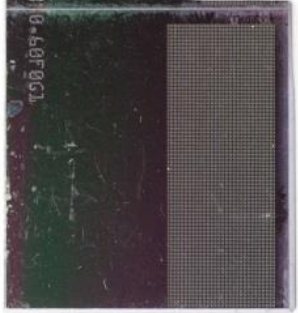
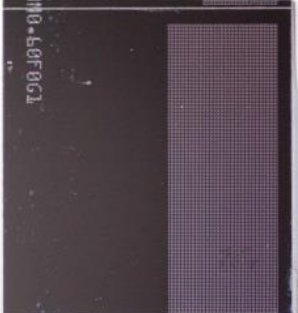
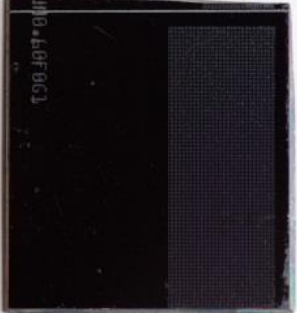
ma-N2410

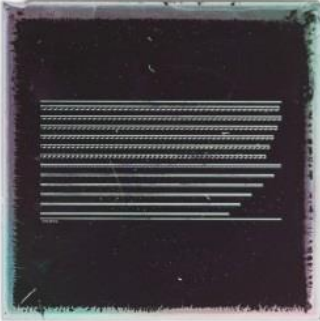
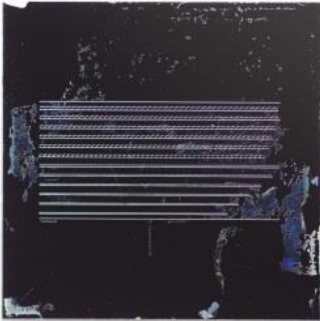
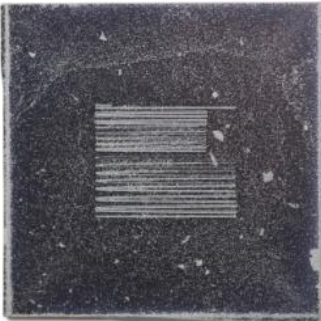




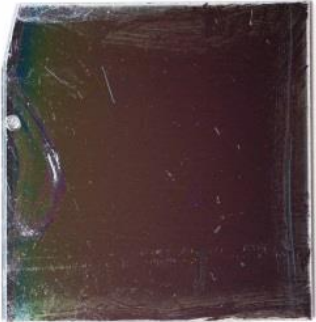


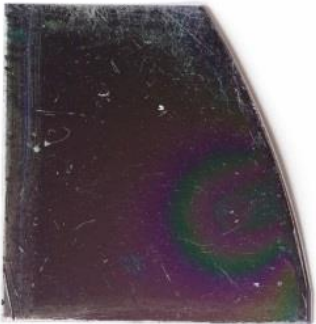
7				
8				
9				

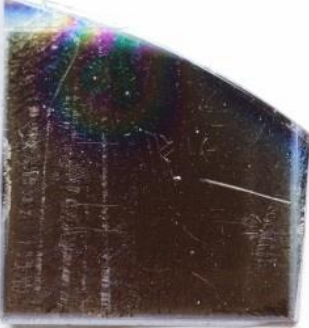
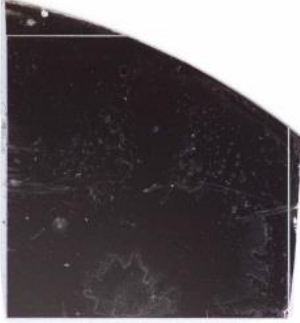
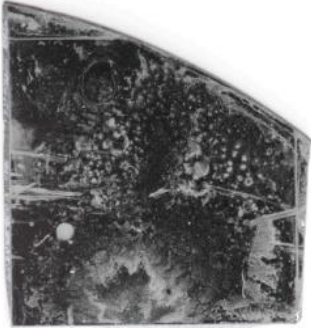
10				
11				
12				

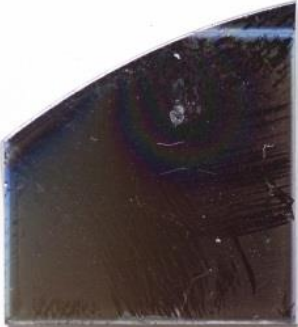
13				
CRL (RAL 135)				
KFM (RAL 136)				

UV-III

1					
2					
3					

4					
5					
6					

7					
8					
9					

10					
11					

**ma-N415**

Resist Layer Thickness				
55	1			
	2			
	3			

	<b>4</b>			
<b>70</b>	<b>1</b>			
	<b>2</b>			

85	1			
	2			
115	1			

	2			
--	---	------------------------------------------------------------------------------------	-------------------------------------------------------------------------------------	-------------------------------------------------------------------------------------

ma-N2410(2)

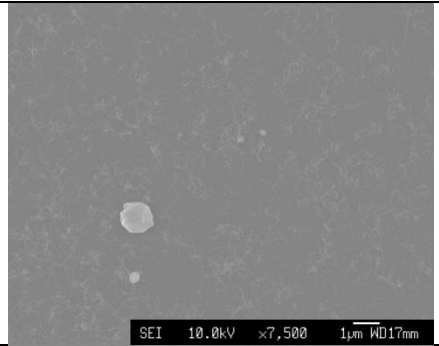
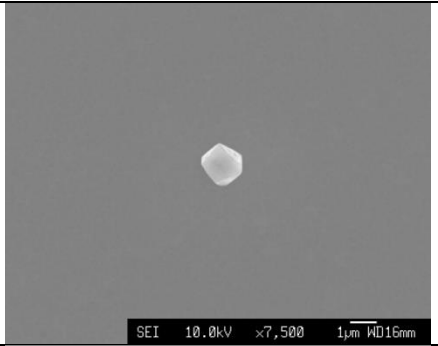
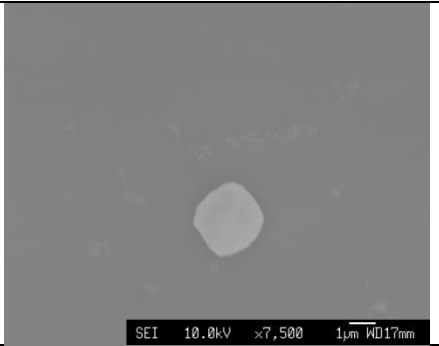
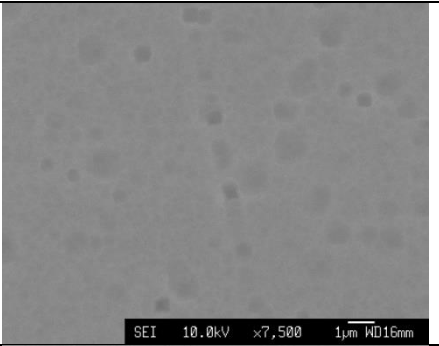
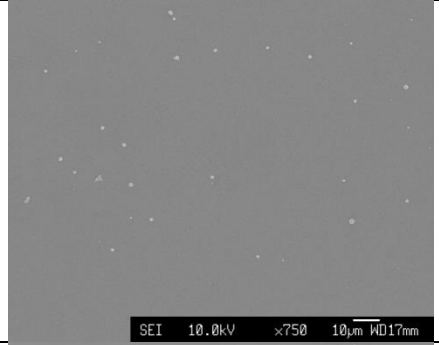
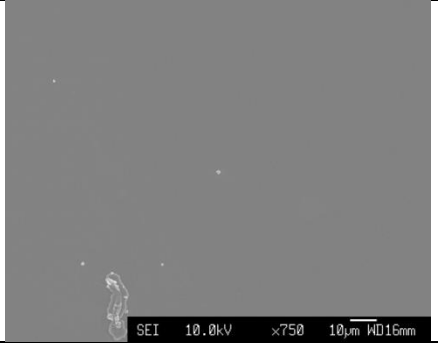
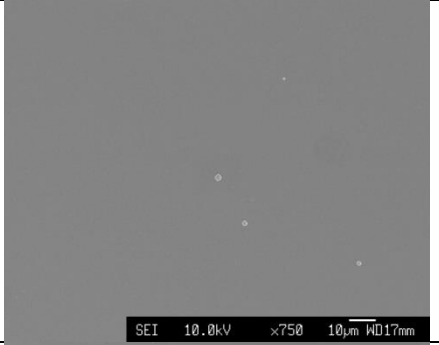
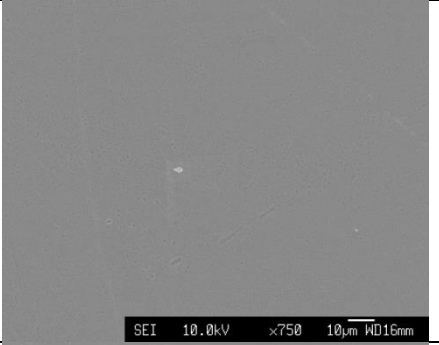
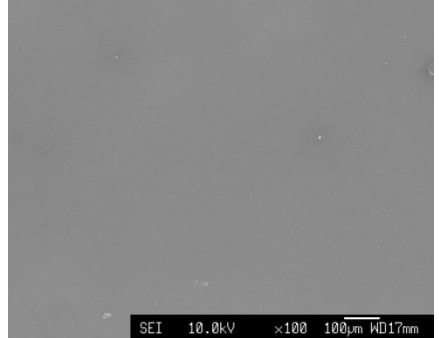
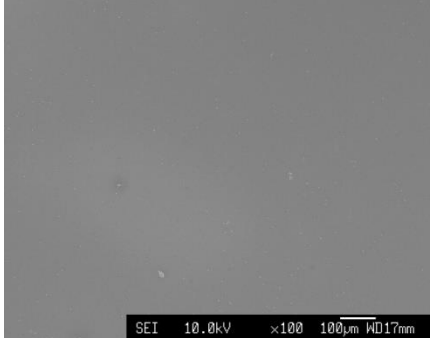
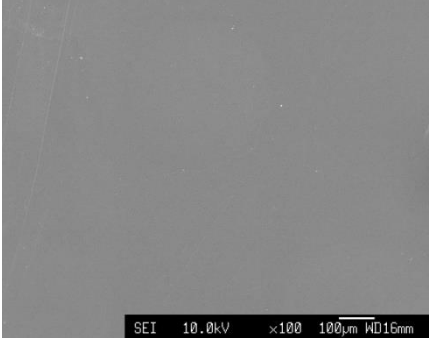
Resist Layer Thickness			
100			

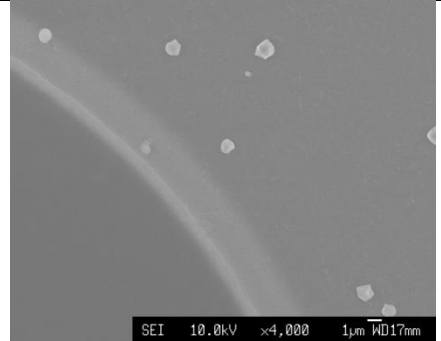
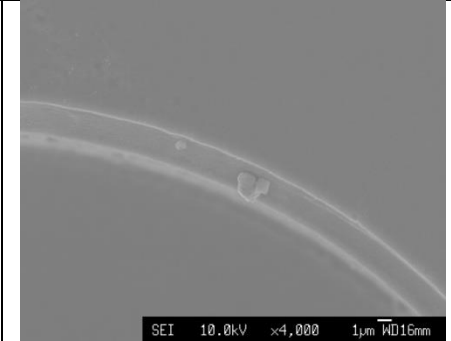
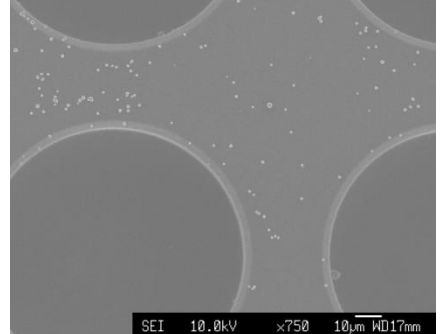
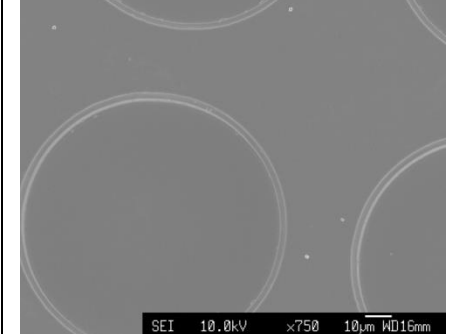
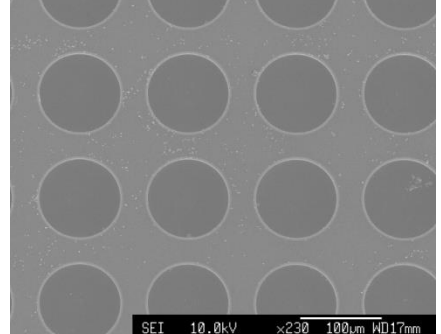
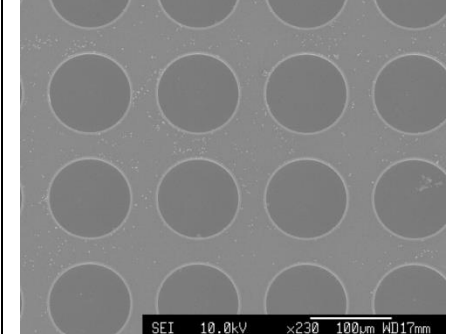
200			
200			
300			

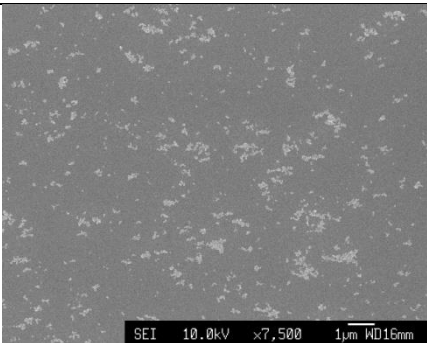
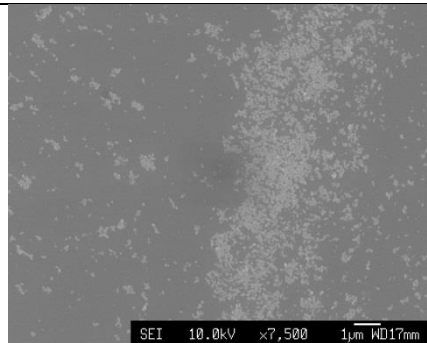
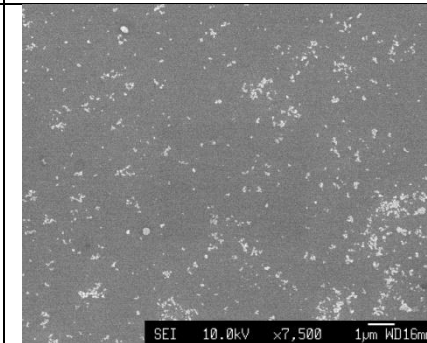
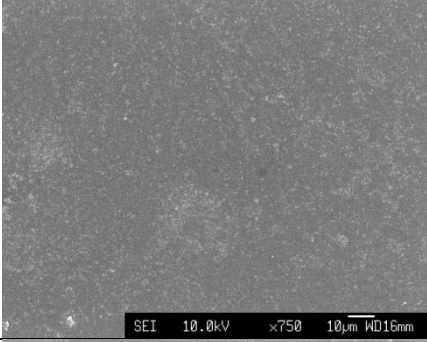
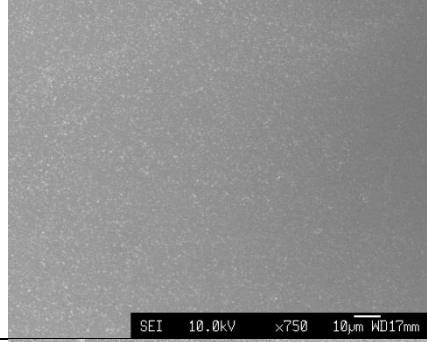
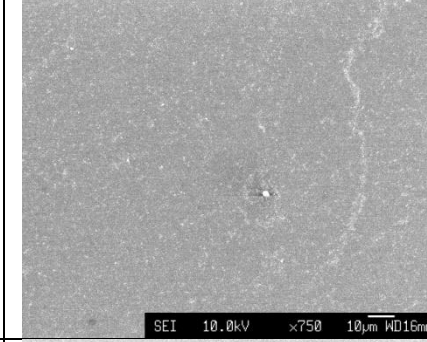
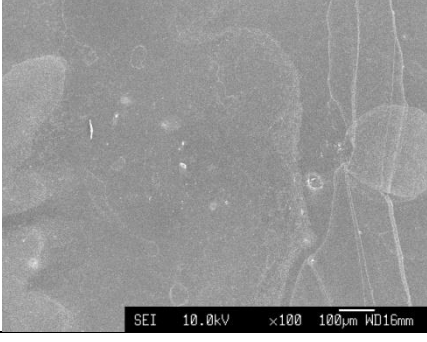
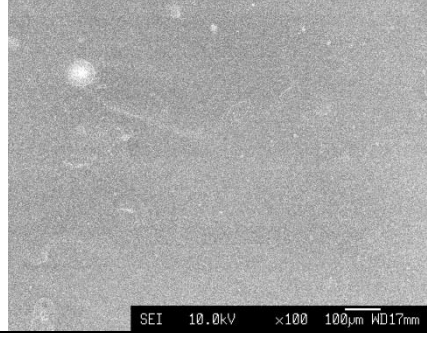
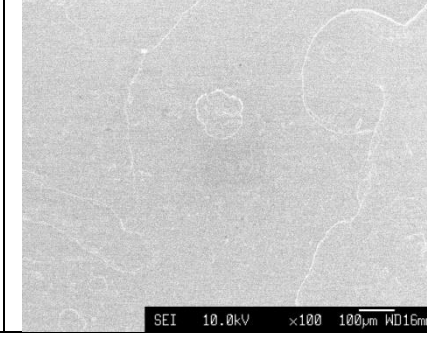
400

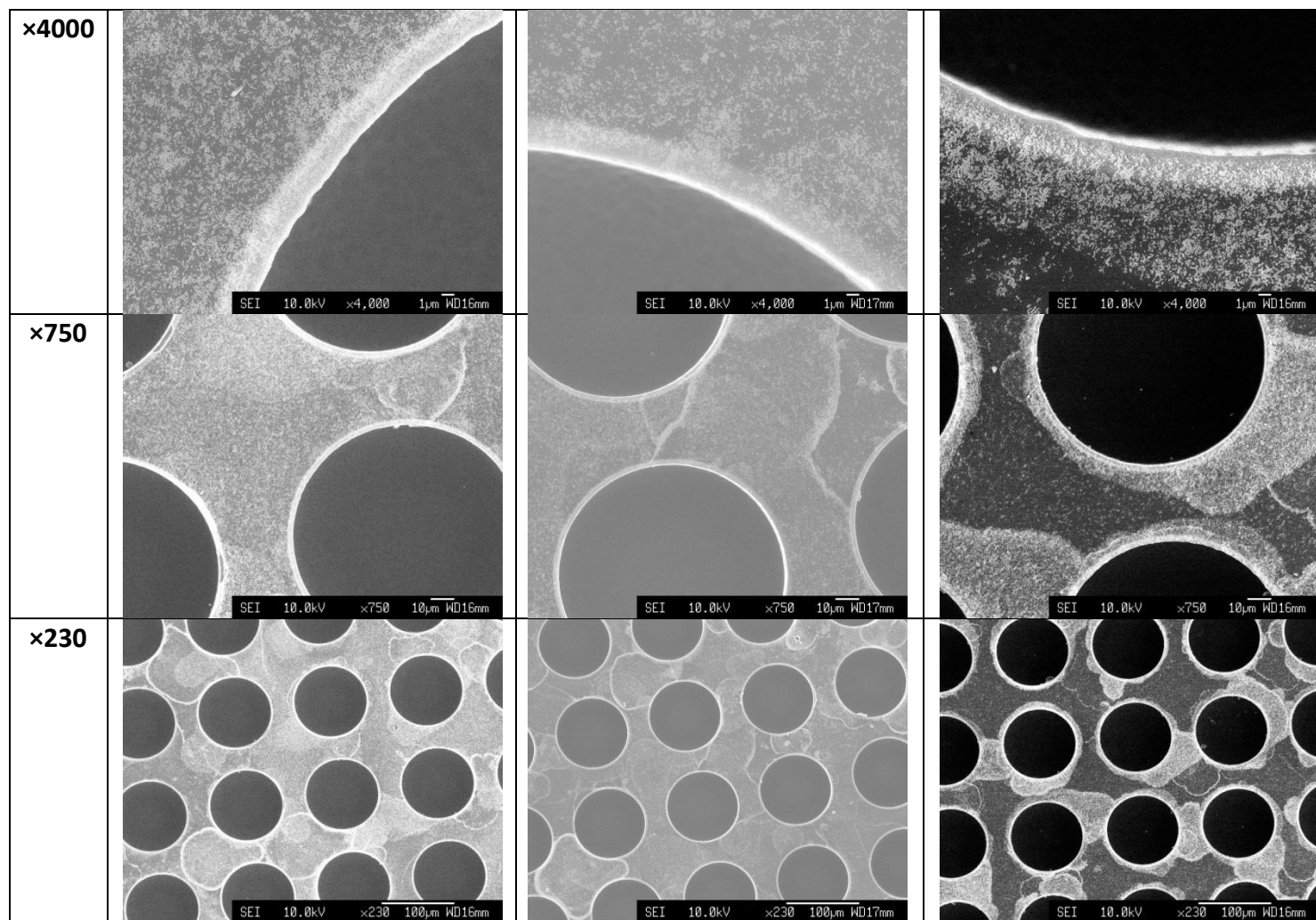


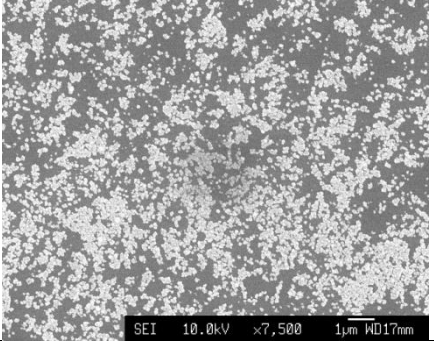
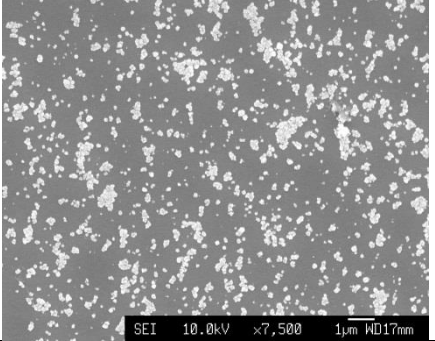
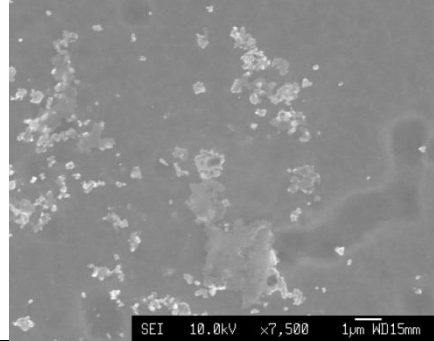
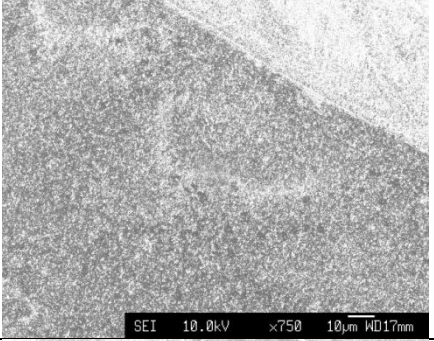
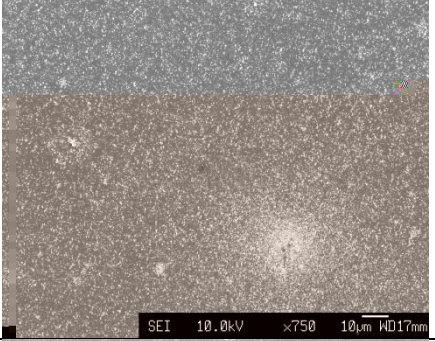
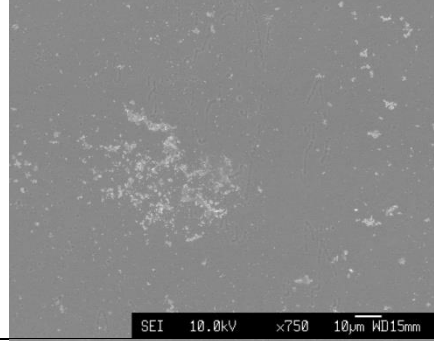
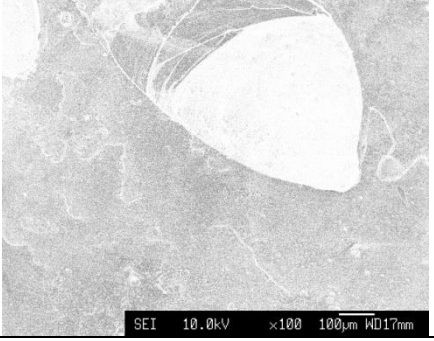
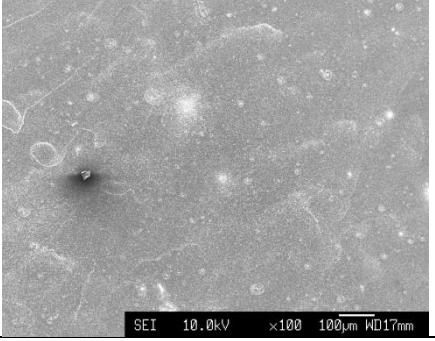
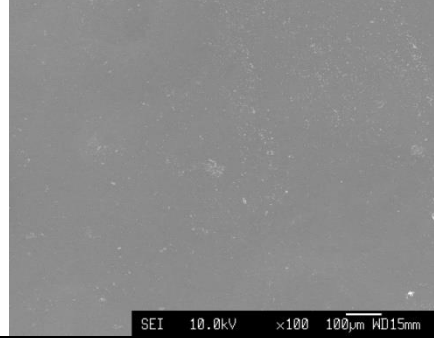
### 14.8 SEM images of SiO samples before and after buffered oxide etch (BOE)

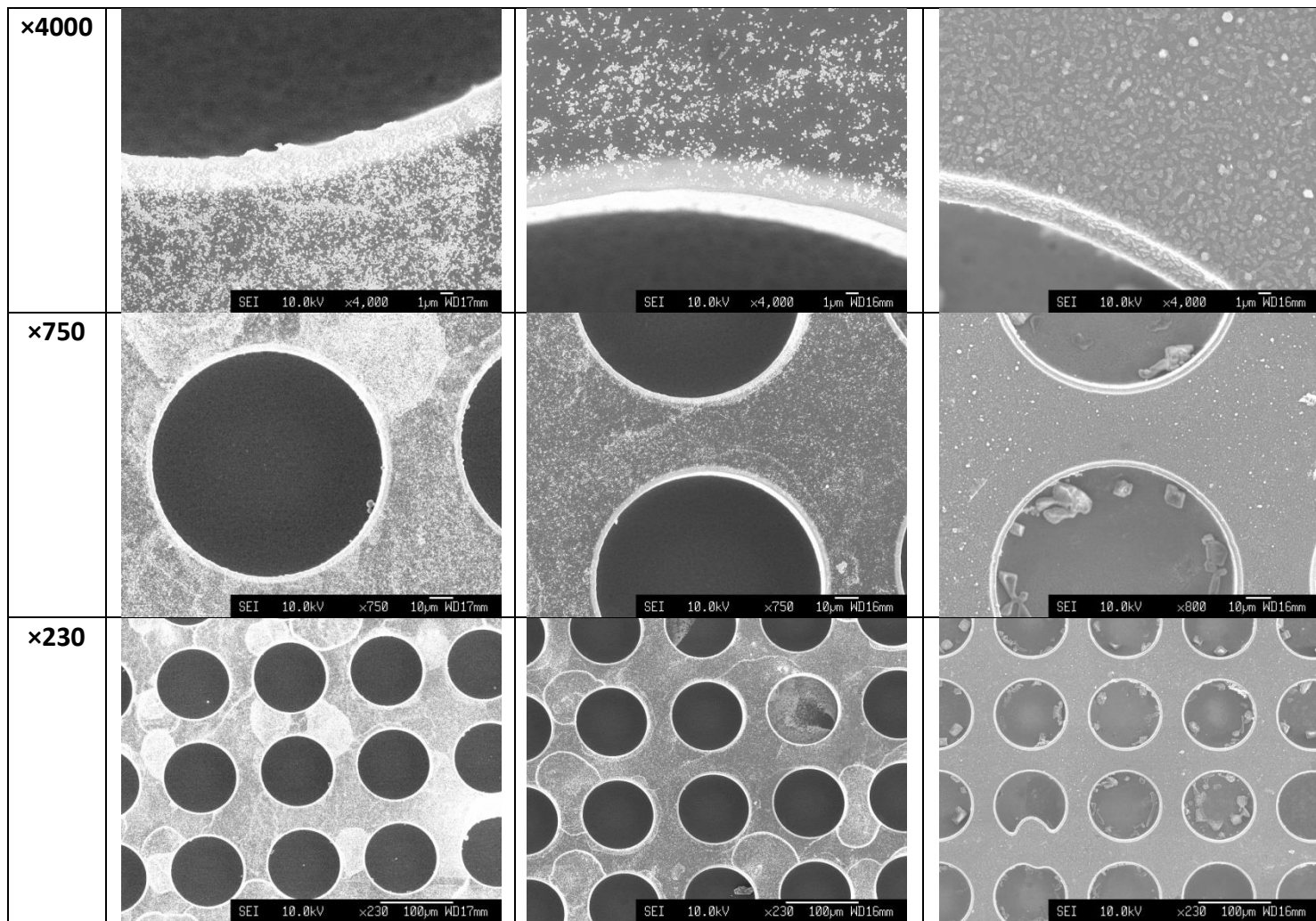
	SiO4	SiO4BOE	SiO5	SiO5BOE
<b>×7500</b>				
<b>×750</b>				
<b>×100</b>				

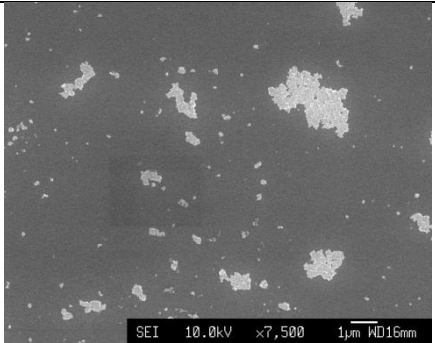
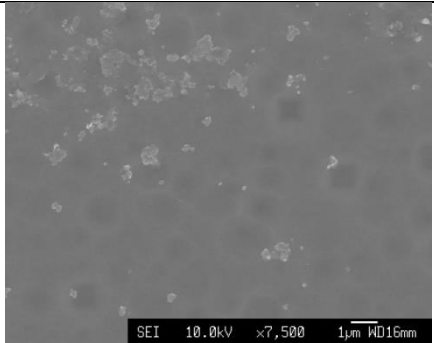
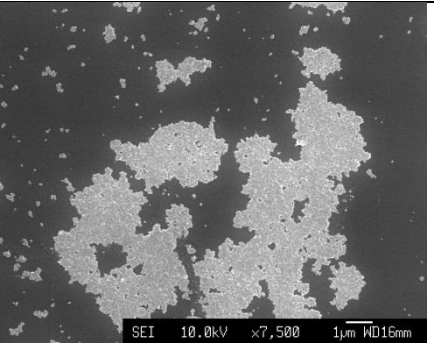
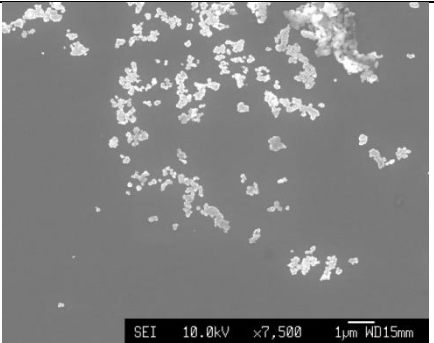
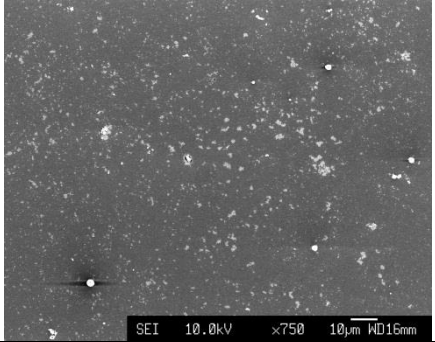
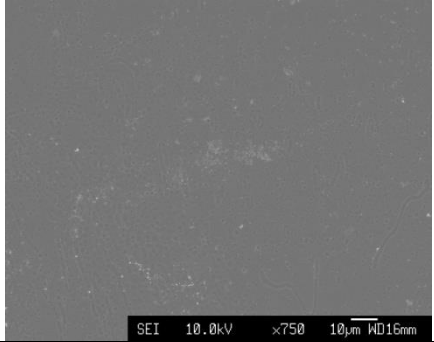
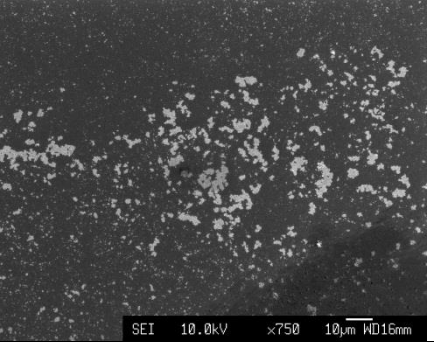
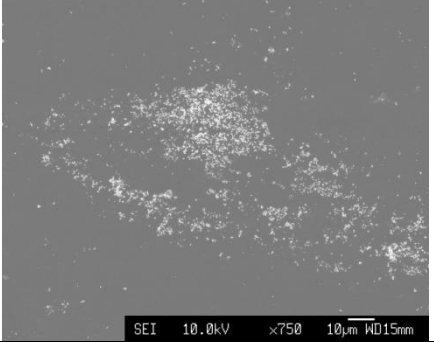
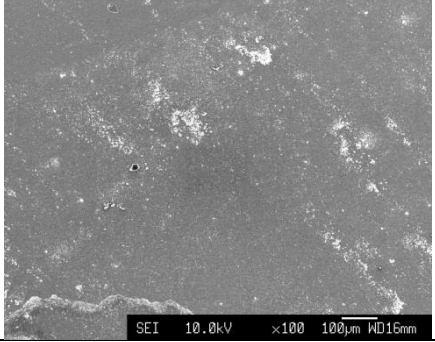
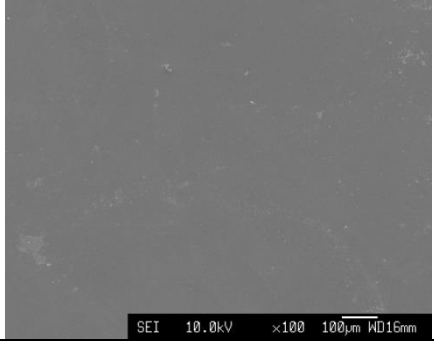
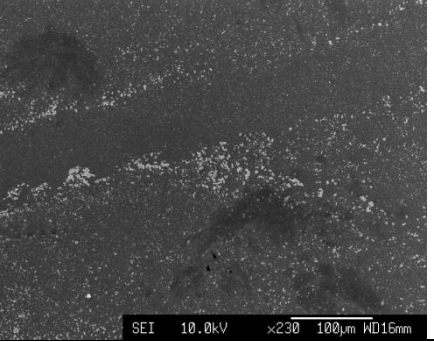
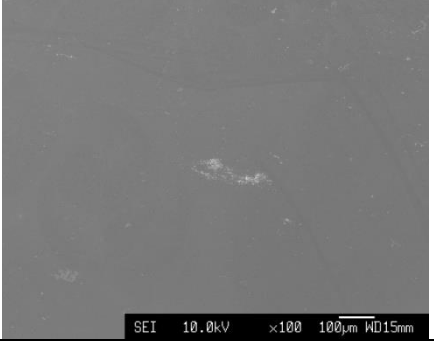
<p><b>×4000</b></p>				
<p><b>×750</b></p>				
<p><b>×230</b></p>				

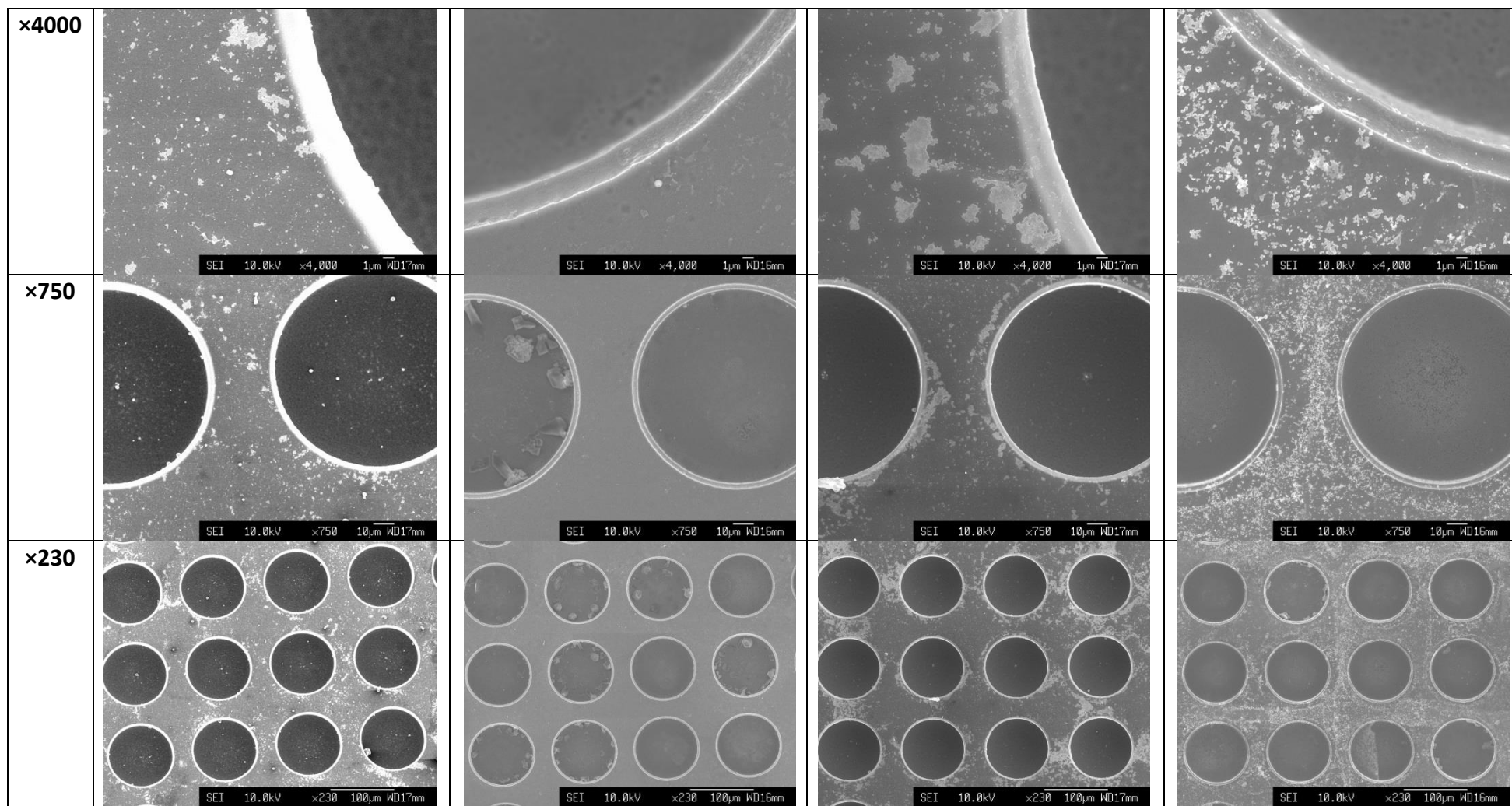
	SiO6	SiO6BOE	SiO7
<b>×7500</b>			
<b>×750</b>			
<b>×100</b>			



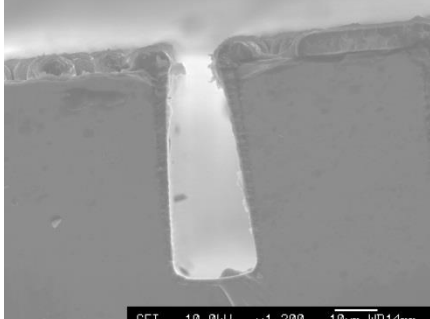
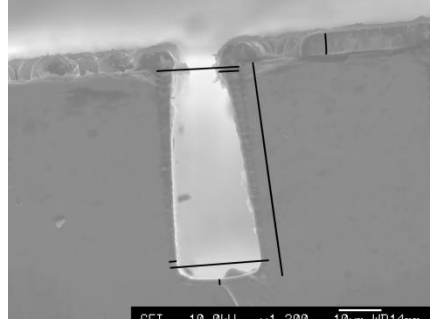
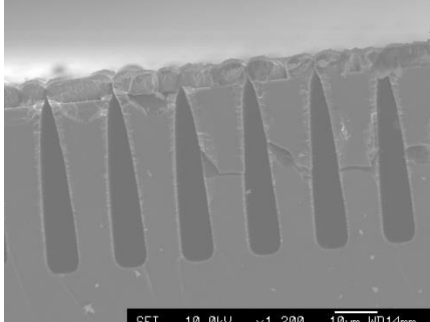
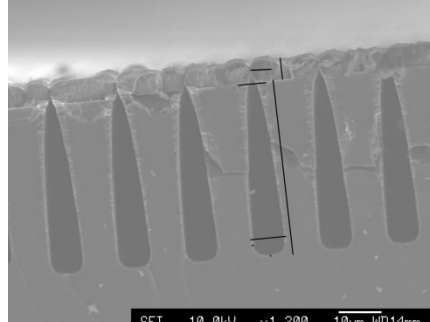
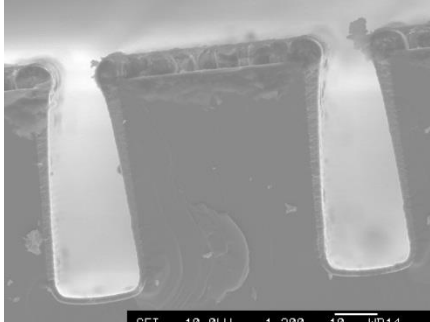
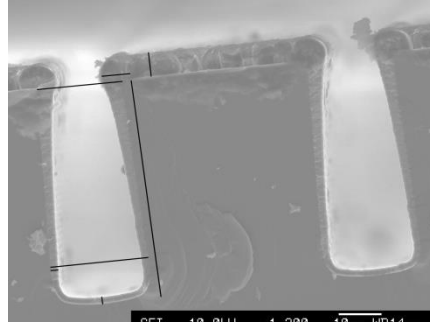
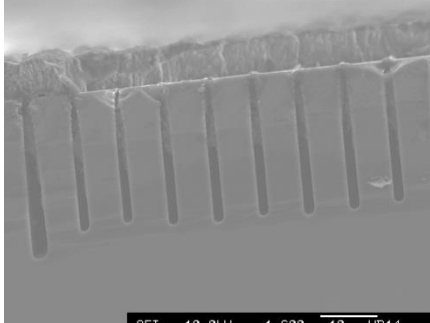
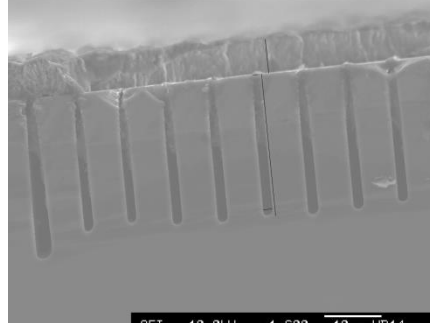
	SiO8	SiO9	SiO9BOE
<b>×7500</b>			
<b>×750</b>			
<b>×100</b>			

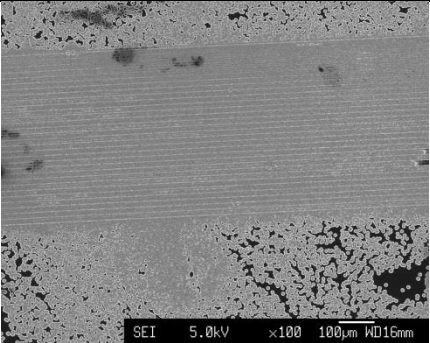
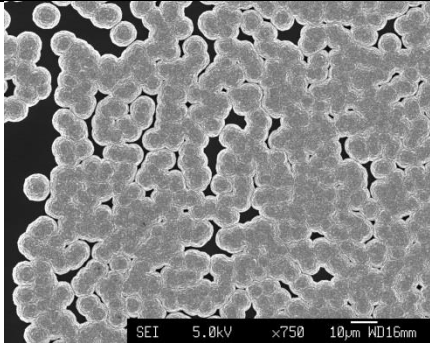
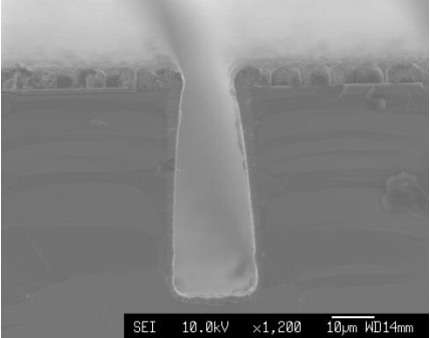
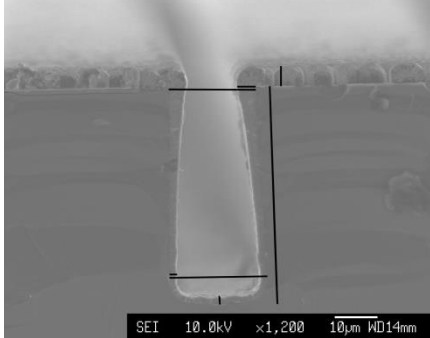
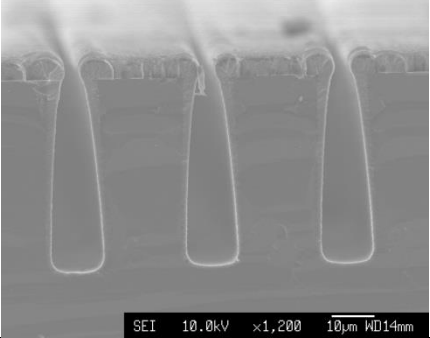
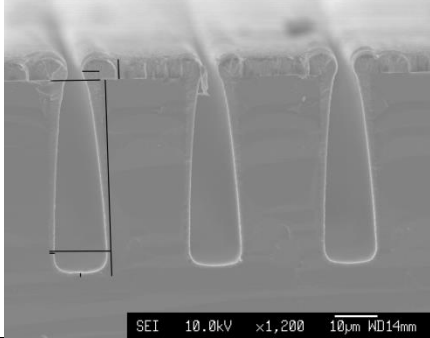
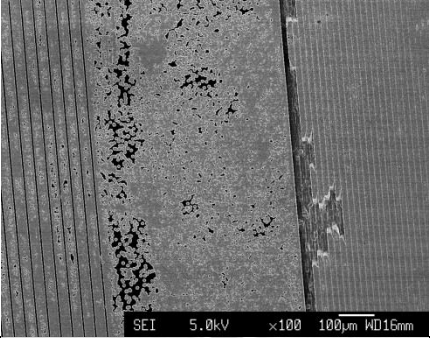
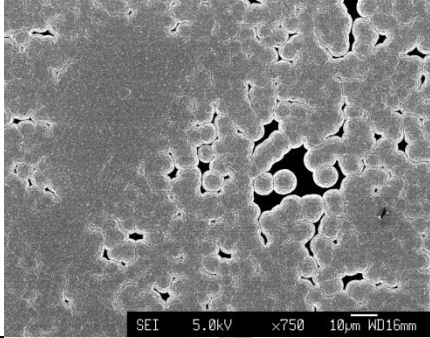
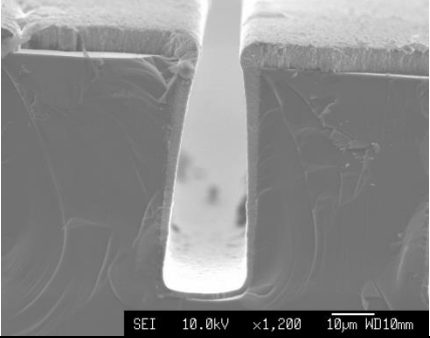
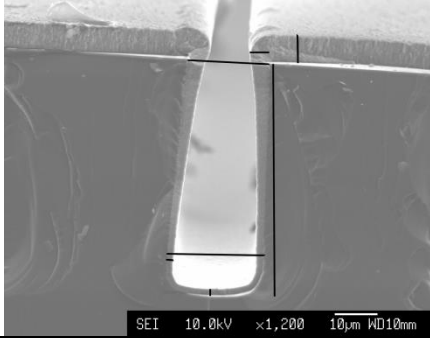


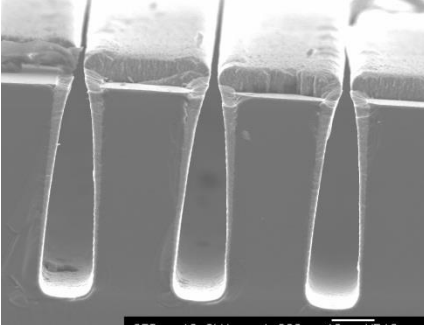
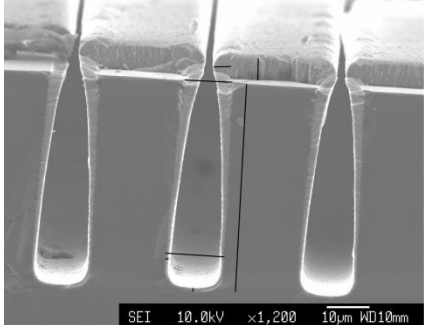
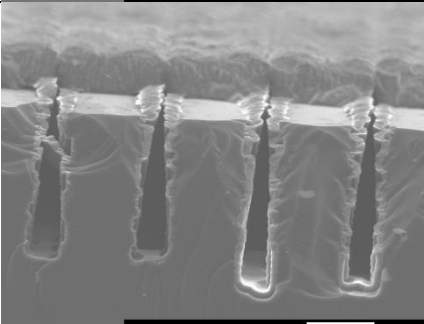
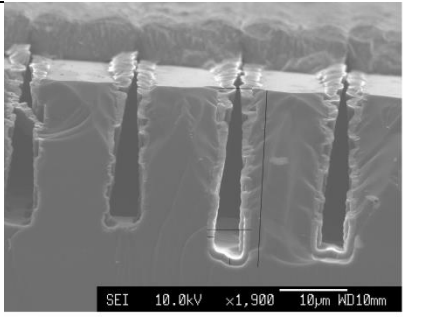
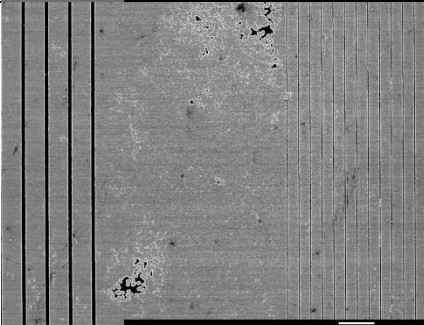
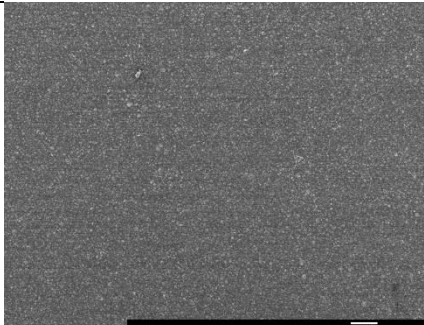
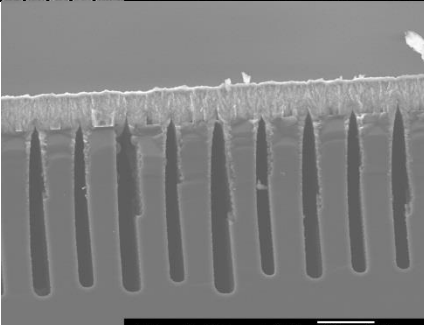
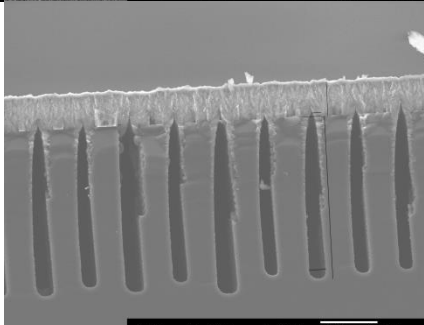
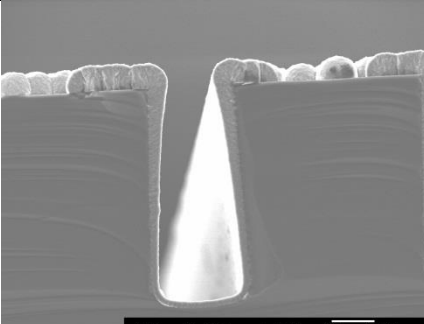
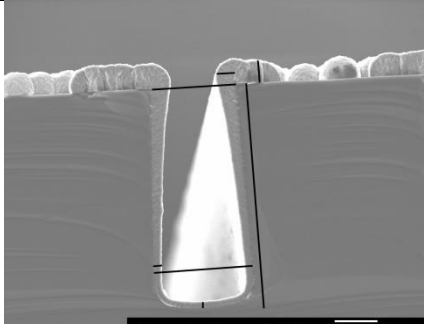
	SiO10	SiO10BOE	SiO11	SiO11BOE
<b>×7500</b>				
<b>×750</b>				
<b>×100</b>				

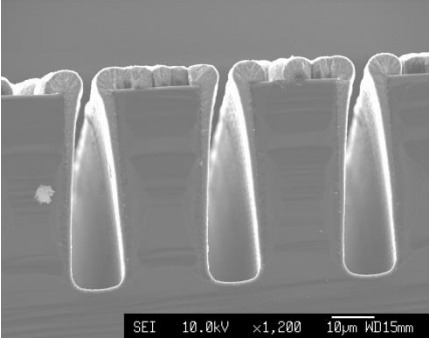
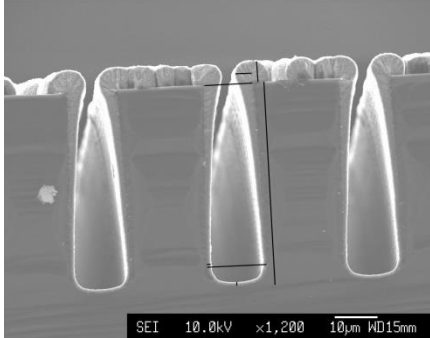
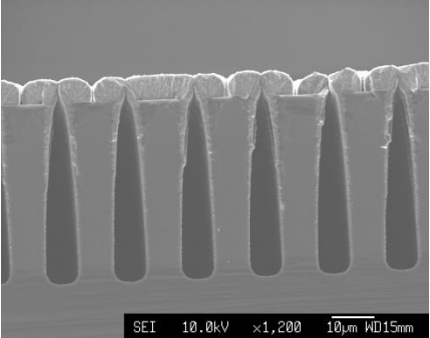
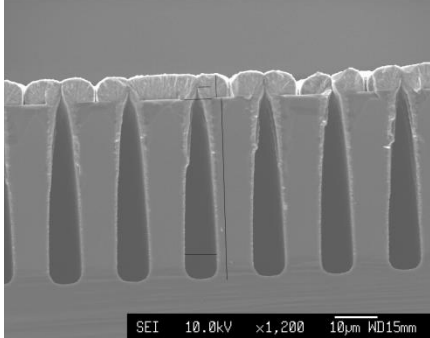
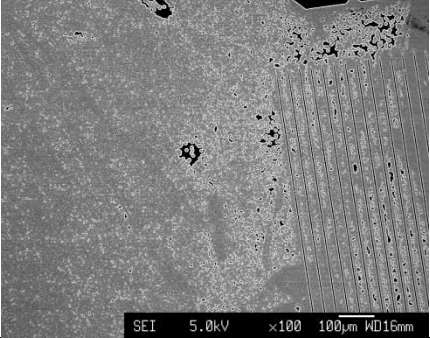
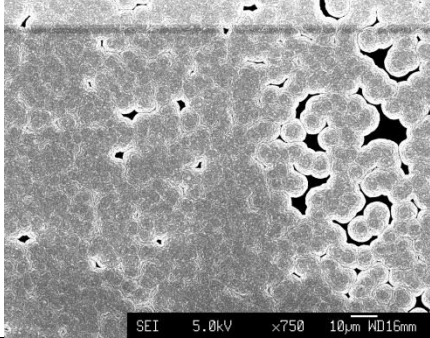
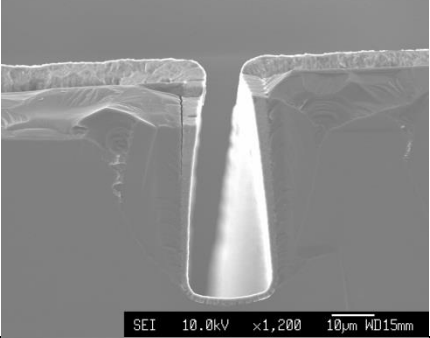
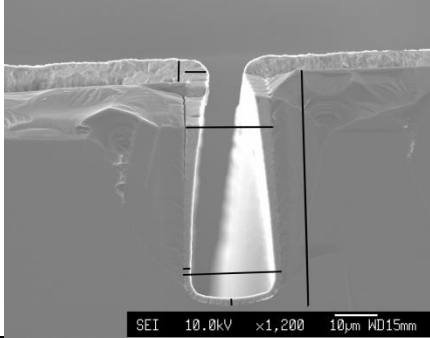
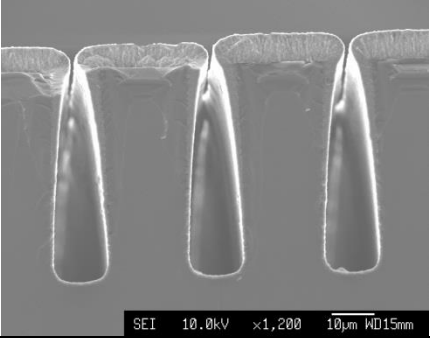
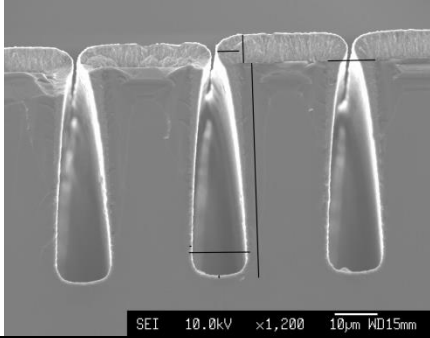


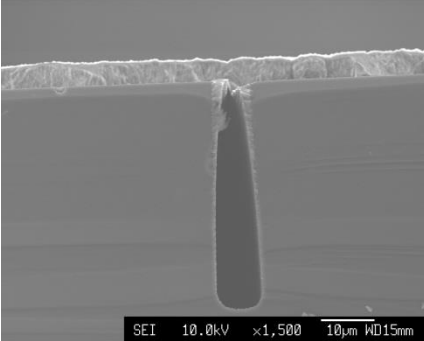
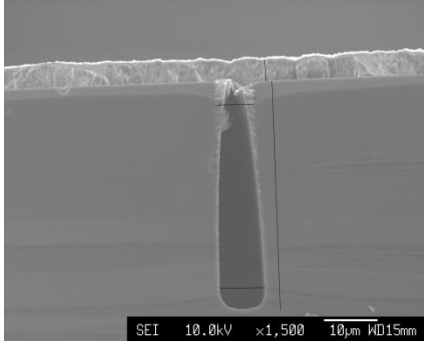
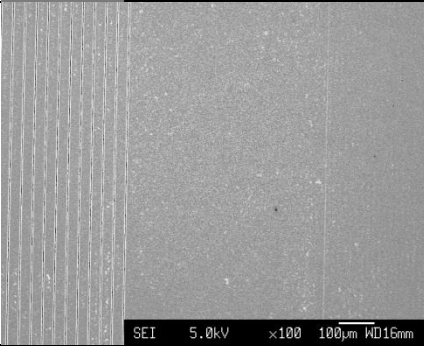
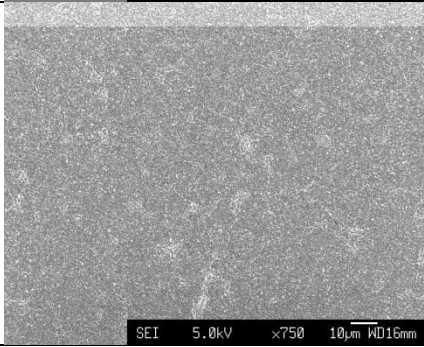
**14.9 SEM images of the DL samples fabricated at Kelvin Nanotechnology after a 3 h NCD deposition on each and the measurements used to calculate various growth parameters**

DL10	Trench1		
	Trench2		
	Trench3		
	Trench4		

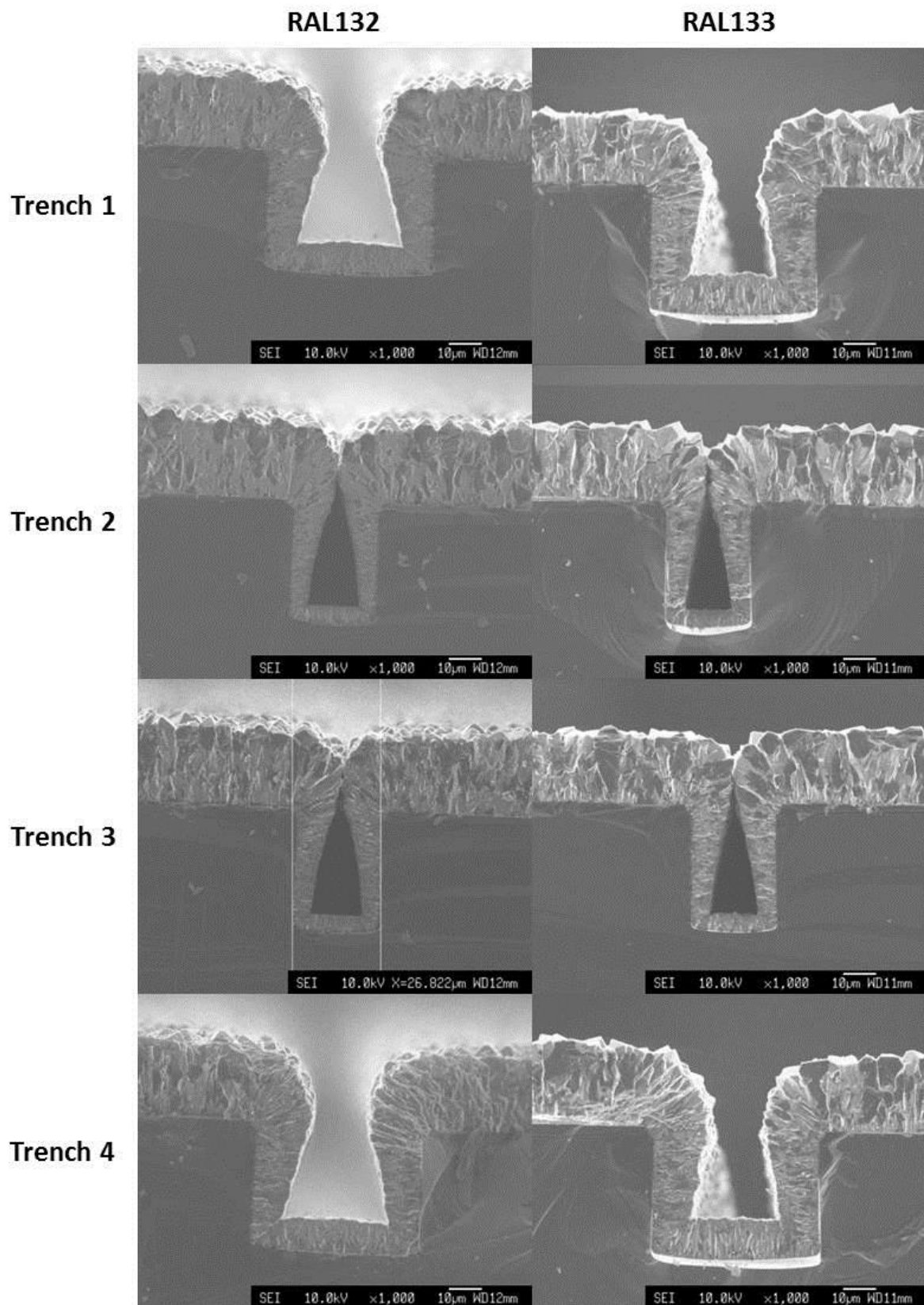
	<b>Surface</b>	 SEI 5.0kV x100 100µm WD16mm	 SEI 5.0kV x750 10µm WD16mm
<b>DL11</b>	<b>Trench1</b>	 SEI 10.0kV x1,200 10µm WD14mm	 SEI 10.0kV x1,200 10µm WD14mm
	<b>Trench2</b>	 SEI 10.0kV x1,200 10µm WD14mm	 SEI 10.0kV x1,200 10µm WD14mm
	<b>Surface</b>	 SEI 5.0kV x100 100µm WD16mm	 SEI 5.0kV x750 10µm WD16mm
<b>DL13</b>	<b>Trench1</b>	 SEI 10.0kV x1,200 10µm WD10mm	 SEI 10.0kV x1,200 10µm WD10mm

	<b>Trench2</b>	 <p>SEI 10.0kV x1,200 10µm WD10mm</p>	 <p>SEI 10.0kV x1,200 10µm WD10mm</p>
	<b>Trench3</b>	 <p>SEI 10.0kV x1,900 10µm WD10mm</p>	 <p>SEI 10.0kV x1,900 10µm WD10mm</p>
	<b>Surface</b>	 <p>SEI 5.0kV x100 100µm WD15mm</p>	 <p>SEI 5.0kV x750 10µm WD15mm</p>
<b>DL15</b>	<b>Trench1</b>	 <p>SEI 10.0kV x1,600 10µm WD15mm</p>	 <p>SEI 10.0kV x1,600 10µm WD15mm</p>
	<b>Trench2</b>	 <p>SEI 10.0kV x1,200 10µm WD15mm</p>	 <p>SEI 10.0kV x1,200 10µm WD15mm</p>

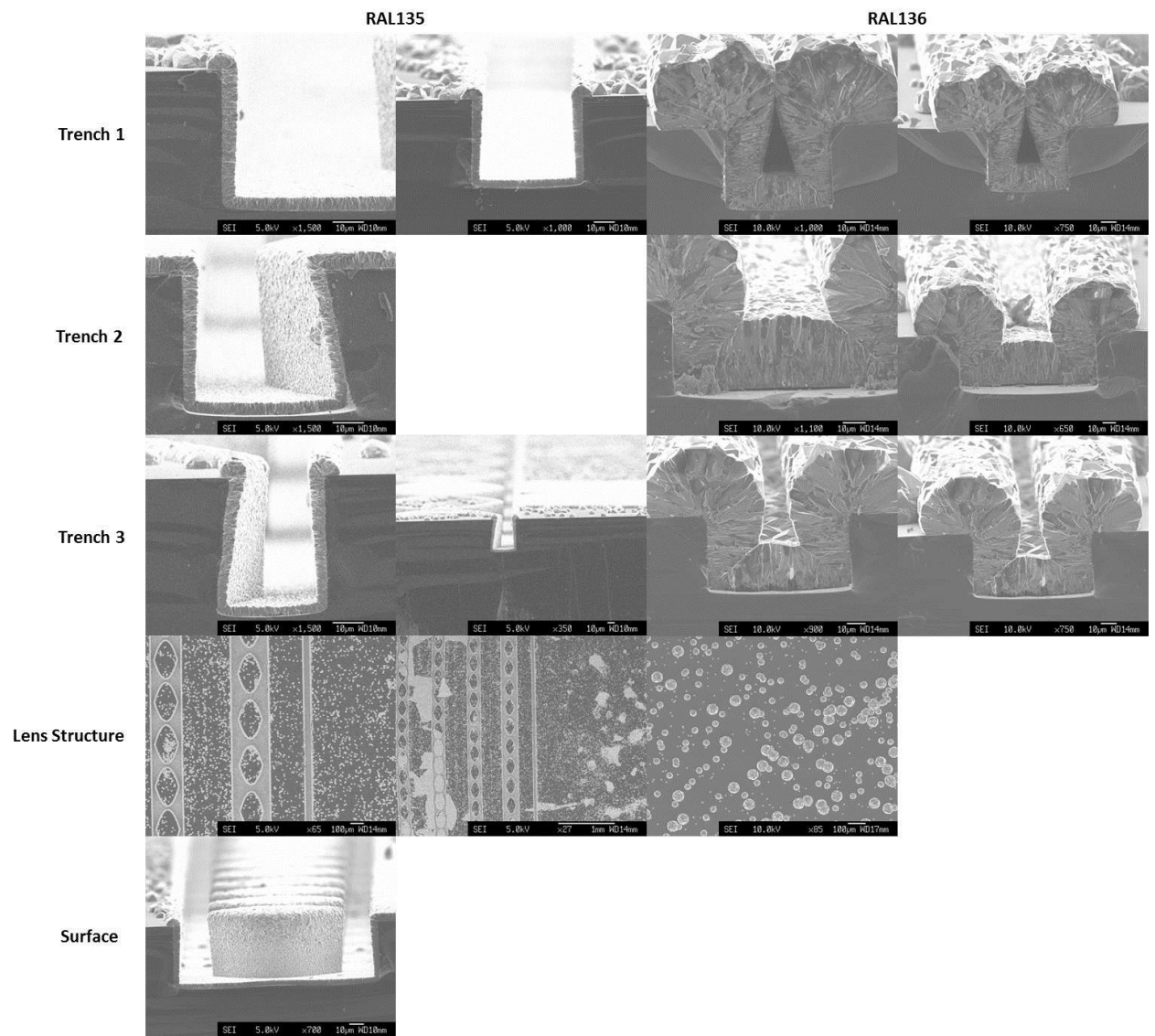
	<b>Trench3</b>		
	<b>Trench4</b>		
	<b>Surface</b>		
<b>DL16</b>	<b>Trench1</b>		
	<b>Trench2</b>		

	<b>Trench3</b>	 <p>SEI 10.0kV x1,500 10µm WD15mm</p>	 <p>SEI 10.0kV x1,500 10µm WD15mm</p>
	<b>Surface</b>	 <p>SEI 5.0kV x100 100µm WD16mm</p>	 <p>SEI 5.0kV x750 10µm WD16mm</p>

### 14.10 SEM images comparing the filling of the trenches on samples RAL132 and RAL133

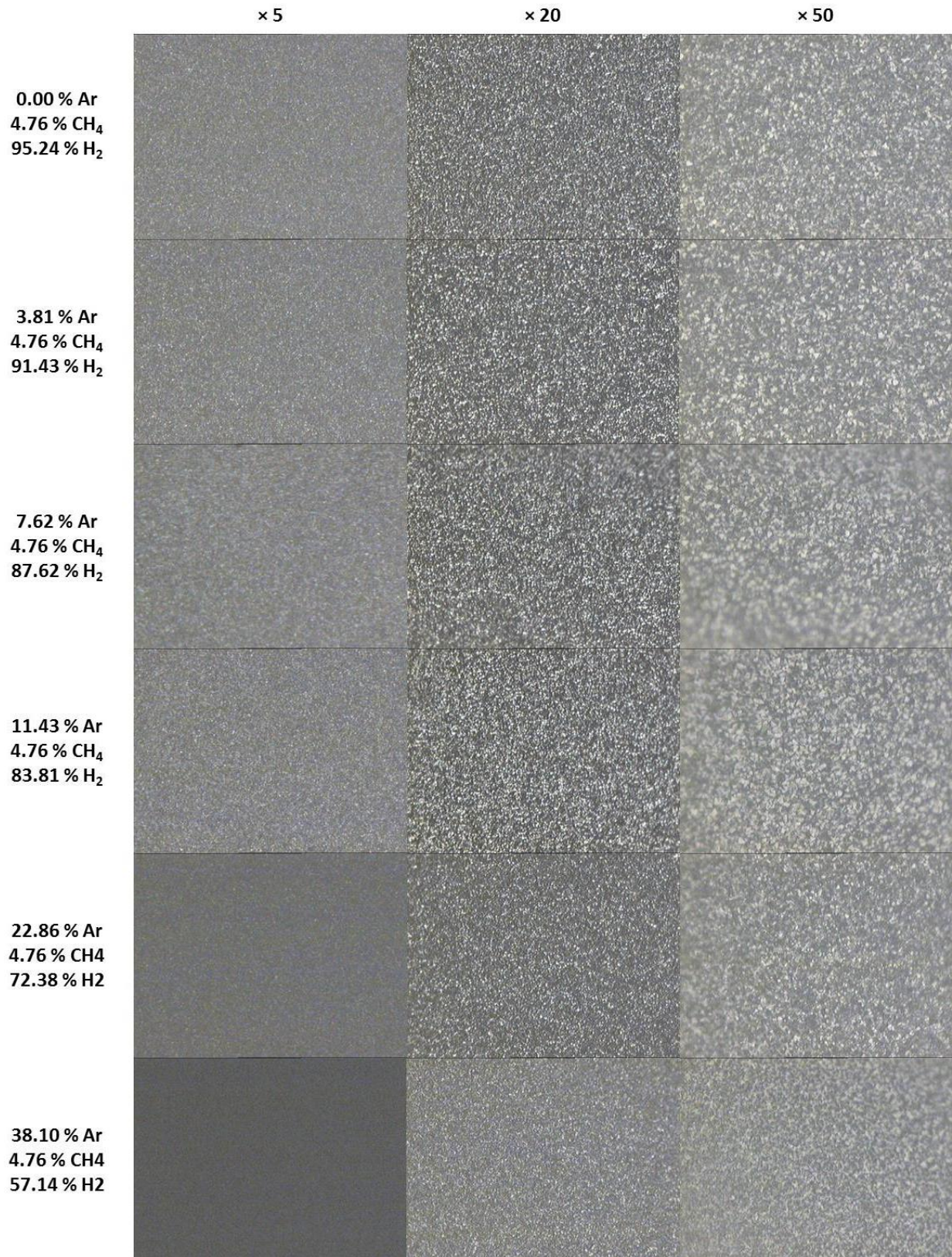


# 14.11 SEM images of selected-area deposition on samples RAL135 and RAL136

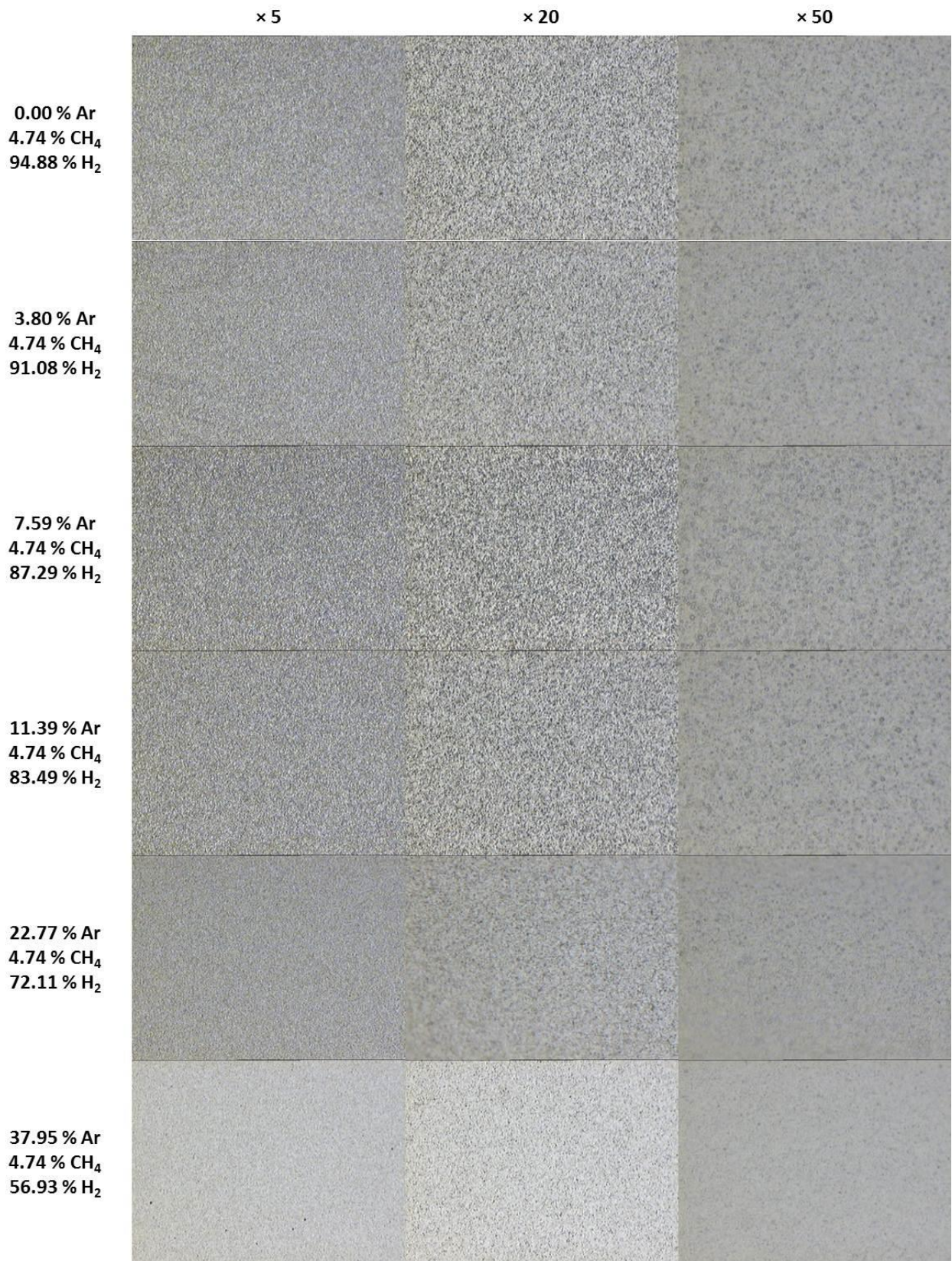


## 14.12 Optical microscope images comparing the diamond films grown for 1 h under varying gas mixtures

$\chi_0(\text{N}_2) = 0.00\%$



$\chi_0(\text{N}_2) = 0.38\%$



$\chi_0(\text{N}_2) = 0.76\%$



$\chi_0(\text{N}_2) = 1.13\%$

× 5

× 20

× 50

0.00 % Ar  
4.71 % CH<sub>4</sub>  
94.16 % H<sub>2</sub>

3.77 % Ar  
4.71 % CH<sub>4</sub>  
90.39 % H<sub>2</sub>

7.53 % Ar  
4.71 % CH<sub>4</sub>  
86.63 % H<sub>2</sub>

11.30 % Ar  
4.71 % CH<sub>4</sub>  
82.86 % H<sub>2</sub>

22.60 % Ar  
4.71 % CH<sub>4</sub>  
71.56 % H<sub>2</sub>

37.66 % Ar  
4.71 % CH<sub>4</sub>  
56.50 % H<sub>2</sub>



$\chi_0(\text{N}_2) = 1.50\%$

× 5

× 20

× 50

0.00 % Ar  
4.69 % CH<sub>4</sub>  
93.81 % H<sub>2</sub>

3.75 % Ar  
4.69 % CH<sub>4</sub>  
90.06 % H<sub>2</sub>

7.50 % Ar  
4.69 % CH<sub>4</sub>  
86.31 % H<sub>2</sub>

11.26 % Ar  
4.69 % CH<sub>4</sub>  
82.55 % H<sub>2</sub>

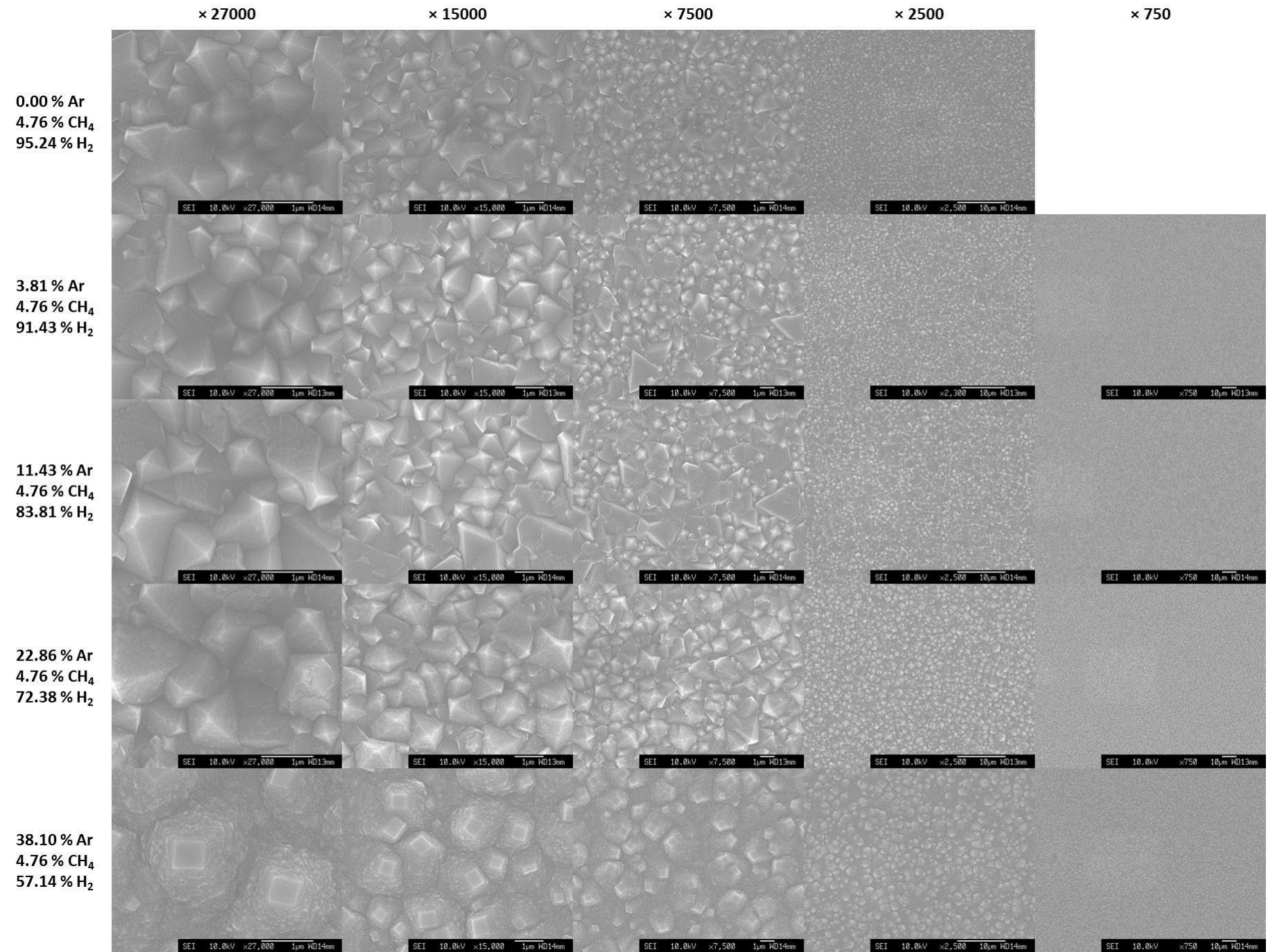
22.51 % Ar  
4.69 % CH<sub>4</sub>  
71.30 % H<sub>2</sub>

37.52 % Ar  
4.69 % CH<sub>4</sub>  
56.29 % H<sub>2</sub>



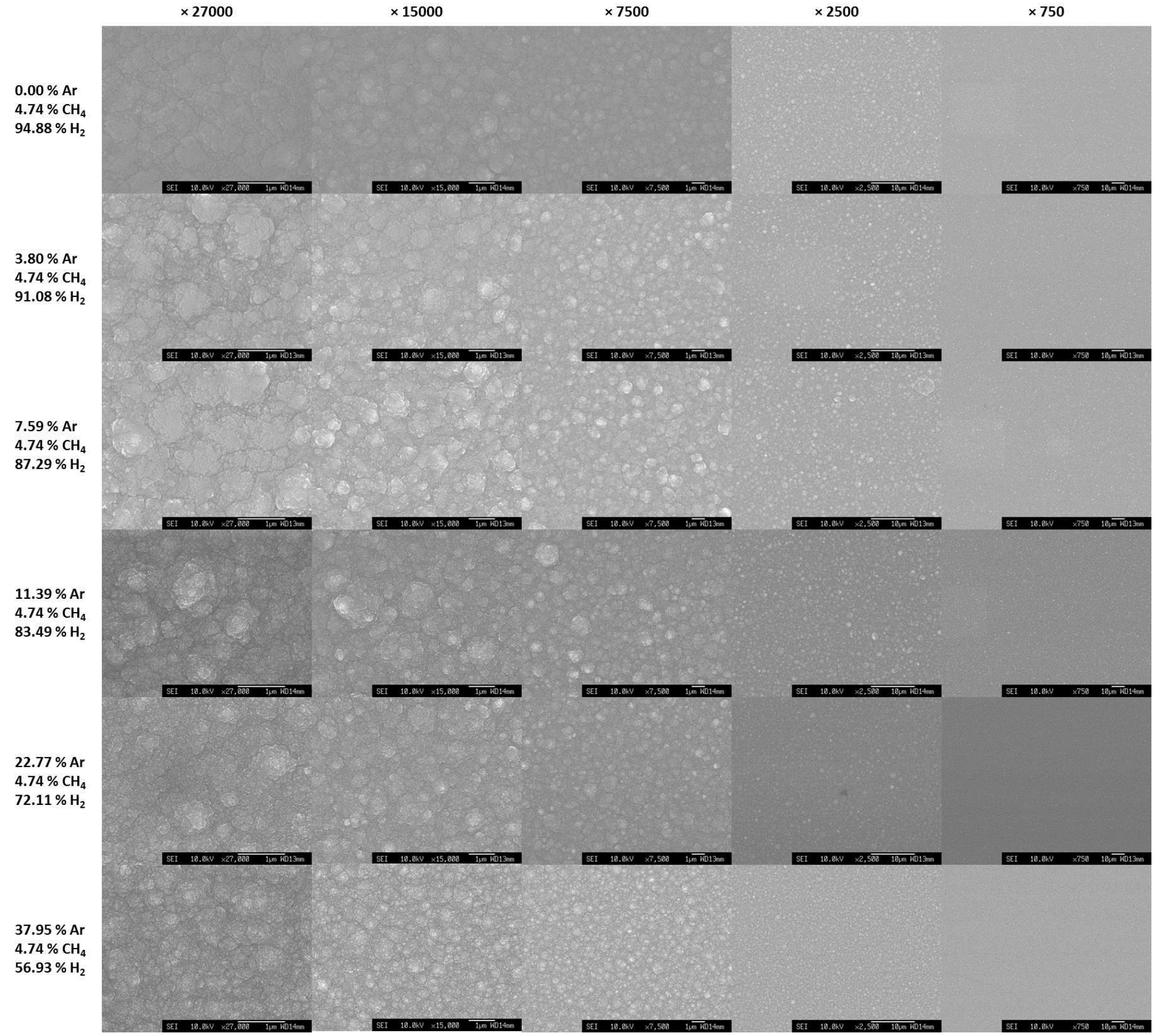
14.13 SEM images comparing the diamond films grown after 1 h in various gas mixtures

$\chi_0(\text{N}_2) = 0.00\%$

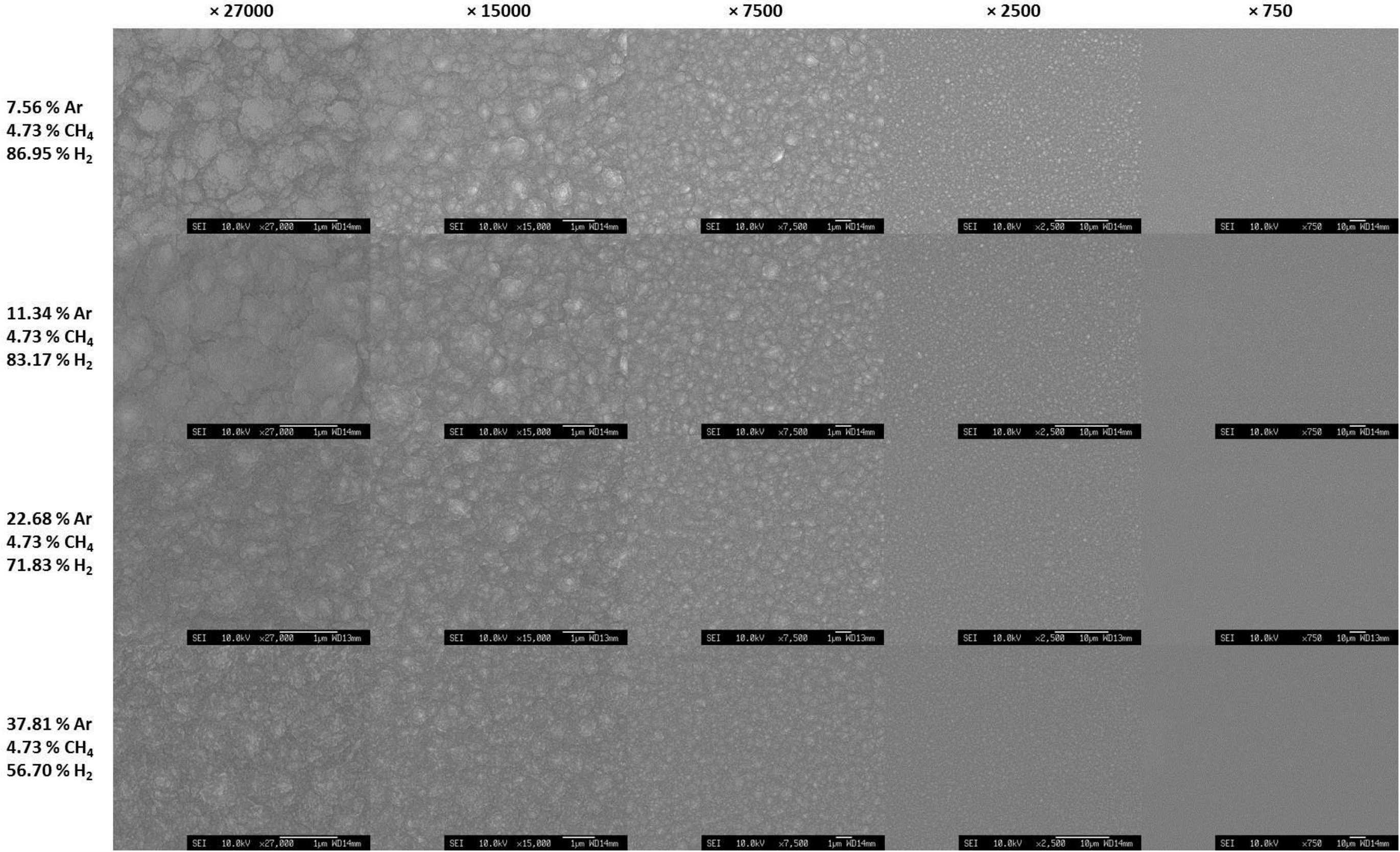




$\chi_0(\text{N}_2) = 0.38 \%$

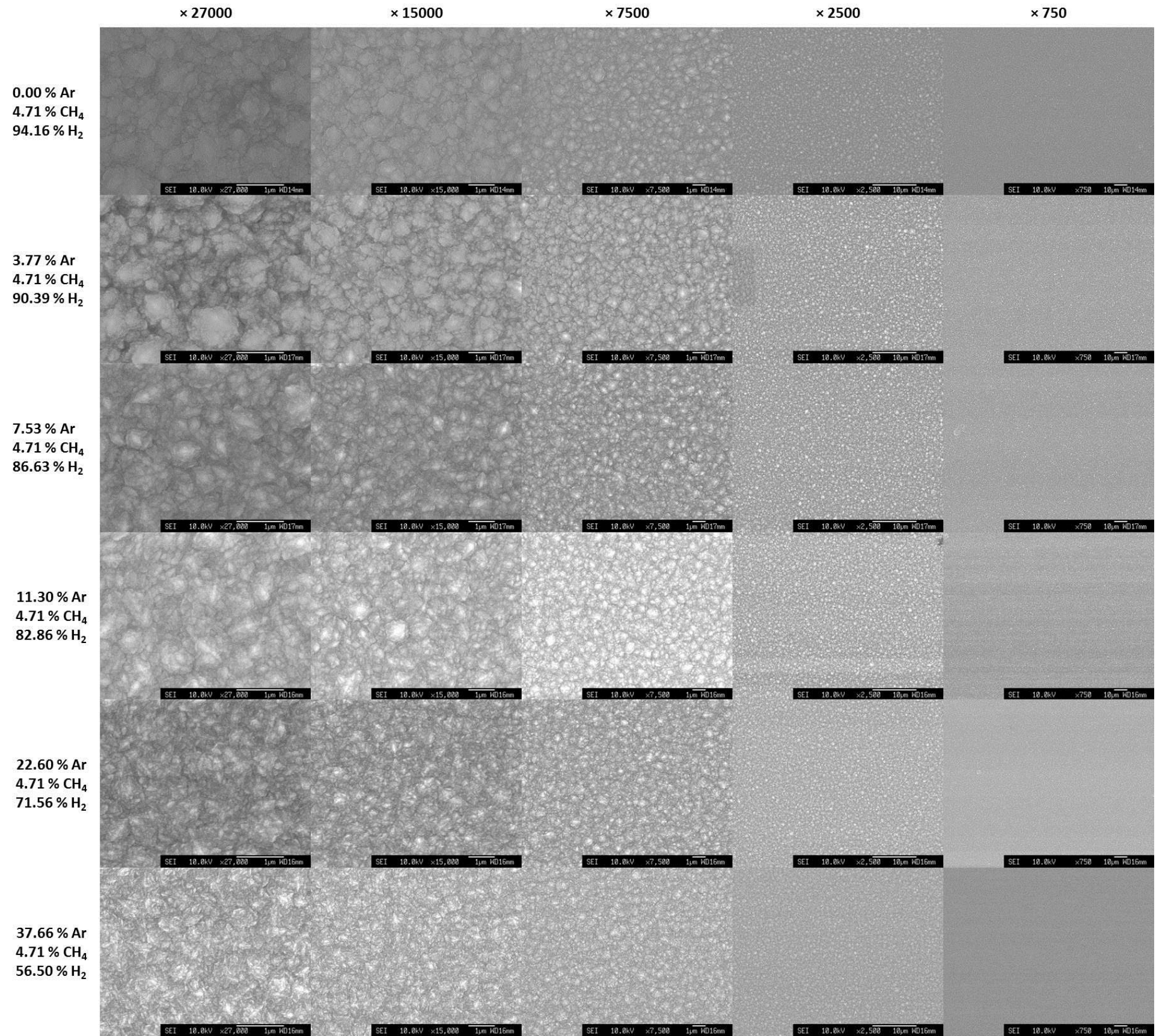








$\chi_0(\text{N}_2) = 1.13 \%$





$\chi_0(\text{N}_2) = 1.50\%$

